



HAL
open science

Thrombosis modeling in blood coated medical devices

Rodrigo Mendez Rojano

► **To cite this version:**

Rodrigo Mendez Rojano. Thrombosis modeling in blood coated medical devices. General Mathematics [math.GM]. Université Montpellier, 2018. English. NNT : 2018MONT088 . tel-02152653

HAL Id: tel-02152653

<https://theses.hal.science/tel-02152653>

Submitted on 11 Jun 2019

HAL is a multi-disciplinary open access archive for the deposit and dissemination of scientific research documents, whether they are published or not. The documents may come from teaching and research institutions in France or abroad, or from public or private research centers.

L'archive ouverte pluridisciplinaire **HAL**, est destinée au dépôt et à la diffusion de documents scientifiques de niveau recherche, publiés ou non, émanant des établissements d'enseignement et de recherche français ou étrangers, des laboratoires publics ou privés.

**THÈSE POUR OBTENIR LE GRADE DE DOCTEUR
DE L'UNIVERSITÉ DE MONTPELLIER**

En Mathématiques et Modélisation

École doctorale I2S

Unité de recherche IMAG

Thrombosis modeling in blood coated medical devices

Présentée par Rodrigo Méndez Rojano

Le 30 Octobre 2018

**Sous la direction de Franck Nicoud
et Simon Mendez**

Devant le jury composé de

Franck Nicoud	Professeur, Université de Montpellier	Directeur
Simon Mendez	Chargé de recherche, CNRS, Université de Montpellier	Co-encadrant
Didier Lucor	Directeur de recherche, CNRS, LIMSI, University Paris-Saclay	Président du jury
Xiao Yun Xu	Professeur, Imperial College London, England	Rapporteur
Yiannis Ventikos	Professeur, University College London, England	Rapporteur
Sophie Susen	Professeur des universités praticien hospitalier, CHRU de Lille	Examineur
François Caton	Chargé de recherche, CNRS, Université Grenoble-Alpes	Examineur



**UNIVERSITÉ
DE MONTPELLIER**

Acknowledgements

I am grateful to the CONACyT, Mexico scholarship and the LabEx Numev (convention ANR-10-LABX-20) for their financial support. Drs. Vincent Moureau and Ghislain Lartigue from CORIA laboratory, and the SUCCESS scientific group are acknowledged for providing the YALES2 solver which constitutes the basis of the YALES2BIO tool. Professor Jean-François Schved, MD. Muriel Giansily and Alexandre Ranc from the University Hospital of Montpellier are thanked for helpful discussions about the biological aspects of thrombosis. In addition they provided valuable experimental data from thrombosis generation assays. This work was performed using HPC resources from GENCI-CINES (Grants 2016-c2015037194 and 2017-A0020307194) and with the support of the High Performance Computing Platform HPC@LR.

I would like to express my sincere gratitude to the members of the committee: Xiao Yun Xu, Yiannis Ventikos, Sophie Susen, Didier Lucor and François Caton, I am honored by their presence.

Je souhaite remercier mes deux encadrants de thèse, Franck Nicoud et Simon Mendez, pour avoir guidé ce travail. Leur support dans les aspects pratiques (heures de calcul, ordinateur portable etc) et notamment pour m'avoir fait participer à des conférences. Ils m'ont permis de profiter de ma thèse et de me focaliser sur les aspects techniques. Surtout, je voudrai les remercier pour leurs compétences scientifiques, je suis très content d'avoir pu faire ma thèse avec eux.

Je remercie également Alexandre Ranc, Muriel Giansily-Blaizot et Jean-Francois Schved pour notre collaboration, plus particulièrement pour les données de génération de Thrombine qui ont contribué à développer le Chapitre 3 de cette thèse.

Je suis également très reconnaissant envers Didier Lucor pour notre collaboration qui s'est reflétée dans le Chapitre 3 ; j'espère sincèrement que cette collaboration continuera.

Je remercie l'équipe YALES2BIO: Julien, Stéphanie, Pierre, Thomas, Dorian, Robert, Alain et Pascal. L'ambiance dans l'équipe était toujours agréable. Je souhaite remercier tout le personnel administratif de l'IMAG, particulièrement Bernadette Lacan et Geneviève Carrière. Je souhaite remercier tous les doctorants de l'IMAG pour les bons moments de partage et pour les sessions de footing. Une pensée spéciale pour Gauthier, Anis et Mickäel pour avoir partagé des moments rigolos comme le challenge de Burritos.

Je souhaiterais remercier mes colocos Jonas et Eliana, ainsi qu'à Jean-Luc et Marielle qui m'ont accueilli pendant le premier mois de ma thèse. Leur hospitalité m'a marqué est m'a fait sentir comme chez moi au Mexique, je vous en serais toujours reconnaissant.

Pour finir la partie en français je souhaiterais remercier la famille Bayle, surtout Sandrine, Thierry, Lucyle, Mathylda, Monique et Max. Ils font partie maintenant de ma famille, les moments de partages ensemble m'ont beaucoup aidé à moins sentir la distance avec le Mexique.

Quiero agradecer brevemente a mi Familia por su apoyo. Gracias a todos mis primos y tíos que siempre se interesan en lo que hago y me han ayudado mucho. Un pensamiento muy especial para mi tía Cristina, este trabajo se lo dedico a ella. A Roge le quiero dedicar unas palabras, siempre fue un modelo a seguir y ha sido el contacto para conocer a nuevos primos que me han recibido con mucha alegría y afecto. Gracias a Dani, María, Alba, Jaime, Lidia y en general a la familia Flor.

Este trabajo no hubiera sido posible sin el esfuerzo y apoyo de mis papás Gilda y Ernesto, mis abuelos Ángela, José y Josefina. A mi hermano Luis y a Laura les doy las gracias por venir a verme y pasar momentos muy bonitos, igualmente los quiero mucho. Finalmente quiero decirle gracias a Audrey espero que podamos vivir muchas aventuras juntos.

Abstract

Thrombosis, which is the formation of a blood clot (thrombus) in the vascular system, is one of the major issues of blood-coated medical devices. To reduce thrombosis risk in this type of devices, computational fluid dynamics has been used. Existing thrombosis models have considered a wide range of biological processes. Nevertheless, to apply these models in the context of biomedical devices, a compromise between model description and computational efficiency must be searched. Up to date, bio-material surfaces used in blood coated devices initiate blood coagulation through the contact activation system. This system has not been considered in models dedicated to devices, even though its importance in thrombosis has been recently highlighted.

The objective of this thesis is to introduce device-triggered coagulation reactions in the modeling of device-related thrombosis. Detailed kinetic schemes of the coagulation cascade are useful to predict thrombin formation in quiescent blood plasma. However, they are computationally inefficient when dealing with complex flow configurations encountered in medical devices. Therefore, reduction of complex biological descriptions was also investigated.

In this study, a numerical framework for the initiation of the coagulation cascade is proposed. Thrombin formation in a backward facing step configuration is studied using a proper reactive boundary condition along with a detailed model of the coagulation cascade including the contact activation system. In our simulations, large thrombin concentrations are observed in the same region in which thrombus is formed experimentally. Due to large uncertainty reported on the reaction rates of the detailed kinetic model used, a global sensitivity analysis is performed in quiescent plasma simulations.

A novel reduced kinetic model including the contact activation system is proposed. The model correctly captures thrombin formation in physiological and prothrombin deficient platelet-poor-plasma. The reduced set of reactions is then included in a platelet-based model for thrombus formation considering platelet activation by thrombin. This approach is used to study thrombus formation in the backward facing step configuration. Large levels of platelet activation are observed due to thrombin activation. The original non-physiological dependency of the platelet-based model to background activation levels of platelets was suppressed using our approach.

Résumé

La thrombose est la formation d'un caillot sanguin (thrombus) dans le système cardiovasculaire. Il s'agit d'un des principaux problèmes des dispositifs biomédicaux en contact avec du sang. Pour réduire le risque de thrombose dans ce type de dispositifs, la mécanique des fluides numérique a été utilisée. Par exemple, Wu et al. [1] a développé un modèle basé sur l'activité plaquettaire pour prédire la croissance thrombotique dans un dispositif d'assistance ventriculaire (voir Fig.1). Les modèles de thrombose existants prennent en compte une large gamme des processus biochimiques. Cependant, pour appliquer ces modèles dans le contexte des dispositifs biomédicaux, un compromis entre description biologique et efficacité numérique doit être trouvé.

Actuellement, les approches dédiées à la formation de thrombus liée aux dispositifs sont concentrées sur l'adhésion et l'activation plaquettaire. Toutefois, les biomatériaux utilisés jusqu'à présent dans les dispositifs en contact avec du sang déclenchent également la coagulation à travers le système de contact comme expliqué par Yan et al. [2]. Ce système n'a pas été pris en compte dans les modèles de thrombose dédiés aux dispositifs, alors que son importance pour la thrombose a été récemment mise en évidence par Naudin et al. [3]. Parallèlement, des schémas cinétiques pour la formation de thrombine déclenchée par le système de contact ont été développés par Chatterjee et al. [4] et Zhu [5]. Ces schémas ont été capables de reproduire la formation de thrombine dans un échantillon de plasma pauvre en plaquettes. Des schémas cinétiques de la cascade de coagulation ont été couplés avec des modèles de mécanique des fluides (Biasetti et al. [6], Seo et al. [7]). Cependant, les cas étudiés sont propres à un thrombus provoqué par une blessure sur les parois de vaisseaux sanguins. Dans ces cas, la zone de formation thrombus est supposée connue et donc prescrite dans les simulations qui ne sont donc pas prédictives. Ce type d'approche ne peut pas être utilisée pour les décrire les dispositifs biomédicaux car la région où le thrombus se forme est a priori inconnue.

L'objectif de cette thèse est d'introduire les réactions de coagulation initiées par le système de contact dans la modélisation de la thrombose associée aux dispositifs

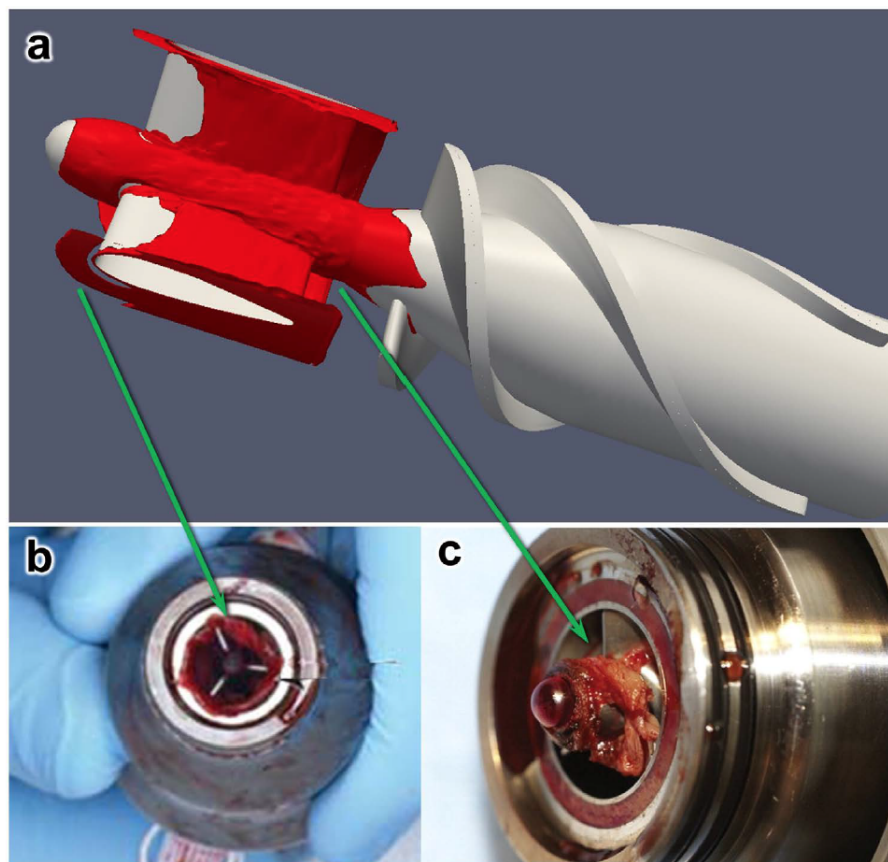


Fig. 1 a) Simulation numérique de la formation du thrombus basée dans l'activité plaquettaire, b) et c) sont des images cliniques. Le thrombus est formé en amont de l'entrée du dispositif d'assistance ventriculaire. Image issue de Wu et al. [8].

biomédicaux. Par ailleurs, la réduction des schémas cinétiques détaillés de la cascade de coagulation a été étudiée dans l'objectif de l'appliquer pour des écoulements complexes présents dans ce type d'appareils.

Après une introduction au sujet dans le Chapitre 1, le Chapitre 2 présente une stratégie numérique pour initier la cascade de la coagulation. La formation de thrombine dans la configuration académique de Taylor et al. [9] a été étudiée en utilisant une condition limite adaptée aux réactions surfaciques. Cette condition limite a été appliquée sur toute la paroi du domaine de calcul mais la création de thrombine n'est effective que dans certaines zones propices du point de vue de la mécanique des fluides (faible vitesse, recirculation). Pour modéliser la cascade de coagulation, le schéma cinétique de Chatterjee et al. [4] a été utilisé. Comme le montre la Fig. 2.8, les simulations produisent de fortes concentrations de thrombine dans la même région où le thrombus se forme lors de l'expérience en laboratoire

de Taylor et al. [9], alors que les réactions de coagulation sont déclenchées sur toute la paroi du domaine.

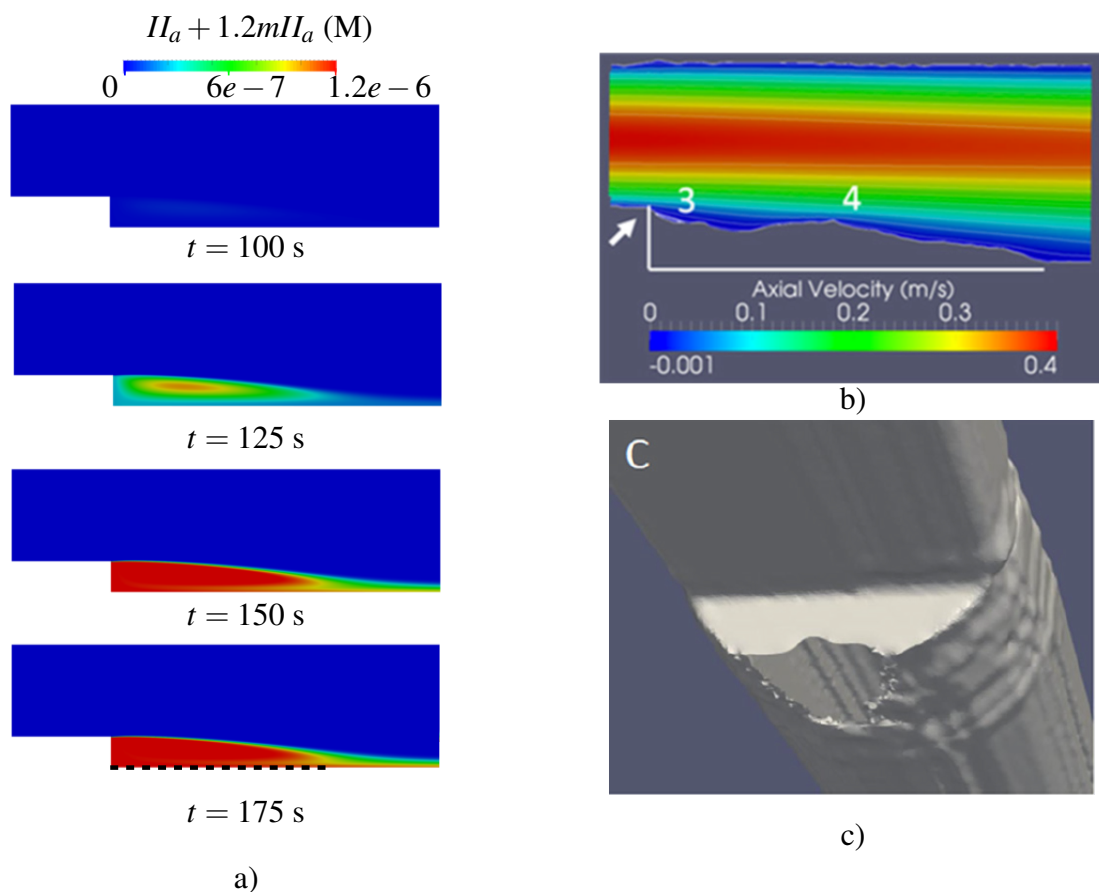


Fig. 2 a) Formation de thrombine à 100, 125, 150 et 175 s. b) Image issue de Taylor et al. [9] montrant le champ de vitesse autour du thrombus dans la configuration académique de la marche descendante. c) Forme tridimensionnelle du thrombus issue de Taylor et al. [9].

Dans le Chapitre 3, un nouveau modèle réduit pour la génération de thrombine est proposé en incluant l'activation par contact. Ce modèle est dérivé d'une analyse de sensibilité du modèle détaillé de Chatterjee et al. [4] en utilisant la méthode globale de Morris [10]. Le modèle arrive à prédire correctement la formation de thrombine dans du plasma physiologique et pour une gamme de plasma déficients en prothrombine. La figure 4 montre les résultats expérimentaux d'un test de génération de thrombine en incluant les résultats numériques du modèle réduit. De manière générale, un bon accord est observé avec une amplitude de génération de thrombine numérique légèrement plus faible pour le numérique. Cependant, la bonne tendance est reproduite par le modèle réduit.

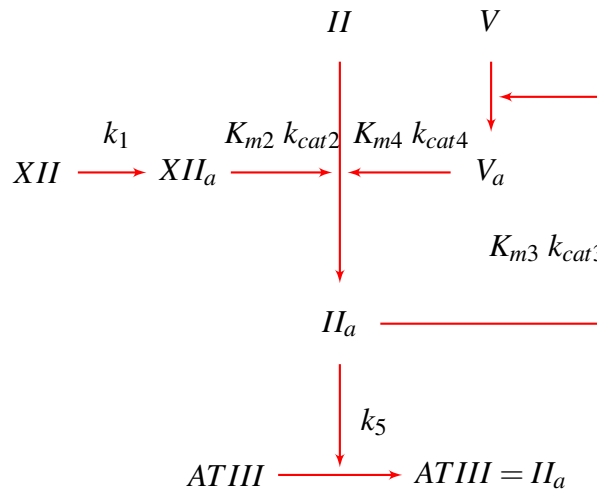


Fig. 3 Modèle réduit pour la génération de thrombine en incluant le système d’activation par contact. Le système de notation K_{mi} , k_{cati} suit la cinétique de Michaelis-Menten, la notation k_i indique une réaction de premier ordre.

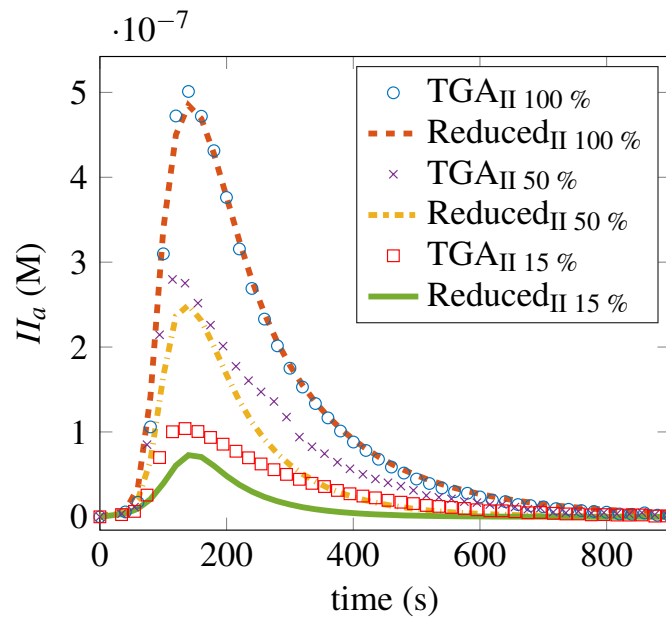


Fig. 4 Test de génération de thrombine dans du plasma déficient en prothrombine.

Dans le Chapitre 4 l’approche réduite est incluse dans le modèle de Taylor et al. [9] pour une croissance du thrombus basée sur l’activité des plaquettes. Cette nouvelle stratégie est utilisée pour calculer la formation du thrombus dans la même configuration académique du Chapitre 2. La Fig. 5 montre l’évolution du thrombus en utilisant le modèle de Taylor et al. quand la génération de thrombine est prise en compte par le modèle réduit en utilisant la

condition limite de paroi réactive.

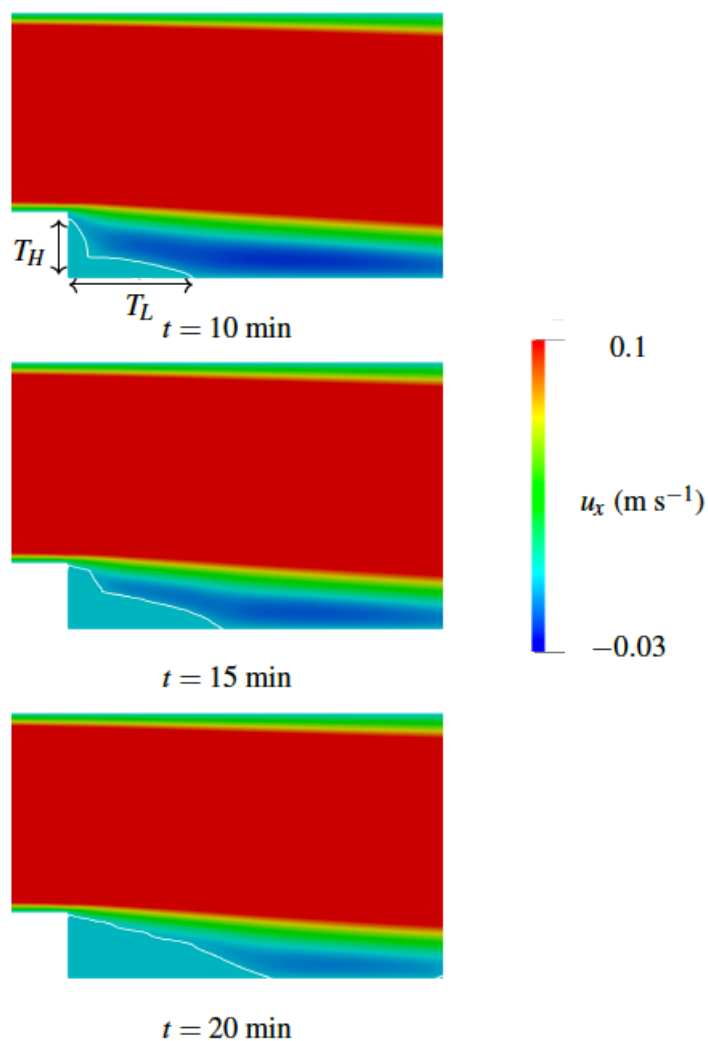


Fig. 5 Champs de vitesse scalaire dans la direction x (horizontal). La ligne blanche montre la limite de thrombus. Le thrombus se forme dans la même zone que dans l'expérience décrite dans Taylor et al. [9].

Les résultats numériques montrent une forte activation plaquettaire par la thrombine. La figure 6 montre la forte dépendance du modèle de Taylor et al. [11] (uniquement plaquettaire) à la valeur d'activation plaquettaire du sang entrant. Cette forte dépendance, pas justifiée d'un point de vue physique, est supprimée quand le modèle est couplé avec le schéma réduit de la cascade de coagulation. Les différentes valeurs d'activation plaquettaire utilisées sont détaillées dans le tableau 1.

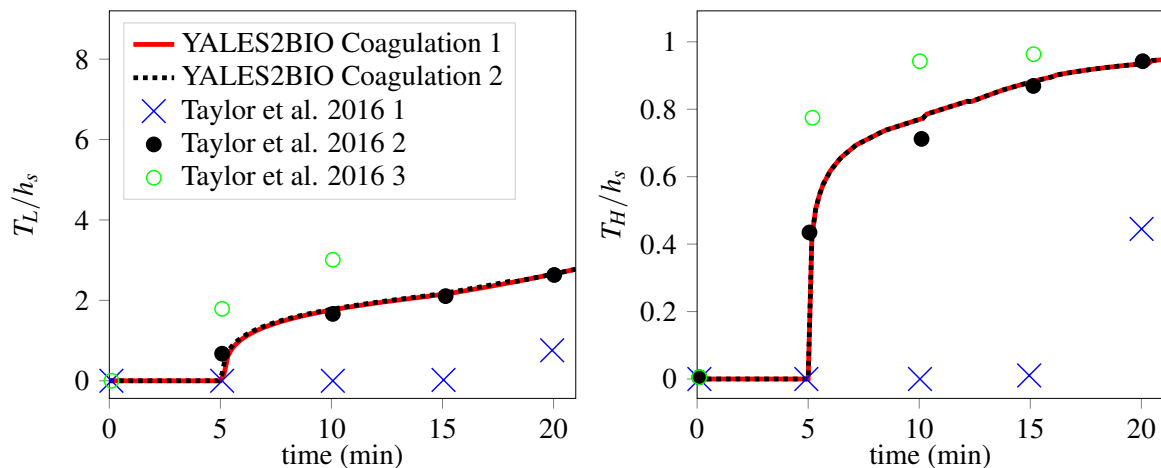


Fig. 6 Croissance de la taille du thrombus T_L et T_H pour different valeurs d'activation plaquettaire de fond.

Cas	Activation plaquettaire de fond (PLT m^{-3})
YALES2BIO Coagulation 1	2.5×10^{13}
YALES2BIO Coagulation 2	7.5×10^{13}
Taylor et al. [11] 1	1.5×10^{13}
Taylor et al. [11] 2	2.5×10^{13}
Taylor et al. [11] 3	3.7×10^{13}

Table 1 Niveaux d'activation plaquettaire de fond utilisées avec le modèle de Taylor et al. [11].

Bibliographie

[1] Wu, W. T., Jamiolkowski, M. A., Wagner, W. R., Aubry, N., Massoudi, M., and Antaki, J. F. (2017). Multi-constituent simulation of thrombus deposition. *Sc. Rep.*, 7.

[2] Yan, Y., Xu, L.-C., Vogler, E. A., and Siedlecki, C. A. (2018). *I - Contact activation by the intrinsic pathway of blood plasma coagulation*. Woodhead Publishing.

[3] Naudin, C., Burillo, E., Blankenberg, S., Butler, L., and Renné, T. (2017). *Factor XII Contact Activation*. Thieme Medical Publishers, Inc.

[4] Chatterjee, M. S., Denney, W. S., Jing, H., and Diamond, S. L. (2010). Systems biology of coagulation initiation: Kinetics of thrombin generation in resting and activated

human blood. *PLoS Comp. Biol.*, 6(9).

[5] Zhu, D. (2007). Mathematical modeling of blood coagulation cascade: kinetics of intrinsic and extrinsic pathways in normal and deficient conditions. *Blood. Coagul. Fibrinolysis.*, 18:637–646.

[6] Biasseti, J., Spazzini, P. G., Swedenborg, J., and Gasser, T. C. (2012). An integrated fluid-chemical model toward modeling the formation of intra-luminal thrombus in abdominal aortic aneurysms. *Front. Physiol.*, 3(266).

[7] Seo, J. H., Abd, T., George, R. T., and Mittal, R. (2016). A coupled chemo-fluidic computational model for thrombogenesis in infarcted left ventricles. *Am. J. Phys.*, 310(11):H1567–H1582.

[8] Wu, W. T., Yang, F., Wu, J., Aubry, N., Massoudi, M., and Antaki, J. F. (2016). High fidelity computational simulation of thrombus formation in thoratec heartmate ii continuous flow ventricular assist device. *Sc. Rep.*, 6:38025–1–11.

[9] Taylor, J., Witmer, K., Neuberger, T., Craven, B., Meyer, R., Deutsch, S., and Manning, K. B. (2014). In vitro quantification of time dependant thrombus size using magnetic resonance image and computational simulations of thrombus surface shear stresses. *J. Biomech. Eng.*, 136(7).

[10] Morris, M. (1991). Factorial sampling plans for preliminary computational experiments. *Technometrics*, 33:161–174.

[11] Taylor, J. O., Meyer, R. S., Deutsch, S., and Manning, K. B. (2016). Development of a computational model for macroscopic predictions of device-induced thrombosis. *Biomech. Model. Mechanobiol.*, 15(6):1713–1731.

Table of contents

List of figures	xvii
List of tables	xxiii
Nomenclature	xxv
1 Introduction	1
1.1 Motivations	1
1.2 Thrombosis Biology	2
1.2.1 Constitution of Blood	3
1.2.2 Coagulation cascade	4
1.2.3 Platelet activity	9
1.2.4 Von Willebrand factor	10
1.2.5 Blood flow influence in thrombosis	11
1.2.6 Inflammation and the complement system	13
1.3 Mathematical modeling: state of the art	15
1.3.1 Thrombus modeling in vivo	16
1.3.2 Thrombus modeling in medical devices	24
1.4 Flow solver YALES2BIO	30
1.5 Objectives of the thesis and chapter contents	32
2 The contact system in device-related thrombosis modeling	35
2.1 Introduction	35
2.2 Materials and Methods	37
2.2.1 Governing equations	37
2.2.2 Coagulation model	38
2.2.3 A boundary condition for the contact activation	40
2.2.4 Numerical implementation and verification	43
2.2.5 Backward facing step configuration	44

2.3	Results: Backward facing step	47
2.3.1	Flow Dynamics	47
2.3.2	Coagulation cascade	48
2.3.3	Parametric studies	51
2.4	Discussion and Conclusion	54
3	Sensitivity analysis and model reduction	59
3.1	Introduction	59
3.2	Methods	61
3.2.1	Plasma Samples and TGA	61
3.2.2	Detailed coagulation model	62
3.2.3	Morris Sensitivity Analysis	65
3.2.4	A reduced model of coagulation initiated by contact activation . . .	69
3.2.5	Bayesian parameter inference	71
3.3	Results	73
3.3.1	Sensitivity Analysis of the full coagulation model	73
3.3.2	Reduced model for thrombin generation	75
3.4	Discussion	79
4	Thrombus growth and its influence on the flow	83
4.1	Introduction	83
4.2	Platelet-based model description and implementation	84
4.2.1	Species transport and platelet activation	85
4.2.2	Aggregation intensity and the impact of the thrombus in the flow .	87
4.2.3	Code verification	89
4.2.4	Verification: Backward facing Step Application	90
4.3	Including the coagulation cascade	95
4.4	Discussion	97
5	Conclusions and Perspectives	101
5.1	Main results	101
5.2	Perspectives	102
	References	105

List of figures

1	a) Simulation numérique de la formation du thrombus basée dans l'activité plaquettaire, b) et c) sont des images cliniques. Le thrombus est formé en amont de l'entrée du dispositif d'assistance ventriculaire. Image issue de Wu et al. [8].	viii
2	a) Formation de thrombine à 100, 125, 150 et 175 s. b) Image issue de Taylor et al. [9] montrant le champ de vitesse autour du thrombus dans la configuration académique de la marche descendante. c) Forme tridimensionnelle du thrombus issue de Taylor et al. [9].	ix
3	Modèle réduit pour la génération de thrombine en incluant le système d'activation par contact. Le système de notation K_{mi} , k_{cati} suit la cinétique de Michaelis-Menten, la notation k_i indique une réaction de premier ordre.	x
4	Test de génération de thrombine dans du plasma déficient en prothrombine.	x
5	Champs de vitesse scalaire dans la direction x (horizontal). La ligne blanche montre la limite de thrombus. Le thrombus se forme dans la même zone que dans l'expérience décrite dans Taylor et al. [9].	xi
6	Croissance de la taille du thrombus T_L et T_H pour different valeurs d'activation plaquettaire de fond.	xii
1.1	Hemostatic response illustrated by a blood clot formation at the injury site. The image is taken from [44].	3
1.2	Circulating human blood scanned with an electron microscope (left) and an illustration of the blood composition (right). The image is taken from [103].	4
1.3	Schematic of thrombus formation in medical devices, coagulation is triggered by the artificial surface. The image is taken from Jaffer et al. [60].	5
1.4	Intrinsic pathway based on the model presented by [29] following the traditional biochemical picture of the coagulation cascade.	6
1.5	Extrinsic system, sometimes referred to as TF pathway [58].	7

1.6	Complete coagulation cascade including the intrinsic, extrinsic and common pathways showing the role of the coagulation inhibitors.	9
1.7	VWF below and above the critical shear rate (upper part show a graphic representation and lower image is a fluorescence) these images are reproduced from [99]	11
1.8	Platelet activation in terms of shear-related serotonin release for platelets (red blood cells hemolysis also shown) as a function of exposure time, graph taken from [54]. Different shear conditions for different biomedical devices are shown.	12
1.9	Complement system diagram from [47] (Kirschfink M).	14
1.10	Time line of thrombus formation and the main biological events that lead to a stable thrombus.	15
1.11	Active thrombin as a function of time presented in [57] for numerical (A) and experimental results (B). The curves correspond to a range of prothrombin concentrations [$0.7 \mu\text{M} \sim 2.1 \mu\text{M}$]. Numerical results of (C) are obtained for small variations of factor V_a showing little influence on the results.	17
1.12	Two transport zones as showed in [13]	18
1.13	Thrombus growth sequence in a blood vessel from [41]. The red and yellow color field show the platelets aggregation intensity field.	19
1.14	Thrombus development from [70] at different instants starting until $t = 600$ s using a TF concentration of 15 fmol cm^{-2}	20
1.15	Platelet aggregation at high shear rates in an stenosed channel, a) view normal to the flow b) above view, c) experimental and numerical results with uncertainties for normalized platelet density. The image is taken from [126]	21
1.16	Vortex educed using λ_2 criteria carrying thrombin in a characteristic counter-clockwise trail taken from [18]	23
1.17	Spatial distributions of three flow-dased criteria for thrombosis risk. Endothelial cell activation potential (ECAP), platelet activation potential (PLAP), thrombus formation potential (TFP). The image was taken from [1].	24
1.18	a) Numerical simulation of thrombus formation based on platelet activity b) and c) are clinical images. The results show significant deposition upstream of the inlet straightener vane (zone of low WSS not shown). The image is taken from [121].	26
1.19	Growing thrombus at a backward facing configuration. a) axial velocity b) shear stress. The platelet clot is represent by a white contour plot computed with a aggregation intensity threshold. The image is taken from [112].	27

1.20	Macroscopic examples of blood flows in A) Mechanical artificial heart valve computation without thrombosis from [106] (Iso-surfaces of the instantaneous Q criterion is shown). B) Velocity field inside a patient-specific left ventricle from [34].	31
2.1	Schematic of the coagulation reaction network. The kinetic network is inspired from the platelet-plasma model of Chatterjee et al. [30] without considering TF, inhibitors and fibrinogen reactions. The dashed lines correspond to the feedback loop reactions related to thrombin.	39
2.2	Mass balance around the device wall. Ω Control of volume, Σ Surface envelope of the control volume, Sub index <i>in</i> , <i>s</i> and <i>l</i> stand for the inferior, superior and lateral surfaces respectively, <i>h</i> height of the control volume. . .	42
2.3	1D reaction-diffusion test case. $C_A = \alpha = 1.0 \mu\text{M}$, initial volume concentration of all the species $C_i = 0 \text{ M}$, diffusion coefficient of species $D_A = D_B = 1.0 \times 10^{-2} \text{ m}^2 \text{ s}^{-1}$, channel height $h = 0.01 \text{ m}$. Numerical results (<i>Case</i> ₁ \circ , <i>Case</i> ₂ \diamond , <i>Case</i> ₃ \square) and analytic Eq. 2.10 data (<i>Case</i> ₁ $\cdots\cdots$, <i>Case</i> ₂ --- , <i>Case</i> ₃ $\cdots\cdots$).	45
2.4	2D Backward facing step computational domain. P_i are the locations of the probes used in Figs. 2.5, 2.7 and Fig. 2.12 ($P_1 = (0.5, 0.5)$, $P_2 = (4.0, 1.5)$, $P_3 = (4.0, 4.0)$ mm); the step and channel heights match the experimental values of Taylor et al. [111]. The thick black line denotes the solid boundary where boundary condition Eq. 2.9 is applied and activation of factor XII is allowed.	45
2.5	Temporal evolution of <i>x</i> and <i>y</i> velocity components in different point probes.	47
2.6	Velocity magnitude with white stream lines. The reattachment length X_r is shown.	47
2.7	Time evolution of $II_a + 1.2mII_a$ for each point probe (see Fig. 2.4). P_1 is near the wall region, P_2 inside the recirculation zone and P_3 outside the recirculation region.	48
2.8	a) Total thrombin concentration field at $t = 100, 125, 150$ and 175 s . The black dashed line represents over which total thrombin is plotted in Fig. 2.9. b) is taken from Taylor et al. [111] showing the velocity field around the thrombus at the BFS (inside the thrombus the velocity is not showed) c) the 3-dimensional form of the thrombus is showed, again the image is taken from Taylor et al. [111]	49
2.9	$II_a + 1.2mII_a$ concentration in the recirculation zone.	50

2.10	Simulations including inhibitor <i>ATIII</i> and related reactions. a) Thrombin concentration at $t = 400$ s is shown in the upper part. b) Evolution of thrombin concentration at point probes P_1 and P_2 is shown in the lower part.	51
2.11	Scatter plot of wall shear stress and wall concentrations of factors XII_a and XI_a	52
2.12	Time evolution at point probe P_1 of total thrombin (upper), activated factor XII (medium) and activated factor XI (bottom). $k_s = 5 \times 10^{-5}$ (·····), $k_s = 5 \times 10^{-6}$ (·-·-·), $k_s = 5 \times 10^{-7}$ (—), $k_s = 5 \times 10^{-8}$ (·····), $k_s = 5 \times 10^{-9}$ (- - -), $k_s = 5 \times 10^{-10}$ (- -). The insets of $II_a + 1.2mII_a$ and XII_a factor show the Inflection Point Time (IPT) for each k_s value. For factor XI_a , the inset displays the maximum concentration time (MCT) as a function of k_s	53
2.13	Time evolution of point probe P_1 for total thrombin (upper), activated factor XII (medium) and activated factor XI (bottom) at point probe P_1 . The inlet and initial concentrations are $XII_{90\%} = 0.306 \mu M$ (- - -), $XII_{70\%} = 0.272 \mu M$ (·-·-·), $XII_{50\%} = 0.17 \mu M$ (—), $XII_{30\%} = 0.102 \mu M$ (·····).	55
2.14	Maximal total thrombin concentration inside the recirculation region for three orders of magnitude of the diffusion coefficients ($D_i \sim 10^{-8}, 10^{-7}, 10^{-6} \text{ m}^2 \text{ s}^{-1}$).	56
3.1	Experimental results of thrombin generation assay (left) and numerical simulation using the kinetic scheme of Table 3.1 with the initial conditions of Table 3.2.	66
3.2	2D parameter grid, the levels are mapped using the log uniform distribution. Two trajectories are shown as an illustration of the OAT random advancement.	67
3.3	Variables used in the sensibility analysis: t_{lag} , $\max(II_a)$, m_1 , m_2 , ETP.	68
3.4	Reduced model for thrombin generation triggered by the contact activation system. The notation K_{mi} , k_{cati} is used for reaction following Michaelis–Menten kinetics while k_i are first order reactions.	70
3.5	Morris analysis for each QoI σ_j and μ_j^* are computed. The rectangle represent the threshold retention zone, the parameter with effects larger than $0.3 \times \max(\sigma_j)$ and $0.3 \times \max(\mu_j^*)$ are considered relevant. A histogram showing how many QoI are sensitive to each parameter is also shown (bottom right).	74
3.6	Sobol coefficients of the 63 parameters for t_{lag} calculated with 126 Stroud data points, with Legendre Polynomials. Coefficients marked with x are responsible for 80% of the output variance	76

3.7	Mean of the eight TGA data sets for physiological data and numerical thrombin formation using the reduced model (Fig. 3.4) with optimal parameters from Bayesian inference. The error bars represent the variance of the TGA data sets. The optimal parameters were obtained after 20000 MCMC iterations.	77
3.8	Experimental TGA and numerical data using the reduced model with optimal parameters of Table 3.4 for a range of factor II initial concentrations, 100% =physiological PPP concentration, 50%, 15%)	78
3.9	Numerical results of the detailed model of Chatterjee et al. [30] and numerical data using the reduced model with optimal parameters of Table 3.5 for a range of factor II initial concentrations, 100% =physiological PPP concentration, 50%, 15%)	79
4.1	Batch test case verification of chemical activation of platelets by ADP. Time evolution of activated platelets fraction $\frac{C_{AP}}{C_{NP}+C_{AP}}$ (—), non activated platelets fraction $\frac{C_{NP}}{C_{AP}+C_{NP}}$ (.....) and normalized ADP $\frac{C_{ADP}}{C_{ADP}^{thr}}$ (○) (right y axis)	90
4.2	Backward facing step computational domain based on [111]	91
4.3	Field of scalar stress, activation taking place at zones of high τ	91
4.4	Velocity field in x direction with white contour of ε_t showing the thrombus. The general agreement is fair.	92
4.5	The numerical results from the current implementation of the model from [112] compared against numerical and experimental results	93
4.6	Platelet aggregation scalar field ε , a second thrombus formed at the reattachment point, this effect is not observed in the experimental configuration of [111].	93
4.7	Platelet agregation intensity at $t = 340$ s, a) case with inlet perturbations b) constant velocity inlet.	94
4.8	Numerical results with coagulation, platelet-based model [112] and experimental results from [111]	96
4.9	Thrombin field at $t = 50$ s, the thrombin activation threshold $C_{II_a}^{thr} = 0.833$ nM is reached in the step lower corner and inside the recirculation region	97
4.10	a) Thrombin concentration (nM) at 60 s b) Activated platelet fraction ϕ_f at 60 s.	98
4.11	Background activation dependency on platelet for the values of background platelet activation from Table 4.8.	99

List of tables

1	Niveaux d'activation plaquettaire de fond utilisées avec le modèle de Taylor et al. [11].	xii
1.1	Circulating inactive coagulation factors and their mean physiological concentration in blood. The values are taken from [22].	4
1.2	Interactions between complement and coagulation systems [47]	14
1.3	Summary of the existing models highlighting their general features.	29
2.1	Coagulation reactions. Kinetic parameters and coagulation reactions used in the simulations. Reaction 14 is taken into account only at the surface by means of the wall boundary condition. Parameter k_s units (m s^{-1}) correspond to a surface reaction; its value was obtained by adapting the volume reaction rate from Chatterjee et al. [30].	41
2.2	Operating points. The different set of parameters (k_s and k_v) used for the verification of the code. The corresponding steady state solutions are shown in Fig. 2.3.	44
2.3	Initial and inlet factor concentrations. Physiological values used in the simulations taken from Chatterjee et al. [30].	46
2.4	Mesh properties. Δ_h is the representative cell size computed as in Celik et al. [27] and the total number of grid elements (triangles) are displayed.	46
2.5	Factor XII inlet concentrations used in the parametric study. These values correspond to 90%, 70%, 50% and 30% of the nominal concentration reported in Table 2.3.	54
3.1	Kinetic parameters and coagulation reactions used in the simulations. The model of Chatterjee et al. [30] was adapted to the experimental conditions detailed in Section 3.2.1.	63

3.2	Factors concentrations based on TGA (concentrations are calculated after sample mixing with fluorescent reagent and using the values reported by Cryopep, Montpellier France) used as initial conditions in the numerical simulations.	65
3.3	Reduced kinetic model for the coagulation cascade showed in Fig. 3.4. Reactions 1 and 5 are first order reaction, reactions 2, 3 and 4 follow Michaelis–Menten kinetics.	70
3.4	Optimal parameters obtained from Bayesian inference; the initial concentration of prothrombin $C_{II} = 933.0$ nM is not infered.	77
3.5	Optimal parameters obtained from Bayesian inference using the numerical data of the detailed model of Chatterjee et al. [30]. The initial concentration of prothrombin $C_{II} = 933.0$ nM is not infered.	78
4.1	Parameters involved in the source terms and transport of species in the model of Taylor et al. [112].	86
4.2	Parameters use to calculate thrombus deposition and growth, all of the parameters are taken from [112].	89
4.3	Initial conditions of platelets and ADP used to solve Eq. 4.13 considering only platelet chemical activation. PLT m^{-3} stand for platelet count per unit of volume. Initially $C_{ADP} = C_{ADP}^{thr}$	89
4.4	Inlet and initial conditions of platelets and ADP used in the BFS benchmark.	91
4.5	Perturbations frequencies and amplitudes used at the velocity inlet boundary condition. These values were arbitrary chosen.	94
4.6	Reduced kinetic model for the coagulation cascade showed in Fig. 3.4. Reaction 1* is a first order surface reaction, reactions 2, 3 and 4 follow Michaelis–Menten kinetics, finally, reaction 5 is first order	95
4.7	Initial and inlet concentrations used in BFS benchmark simulation including thrombin formation due to coagulation. The values are taken from the reduced kinetic model developed in Chapter 3.	96
4.8	Background activation of platelets used in YALES2BIO simulations including platelet activation by thrombin and three cases computed by Taylor et al. [112].	98

Nomenclature

Coagulation Factors

ATIII Antithrombin

HMWK High molecular weight kininogen

I Fibrinogen

I_a Fibrin

II Prothrombin

II_a Thrombin

IX Christmas factor

K Kallikrein

PK Prekallikrein

TF Tissue Factor (Factor *III*)

TFPI Tissue Factor Pathway Inhibitor

V Labile factor

VII Proconvertin

VIII Antihæmophilic factor

X Stuart-Power factor

XI Plasma thromboplastin antecedent

XII Hageman (contact factor)

XIII Fibrin-stabilizing factor

Acronyms / Abbreviations

AAA Abdominal Aortic Aneurysm

ADP Adenosine diphosphate

BFS Backward Facing Step

CAT Calibrated Automated Thrombogram

CFD Computational Fluid Dynamics

CFL Courant-Friedrichs-Levy stability condition

CGI Convergence Grid Index

DoE Design of Experiments

ETP Endogenous Thrombin Potential

FVM Finite Volume Method

GP Glycoprotein

MCMC Markov Chain Monte Carlo

NS Navier-Stokes

OAT One at A Time

ODE Ordinary Differential Equation

PDE Partial Differential Equation

PNP Platelet Normal Plasma

PPP Platelet Poor Plasma

QoI Quantity of Interest

RBC Red Blood Cell

SS Shear Stress

TGA Thrombin Generation Assay

TG Thrombus Growth

VAD Ventricular Assist Device

VWF Von Willebrand Factor

WSS Wall Shear Stress

Chapter 1

Introduction

In this chapter, a general introduction of the thesis is developed. First, the motivations of the work are presented. Then, the biological processes that take place in thrombosis are introduced. A literature review on thrombosis modeling is done for both injury-related and device-related thrombosis. Finally, the thesis structure is presented, listing the principal objectives and contributions of each chapter.

1.1 Motivations

The use of blood-coated medical devices has emerged over the last decades [110, 2, 16, 64]. This type of devices are used to treat different types of pathologies such as:

- Heart-related conditions
 - Heart failure which is treated with ventricular assist device (VAD), total artificial heart (TAH)
 - Heart valve disease in which mechanical valves or bioprosthetic valves are used
- Cerebrovascular conditions
 - Brain Aneurysm treated with coils, stent, flow diverter
 - Stenosis treated using balloon angioplasty stenting

The efficiency of these devices has improved over the last years. However, there is not a biomaterial surface that prevents the initiation of blood coagulation or platelet adsorption due to the lack of non-thrombotic properties of the endothelium in the biomaterial. In some cases,

thrombus formation is desired: in cerebral aneurysm for example, thrombus growth maybe triggered as a treatment to prevent aneurysm rupture [87]. However, in other devices such as heart valves, blood pumps or vessel grafts, clinical complications may arise, as pointed out by different authors [28, 119, 75]. One of the major challenges of device manufacturers is to develop strategies that increase the hemocompatibility of devices to improve the treatment success rate. The main objective of the current work is to develop a mathematical model that helps to understand and predict the formation of thrombus in blood-coated devices contributing with the long-term goal of optimizing these devices.

1.2 Thrombosis Biology

In its normal state, blood is pumped inside the cardiovascular network. The first layer of most of the vessels wall, named endothelium, has non-thrombotic properties. The endothelial cell functions influences thrombosis through the secretion of mediators such as: thrombomodulin, antithrombin, plasminogen activator, heparin, thromboxane A₂ leukotrienes which prevent the spontaneous creation of a blood clot [45]. When the endothelium is damaged, a biological response called hemostasis takes place to preserve the integrity of the vessel wall. The hemostatic response involves different biological processes that form a blood clot which prevents the blood from leaving the vessel. This process searches an equilibrium in order to preserve the vessel wall integrity without occluding the vascular duct as shown in Fig. 1.1.

When hemostasis is not well regulated, several disorders can take place like thrombosis (excessive clot formation known as thrombus) or hemorrhagic disorders (like hemophilia or von Willebrand disease). In the case of thrombosis, blood clots can form mural thrombus (thrombus at the vessel wall), emboli (a detached part of a thrombus) or occlusive thrombus. Hoffbrand and Moss [58] define the hemostatic system as a delicate balance between pro-coagulant and anticoagulant mechanisms allied to a fibrinolysis process that allows for an efficient and rapid mechanism for stopping bleeding from sites of blood vessel injury. Some of the major biological components involved in hemostasis are:

- Coagulation cascade
- Platelet activity (adhesion, activation, aggregation)
- Blood flow (mass transport)
- Inflammation and other minor processes

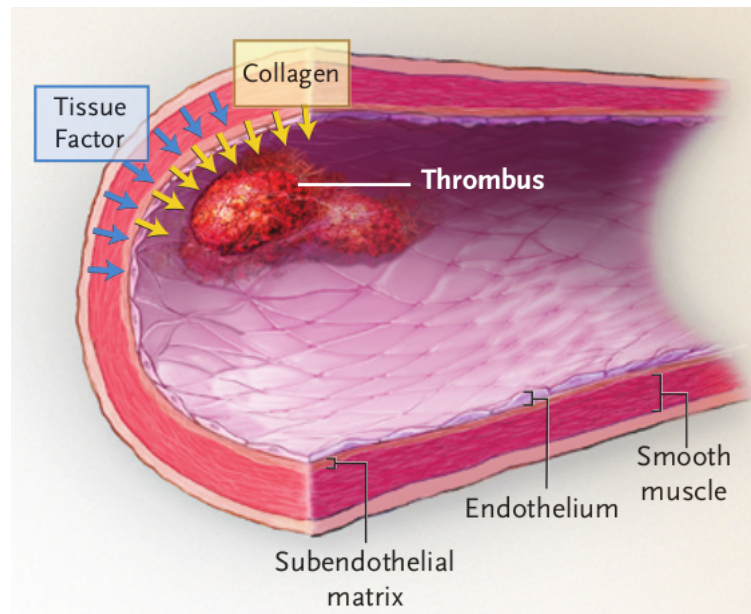


Fig. 1.1 Hemostatic response illustrated by a blood clot formation at the injury site. The image is taken from [44].

Through these biological mechanisms, a platelet plug is formed. Simultaneously, thrombin produced in the coagulation cascade transforms fibrinogen into fibrin which meshes the platelet plug. Then, a complicated interaction between the platelet plug and fibrin nets takes place continuously to form a stable blood clot (thrombus). Even though the biological processes involved in thrombus formation take place at the same time, for the sake of understanding, they will be presented separately.

1.2.1 Constitution of Blood

Blood is a complex fluid mainly composed of plasma, platelets, red and white blood cells which are suspended as shown in Fig. 1.2. Plasma constitutes 55 % of the total blood volume and is mainly composed of water (up to 95 %) along with different substances, such as dissolved proteins (6-8 %), glucose, coagulation factors, electrolytes, hormones, carbon dioxide and oxygen. Coagulation factors are enzymes and zymogens that circulate in their inactivated state. Upon a specific biochemical signal, they initiate a series of biochemical reactions that contribute to form the blood clot. The coagulation factors that circulate in blood in their inactive form are listed in Table 1.1. The remaining 45 % of the volume is composed of platelets, white blood cells and mainly Red Blood Cells (RBC).

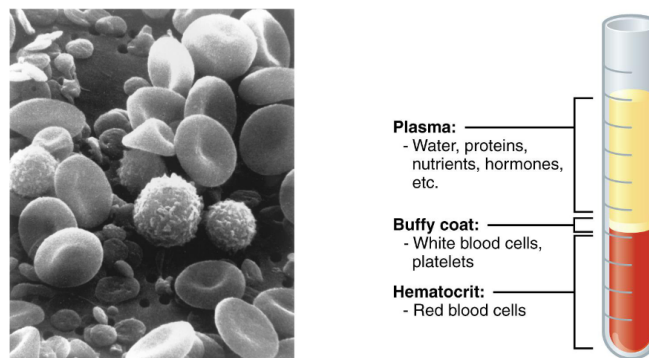


Fig. 1.2 Circulating human blood scanned with an electron microscope (left) and an illustration of the blood composition (right). The image is taken from [103].

Factor	Names	Physiological mean	Clinically range
<i>II</i>	Prothrombin	1.4 μM	0.8-2.0
<i>V</i>	Labile factor	20 nM	12-28
<i>VII</i>	Proconvertin	10 nM	6-14
<i>VIII</i>	Antihaemophilic factor	0.7 nM	0.4-1.6
<i>IX</i>	Christmas factor	90 nM	62-135
<i>X</i>	Stuart-Power factor	160 nM	96-224
<i>ATIII</i>	Antithrombin	3.6 μM	3.2-6.3
<i>TFPI</i>	Tissue Factor Pathway Inhibitor	2.5 nM	1.1-4.3

Table 1.1 Circulating inactive coagulation factors and their mean physiological concentration in blood. The values are taken from [22].

1.2.2 Coagulation cascade

In the classical view of the coagulation cascade, when the endothelium is damaged, tissue factor (TF) is exposed triggering a cascade of enzymatic reactions that generate thrombin. This cascade of reactions is known as the coagulation cascade, which is divided into three pathways: extrinsic (or TF) pathway, the intrinsic pathway (which can be triggered by foreign surfaces without endothelial properties) and the common pathway. The extrinsic and the intrinsic pathway taking place separately merge in their final part at the common pathway. Here, the classical view of the coagulation cascade is presented [58]. However, new enzymatic reactions and interactions between factors are still being discovered [23].

Intrinsic pathway

In vivo, the intrinsic pathway is initiated by blood exposure to a negatively charged surface such as collagen or by artificial surfaces, as shown in Fig. 1.3. Several surfaces that can initiate this pathway have been identified, including collagen, nucleic acids, platelet and microbial polyphosphate, as pointed out by Naudin et al. [85]. In the case of a medical device, when an artificial surface is present in the blood flow, proteins like albumin, fibrinogen, factor *XII* or *HMWK* rapidly adhere to it, forming a protein layer. The protein layer evolves dynamically in what is called the Vroman effect [115]. In whole blood, several proteins compete to occupy free sites at the artificial surface. In particular, the adsorption rate of factor *XII* will directly influence the initiation of the intrinsic pathway by the contact activation system.

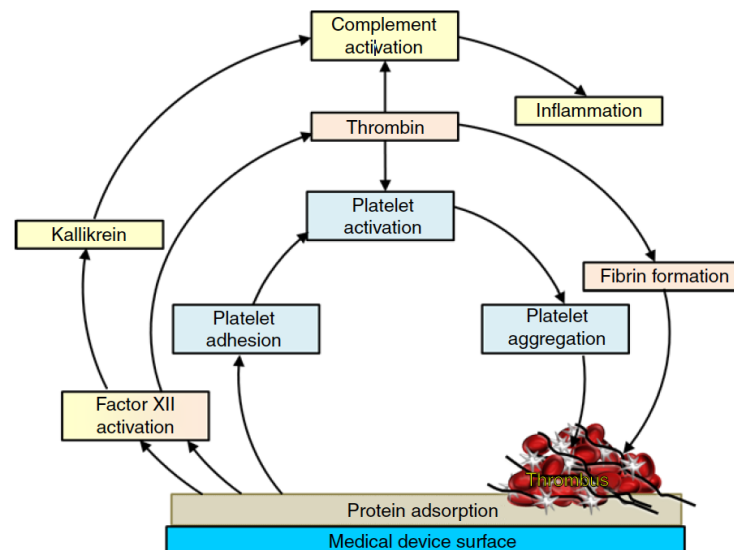


Fig. 1.3 Schematic of thrombus formation in medical devices, coagulation is triggered by the artificial surface. The image is taken from Jaffer et al. [60].

Figure 1.4 shows the intrinsic pathway. This pathway is triggered by factor *XII* auto-activation in a negatively charged surface. Two other enzymatic reactions that activate factor *XII* exist, auto-hydrolysis (activation by XII_a) and reciprocal activation by Kallikrein. At the negatively charged surface, high molecular weight kininogen (*HMWK*) binds to prekallikrein (*PK*) and to factor *XI*. Once *PK* binds to *HMWK* it transforms into Kallikrein (*K*). In addition, *K* transforms factor XII_a to XII_f (fragmented) which interacts with the complement system (see Section 1.2.6). Activation of factor *XI* to XI_a by factor XII_a marks the end of the contact activation system. The intrinsic system continues with the activation of factor

IX to IX_a by the action of factor XI_a . Factor IX_a forms a complex with calcium ions (Ca^{2+}) and $VIII_a$ (which is activated by thrombin and factor X_a). This complex is also known as the intrinsic Tenase complex. Finally, complex $IX_a = VIII_a = Ca^{2+}$ activates factor X . The intrinsic and extrinsic pathways merge in the production of factor X_a .

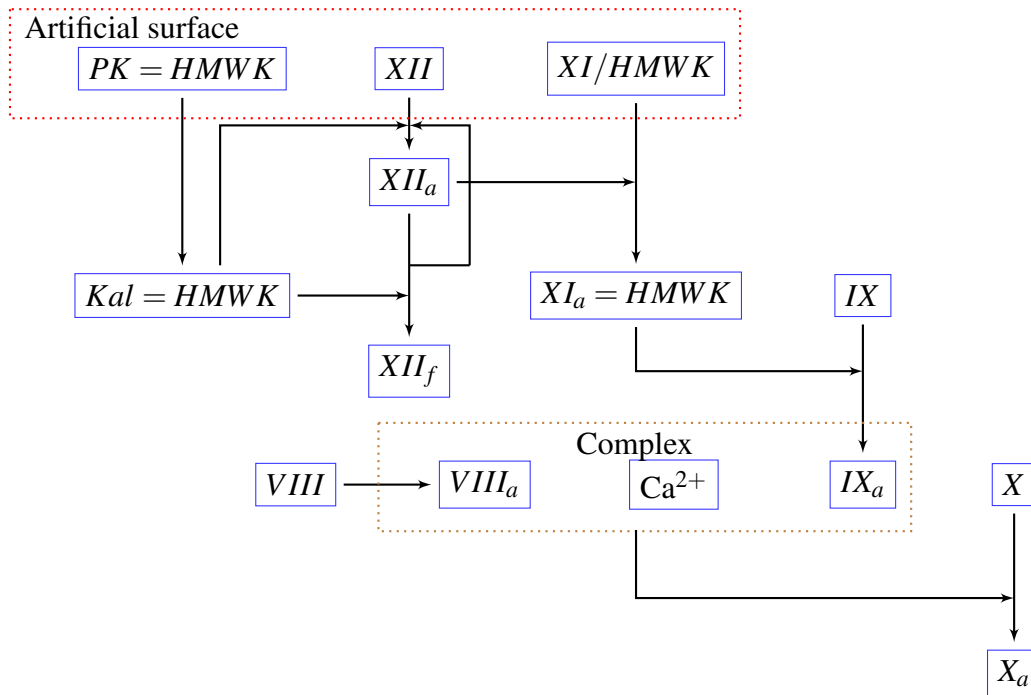


Fig. 1.4 Intrinsic pathway based on the model presented by [29] following the traditional biochemical picture of the coagulation cascade.

Historically, the importance of the intrinsic pathway remained speculative because patients with factor XII deficiency did not present bleeding disorders. On the other hand, patients lacking of factor VII (initial enzyme in the extrinsic system) show bleeding disorders, suggesting that the contact system had a minor role in haemostasis and therefore in thrombosis as well. It was not until the work of Renné et al. [95] that the importance of the contact system for thrombus formation was elucidated. Renné and co-workers showed that infusion of human factor XII into murine blood lacking of factor XII resulted in a restitution of thrombotic activity. These findings suggest that contact activation is crucial for thrombosis and thus relevant to biomedical devices due to factor XII activation in most of the materials used.

Extrinsic pathway (Tissue factor pathway)

As shown in Fig. 1.5, the extrinsic pathway is triggered by the presence of Tissue Factor, which is present at the sub-endothelium layer or expressed by activated platelets and leukocytes. TF is released in response to wall vessel damage. When TF is exposed to blood flow, it binds to plasma factor VII to form the $TF = VII$ complex. $TF = VII$ complex promotes the activation of factor VII forming the complex $TF = VII_a$. It is important to mention that pico-molar concentrations of VII_a circulate normally in the blood thus allowing, in the presence of TF , the direct formation of $TF = VII_a$ complex [47]. In the presence of calcium (Ca^{2+}) and phospholipids, the $TF = VII_a = Ca^{2+}$ complex, also known as the extrinsic 'tenase' complex, activates factor X . As pointed out before, here is where the intrinsic and extrinsic pathways come together. In addition, $TF = VII_a = Ca^{2+}$ complex can activate factor IX , hence communication between extrinsic and intrinsic systems takes place. This pathway is also relevant to blood coated medical devices since TF expression by monocytes was observed by Wilhelm et al. [117] and correlated to the presence of bio-materials. Also, TF can be released during device implantation which could also induce the initiation of the coagulation cascade.

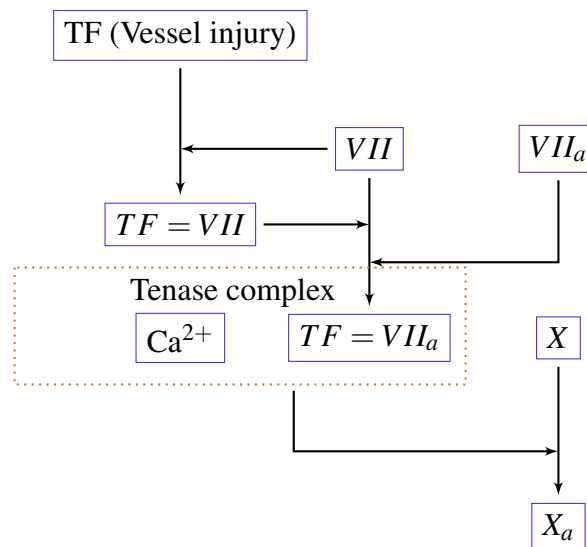


Fig. 1.5 Extrinsic system, sometimes referred to as TF pathway [58].

Common pathway

In the final part of the coagulation cascade factor X_a forms a complex with activated factor V_a . In the presence of calcium, the prothrombinase complex $X_a = V_a$ converts prothrombin into

thrombin which is the key enzyme in the coagulation process due to its multiple interactions with various systems and factors. Thrombin cleaves activation peptides from fibrinogen to form fibrin monomers and activates factor *XIII* that adds mechanical structure to the fibrin (through cross-linking). Furthermore, thrombin is a powerful activator of platelets, together platelets and fibrin form the stable blood clot [44]. Figure 1.6 shows the common pathway and thrombin amplification feedback loops such as activation of factor *V*, factor *XI* and factor *VIII*.

Inhibitors of coagulation

The coagulation cascade has many feedback loops that amplify the production of thrombin. A counterpart that blocks the amplification loops is the presence of coagulation inhibitors in blood that help reaching a hemostatic balance. The main inhibitors of coagulation are:

- **Protein C** is a vitamin K-dependent protein that inactivates factors V_a and $VIII_a$.
- **Antithrombin** (*ATIII*) neutralizes factor X_a and II_a by forming a complex. It is also capable of inhibiting factors IX_a , XI_a and XII_a .
- **Tissue factor pathway inhibitor** (*TFPI*) is the main inhibitor of the $TF = VII_a$ complex and of factor X_a . *TFPI* is present on the luminal surface of the vascular endothelium, and in platelets, monocytes and plasma.

Fibrin Formation

Fibrin along with activated platelets form the hemostatic clot that prevents blood loss. The fibrinogen conversion to fibrin is catalyzed by thrombin. In parallel, thrombin activates factor *XIII* that will promote fibrin cross-links leading to a mechanical stable blood clot. This could be considered as the final event of the thrombus formation process. However, it is important to mention that Fibrinolysis and Thrombolysis (enzymatic degradation of fibrin and thrombin) can occur in a longer process mediated by plasmin. This process is often used with therapeutic means to prevent thrombosis. Figure 1.6 shows the coagulation cascade involving the three pathways previously mentioned and the coagulation inhibitors.¹

¹A really good graphical effort from the Johns Hopkins University to explain the coagulation cascade can be found in <http://www.hopkinsmedicine.org/hematology/Coagulation.swf>

A_2 or serotonin can activate platelets through different pathways, which may lead to auto-activation loops. Another platelet activation mechanism is due to the interactions with the Von Willebrand factor (VWF) through glycoprotein Ib receptor and glycoprotein VI with collagen; this pathway is independent of thrombin and its result is the adhesion of platelets to the injury. Platelets can also be mechanically activated by the flow due to shear. Hellums [54] identifies a shear stress threshold for platelet activation that depend on the stress magnitude and the exposure time. Activated and non-activated platelets aggregate at the injury site and form, along with fibrin, the hemostatic clot. The natural inhibitors of platelet function are Nitric oxide (NO) and Prostacyclin which are released by endothelial cells; both promote vasodilatation and inhibit platelet activation according to Galley and Webster [45].

Platelet activation has been observed in several clinical procedures and bio-mechanical devices due to high shear stress (SS). It has been reported by [89] that mechanical activation of platelets can trigger chemical activation feedback loops. Platelets can also adhere to bio-material surfaces and activate through their interaction with different glycoprotein (GP) receptors. In-vivo, the bouncing off or adhesion of platelets to the thrombus is regulated by the interactions of GPIb\IIIa complex with fibrinogen and Von Willebrand factor (VWF). In-vitro platelet adhesion depends on the material adhesive properties which will determine the rate of protein adsorption to the device surface [113]. According to Taylor et al. [112], at low shear regions platelet adhesion is mediated by fibronectin, vitronectin and fibrinogen. At medium shear rates fibrinogen is the primary mediator. It is likely that at shear rates greater than 5000 s^{-1} VWF is the dominant adhesion mediator [97, 99]. In hemodynamic regimes with high shear rates, "white clots" primarily composed of platelets are observed [26].

1.2.4 Von Willebrand factor

At high shear rates ($\dot{\gamma}_{crit} > 5000 \text{ s}^{-1}$), thrombus formation is dominated by platelet accumulation as explained by [26]. Shear dependent platelet adhesion and aggregation is highly regulated by VWF. Increasing the shear rate above $\dot{\gamma}_{crit}$ induces a shape transformation of VWF to a stretched form with a larger length of ($l \sim 15 \mu\text{m}$). At shear rates below $\dot{\gamma}_{crit}$, VWF has a compact conformation with an estimated diameter size of $d \sim 2 \mu\text{m}$. Figure 1.7 shows both VWF shapes. The adhesion rate of VWF is increased in the stretched form as pointed out by [99].

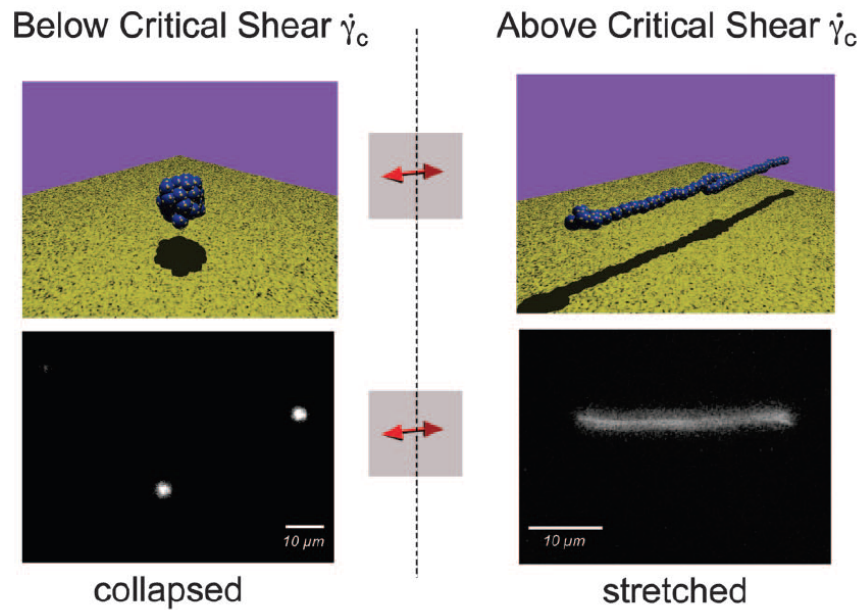


Fig. 1.7 VWF below and above the critical shear rate (upper part show a graphic representation and lower image is a fluorescence) these images are reproduced from [99]

1.2.5 Blood flow influence in thrombosis

Blood flow enhances the transport of coagulation factors and blood cells to the vessel wall injury or the artificial surface. The rate of transport (with diffusive and convective contributions) is extremely important for coagulation biochemistry. Looking closely to the characteristic kinetic, convective and diffusive time scales can be helpful to understand the role of each hemostatic element, as pointed out by Rana and Neeves [94]. In addition, platelet activation, aggregation and adhesion are largely influenced by the characteristics of the flow [54, 114, 48]. Large values of mechanical SS can increase the binding affinity between the different platelet agonists. In particular, a key event of the stress-induced activation and aggregation is the binding of VWF to platelet membrane glycoprotein Ib. Grabowski et al. [48] demonstrated that increasing shear rate may increase the flux of platelets to a foreign surface not only by diminishing the thickness of the platelet concentration boundary layer but also by simultaneously augmenting the platelet diffusion coefficient. A dependency of platelet adhesion to shear rate is therefore present. Furthermore, a clear interaction of platelet activation and mechanical shear has been observed at some SS threshold. Measurable changes in the platelet response are seen when the threshold of SS is reached. This threshold has a strong dependency on the exposure time as demonstrated in [54]. Figure 1.8 shows the dependency of the platelet serotonin release (a measure of platelet activation) to SS

magnitude and exposure time.

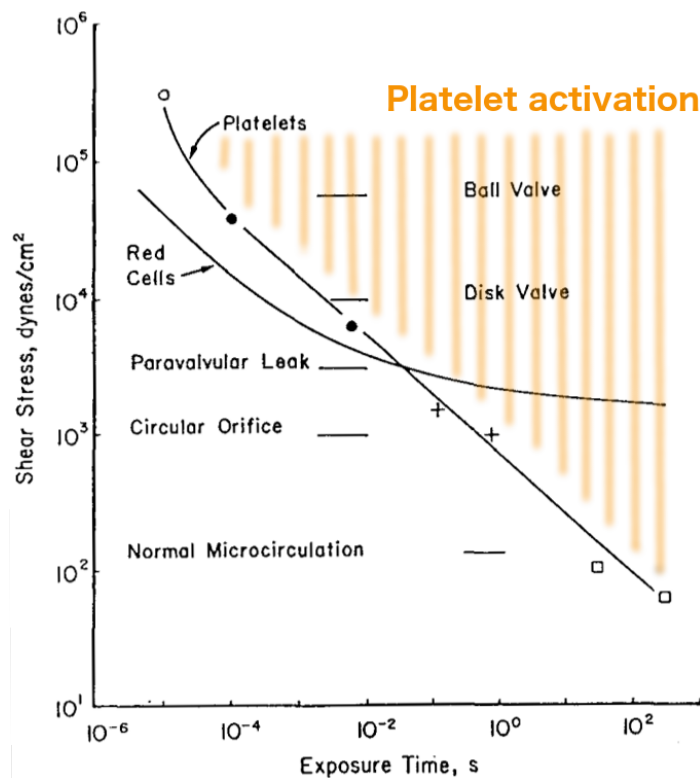


Fig. 1.8 Platelet activation in terms of shear-related serotonin release for platelets (red blood cells hemolysis also shown) as a function of exposure time, graph taken from [54]. Different shear conditions for different biomedical devices are shown.

Similar studies as the one about platelet activation have been done to evaluate the influence of the flow on leukocyte adhesion that leads to *TF* expression. However, these pathways are not fully understood. Another important element is turbulence that may influence species mixing and yield high mechanical shear stresses that can, in turn result in cell damage, such as, hemolysis or platelet activation. However, turbulence influence in thrombus growth is not fully understood. In addition, thrombus architecture is greatly influenced by how the fibrin plug and platelets adsorb and deposit to thrombogenic surfaces. Large wall shear stress (WSS) may provide a "washing" mechanism for the device surface. On the other hand, low wall shear stress regions combined with large residence times may promote thrombus growth [120, 125].

Virchows triad

Virchow's triad is frequently used as an evaluation tool for thrombosis risk. It consists of three risk elements that build a criterion for thrombosis [58]. Virchow's triad components are:

- Hemodynamic changes (Stasis or aberrant flow)
- Hypercoagulability of the blood
- Endothelial injury/dysfunction

The triad is a useful concept tool for clinicians and pathologists to understand the contributors to thrombosis. In a similar way, implanted medical devices can include equivalent criteria to evaluate thrombosis risks. De Biasi et al. [37] proposed a Virchow's triad for continuous-flow ventricular assist devices which considers the following aspects:

- Aberrant flow
- Anticoagulants therapy and donor variability
- Biomaterial surface reactivity

1.2.6 Inflammation and the complement system

The complement system enhances antibodies and phagocytic cells to kill bacteria. This activity was said to "complement" the antibacterial activity of the antibody, hence the name. It has fundamental clinical implications in the context of life-threatening tissue injury and inflammation. Complement system is structured by the classical and the alternative pathways (see Fig. 1.9). The classical pathway is triggered by antigen-antibody complexes while the alternative pathway is activated by contact activation of foreign surfaces such as fungal, bacterial polysaccharides, lipopolysaccharides, particles and **bio-material surfaces**.

The coagulation cascade is related to the complement system at several levels. Thrombin, coagulation factors XI_a , X_a , IX_a and plasmin were all found to effectively cleave C3 and C5 molecules which are central components of the complement system [47]. Furthermore, the contact system relates directly to the factors that initiate the complement system. In Table 1.2 all the interactions of the complement system with the coagulation systems are shown.

Gorbet and Sefton [47] pointed out the importance of complement system interaction with the coagulation process when artificial surfaces are present. An inflammatory response

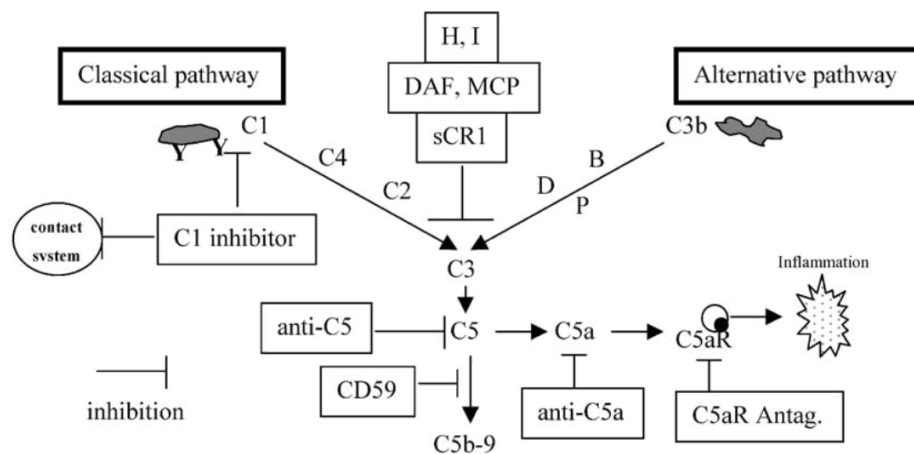


Fig. 1.9 Complement system diagram from [47] (Kirschfink M).

Protein	Type of interaction
Thrombin	Proteolysis of C3, C5, C6 and factor B
Factor XIIa	Proteolysis of C1r, C1s and C3
Kallikrein	Proteolysis of C1, C5 and Factor B
Antithrombin III	Protect RBC form lysis by mC5b-9
Bb	Proteolysis of prothrombin
C3bBb	Proteolysis of prothrombin
C1 inhibitor	Inactivates FXIIa and kallikrein
S protein (vitronectin)	Stabilizes plasminogen activator inhibitor 1
C4b-binding protein	Binds to the vitamin K-dependant protein S

Table 1.2 Interactions between complement and coagulation systems [47]

is observed in the presence of bio-materials. This inflammation is primarily regulated by activation of the alternative pathway. In addition, the increased activity of the complement system boosts leukocyte *TF* expression and therefore thrombin production.

Other thrombosis elements

Leukocytes Several types of leukocytes are present in blood. Neutrophils, monocytes, lymphocytes, basophils and eosinophils are the main five types of leukocytes that form the immune system. Artificial surfaces interaction with Neutrophils (40 – 60% of leukocytes population) and monocytes (5% of leukocyte population) may activate these cells. One of the most important effects of leukocyte activation for thrombosis is the expression and synthesis of *TF*. Leukocyte adhesion may also participate in inflammation, therefore promoting a feedback loop with the contact system.

Red blood cells Red blood cells (RBC) play an important role in hemostasis due to its impact on flow conditions, which has effects on the interactions between platelets and the surface vessel. For instance, RBC tend to move to the center of blood vessels causing platelet margination towards the vessel surface [66]. This effect enhances the platelet adhesion at the injury site or at the device surface. In some cases, thrombosis takes place in regimes in which mass transport is dominated by diffusion. In this context, RBC enhanced the diffusivity of platelets. An expression to estimate the enhanced Brownian diffusion coefficient in plasma was proposed by Antonini et al. [10].

In regions of blood stasis and low shear stress zones in which the coagulation cascade takes place producing high amounts of fibrin nets that trap RBC or stacked cells (RBC rouleaux) forming the so-called erythrocyte rich thrombus (red thrombus) as explained by Cadroy and Hanson [24]. Red thrombi are thus that form in slow flow regimes while white thrombi are predominantly form by platelets in high shear flows. In addition, RBC membrane provide another surface of phospholipids in which coagulation reactions can take place. For further information about the effects of RBC in coagulation the reader is referred to [71].

1.3 Mathematical modeling: state of the art

Thrombosis modeling is a challenging task due to the multi-scale and multi-physics nature of this biological process. Ranging in time and space from [(coagulation reactions) ≤ 1 s, 1000 s (stable thrombus)] and [$0.1 \mu\text{m}$ (protein interactions), $100 \mu\text{m}$ (transport effects)] respectively as pointed by Xu et al. [123] and displayed in Fig. 1.10. In addition, the impact of the growing thrombus on the flow and the intertwined dynamics of different biological processes renders thrombosis modeling extremely challenging. In this section, a discussion about the existing mathematical models is presented, highlighting the different modeling issues.

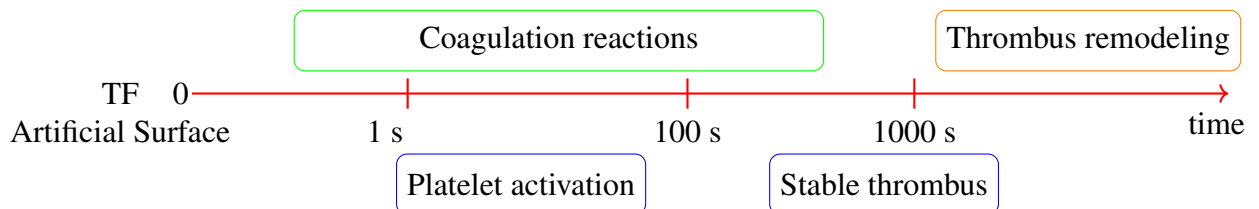


Fig. 1.10 Time line of thrombus formation and the main biological events that lead to a stable thrombus.

1.3.1 Thrombus modeling in vivo

Most of the mathematical models have been developed for in-vivo situations in which an injury site initiates clot formation. The complexity of the models increases with the level of details of the biological process description. For instance, a simple description may include only the coagulation reactions in quiescent platelet-poor plasma samples. An extra level of complexity could be added by considering platelet-limited binding reactions or fluid-structure interaction of the growing thrombus with the flow ([43, 38, 5]). In this literature review, the levels of complexity of the thrombus models and their applications are discussed for both in vivo situations and for medical devices. In addition, model reduction towards applications pipelines for both cases is reviewed.

Models for quiescent plasma, a global assessment of coagulation

In clinical practice, the global production of thrombin is evaluated in a quiescent blood plasma. From a modeling perspective, this process is homogeneous in space and thus the time evolution of coagulation factors can be described by a system of ordinary differential equations (ODE):

$$\frac{dC_i}{dt} = R_i \quad (1.1)$$

where C_i are the biochemical species (coagulation factors) and R_i are the source terms of each species, that are computed according kinetic schemes that describe the coagulation cascade. One of the first models that used this strategy to predict thrombin generation was presented by Jones and Mann [62]. This model considers the TF pathway (extrinsic pathway) including 18 species and 20 differential equations that describe the coagulation reactions initiated by TF . In this model, the system is solved using a Runge-Kutta integration technique. Figure 1.11 shows the numerical and experimental results using this type of approach. Good agreement is observed in the thrombin generation curves. Models considering more complex systems have been developed to capture thrombin production in the case of plasma with coagulation factors deficiencies [57, 130, 90]. A kinetic model considering the intrinsic pathway was developed by Zarnitsina et al. [129] considering the polymerization of fibrinogen. In addition, the Tenase and Prothrombinase complex are dependent on the calcium concentration, which contrasts with previous models in which calcium and phospholipids were assumed to be present in excess.

It should be noted that not all the interactions taking place in the coagulation cascade have been completely understood. In addition, the mechanistic pathways are being revisited,

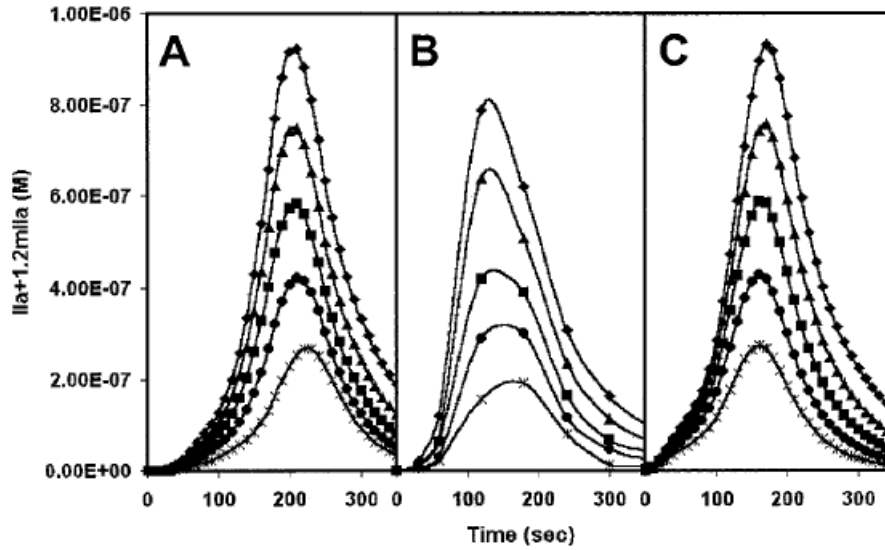


Fig. 1.11 Active thrombin as a function of time presented in [57] for numerical (A) and experimental results (B). The curves correspond to a range of prothrombin concentrations [$0.7 \mu\text{M} \sim 2.1 \mu\text{M}$]. Numerical results of (C) are obtained for small variations of factor V_a showing little influence on the results.

for instance, the role of the contact activation system in thrombosis [15, 85]. Also, large uncertainty in the reactions rates that are involved in the models [36] may hinder the predictive capabilities of the kinetic models. Due to these reasons the clinical application of these models remains controversial [56]. In contrast, for research purposes this type of modeling is of great value in the understanding of the coagulation dynamics and to investigate the unknown mechanistic pathways of coagulation [73].

Modeling of thrombotic elements using an analytic flow approximation

Coagulation reactions take place in the blood flow, thus the influence of convection and diffusion in thrombosis is of great importance. In order to model this process, the vast majority of models have used the convection-diffusion-reaction equations:

$$\frac{\partial C_i}{\partial t} + \nabla \cdot (C_i \mathbf{u}) = \nabla \cdot (D_i \nabla C_i) + R_i \quad (1.2)$$

where C_i and D_i are the molar concentration and diffusion coefficients for each species i , R_i is the reaction source term and \mathbf{u} stands for the velocity field. Eq. 1.2 is applied for each of the biochemical species (coagulation factors, platelets, etc). Basmadjian [13] introduced the effects of blood flow by solving a set of partial differential equations describing the chemical

species concentration in space and time. This model considered a single reactive event at the vessel wall and a lumped mass transfer coefficient that can be obtained from experiments or rigorously derived from analytic concentration profiles. Fig. 1.12 shows the L ev eque analogy which is an idealized situation that allows to derive heat or mass distribution in Hagen-Poiseuille flow which can be used to consider mass transport in a reactive system.

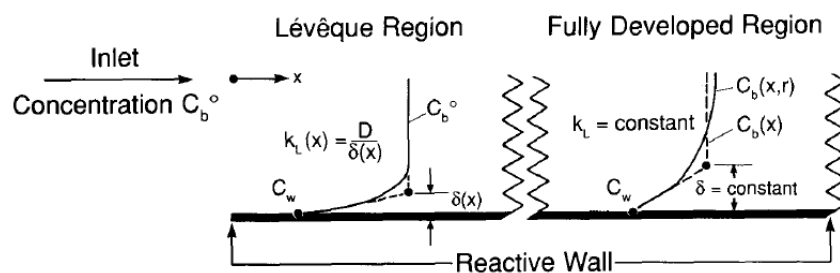


Fig. 1.12 Two transport zones as showed in [13]

Considering an analytic expression for mass transport allows a quick evaluation of generalized cases with specific transport and reaction rates. In a similar model, Kuharsky and Fogelson [67] considered flow transport and a more complex biochemical description. The model studies platelet activity and coagulation events occurring in a thin layer, called the reaction zone, just above a small vascular injury. Plasma-phase, subendothelial-bound and platelet-bound enzymes and zymogens as well as activated and non-activated platelets are taken into account. All species in the reaction zone are assumed to be well mixed: each species is characterized by its concentration that is tracked in time using an ordinary differential equation. Advective and diffusive transport of fluid-phase species (coagulation factors and platelets) inside or outside of the reaction zone is modeled by a mass-transfer coefficient computed in a similar way as in [13].

Modeling of thrombus in simple flow configurations

Fogelson and Guy [41] presented a model to predict platelet thrombi formation in a simple configuration representative of coronary-artery sized blood vessels. Their approach accounted for platelet adhesion and aggregation in an injured vessel using distributions of elastic links. This method focused in platelet-platelet and platelet-subendothelium interactions considering the flow as a continuum, thus a closure approximation is proposed to capture the essential information from the microscale without computing interaction events explicitly. Their

results showed that a growing thrombus can modify its subsequent growth through small scale changes or structural breakup based on the shear-stress exerted by the fluid. A sequence of a growing thrombus in a stenosed channel is shown in Fig. 1.13.

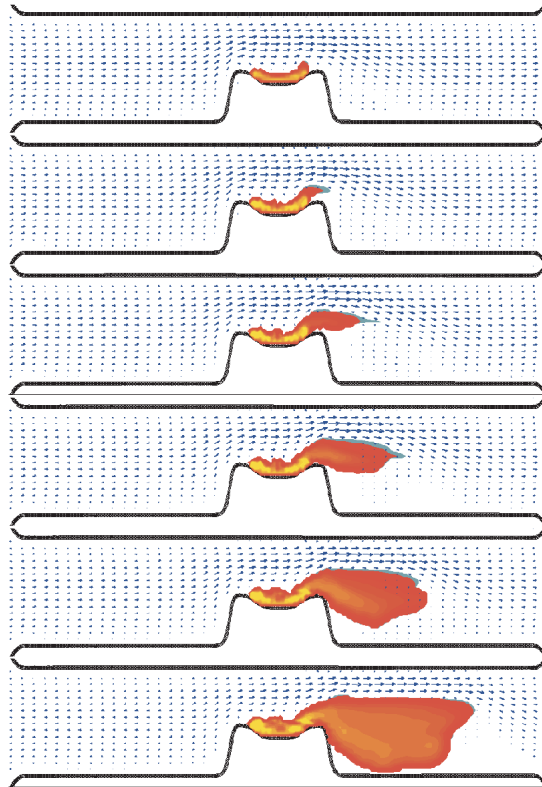


Fig. 1.13 Thrombus growth sequence in a blood vessel from [41]. The red and yellow color field show the platelets aggregation intensity field.

Anand et al. [6–8] developed a model to quantify thrombus formation and dissolution in a simple cylindrical pipe for various steady and pulsatile flow conditions considering visco-elastic properties of blood. The model included biochemical reactions until the formation of fibrin and platelet activity. An interesting feature of this work is that platelet activity promotes the coagulation reactions by increasing the reaction rate of certain reactions. In addition, a critical threshold of fibrin is proposed to define the clot. Anand and co-workers treated the clot as a highly viscous fluid to mimic momentum reduction. Thrombus dissolution was modeled as a function of shear rate and local fibrin concentration. The model of Anand et al. [6] was used in a simplified way by Bodnár and Sequeira [21] to study the clot formation and growth of thrombus in the vicinity of an injured vessel wall with fair predictive capabilities. Leiderman and Fogelson [70] presented a model that extended the work of Kuharsky and

Fogelson [67] and explicitly modeled thrombus growth and its influence on the local fluid dynamics; as a note, the platelet interactions are modeled as in [41]. This was the first work that incorporated the interaction of platelet aggregation with a detailed description of the coagulation cascade. Their results showed that the production of thrombin has a dependence on TF local concentrations and wall shear rate. Figure 1.14 shows the two-dimensional development of a thrombus in a blood vessel due to an injury.

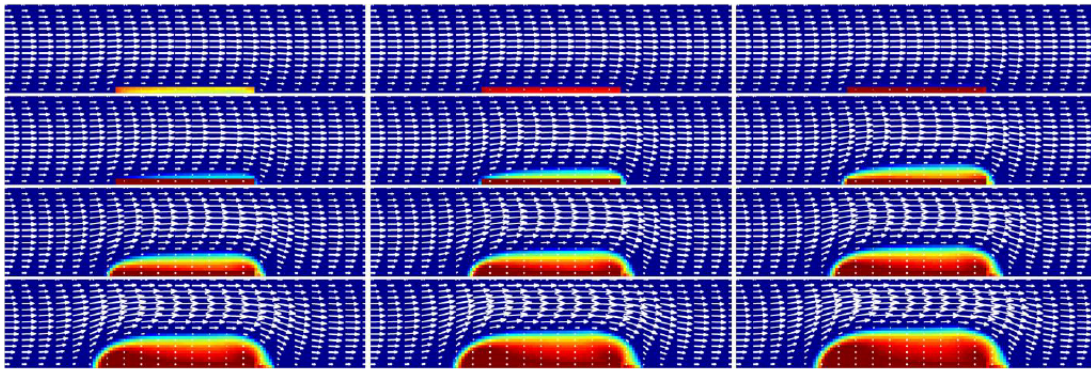


Fig. 1.14 Thrombus development from [70] at different instants starting until $t = 600$ s using a TF concentration of 15 fmol cm^{-2} .

In the work of Xu et al. [123], a two-dimensional model is presented where a macroscopic view of the flow is modeled by the Navier-Stokes equations. Microscale interactions between platelets and coagulation reactions are modeled using an extended stochastic discrete model. Pivkin et al. [93] developed a model for thrombus growth based on platelet aggregation. In this model, the flow is considered as a continuum and described by the Navier-Stokes equation, while platelets are explicitly tracked and their interactions are modeled through specific force terms that consider platelet-platelet and platelet-wall interactions. Their results showed that thrombus formation depends on blood velocity which correlated well with experimental data. In a similar approach, Yazdani et al. [126] developed a model coupling a spectral/hp element method to compute the flow with a particle-force method. On one hand, the spectral method is used to solve the flow field and the coagulation factors transport on a Eulerian grid and on the other hand, two-way interactions are considered between the flow and the Lagrangian platelets description. The coagulation cascade model of [6] was used and platelet activation due to thrombin was considered. The model was applied to a stenosed situation and a venous flow configuration. Their numerical results align well with experimental data of thrombus formation as shown in Fig. 1.15.

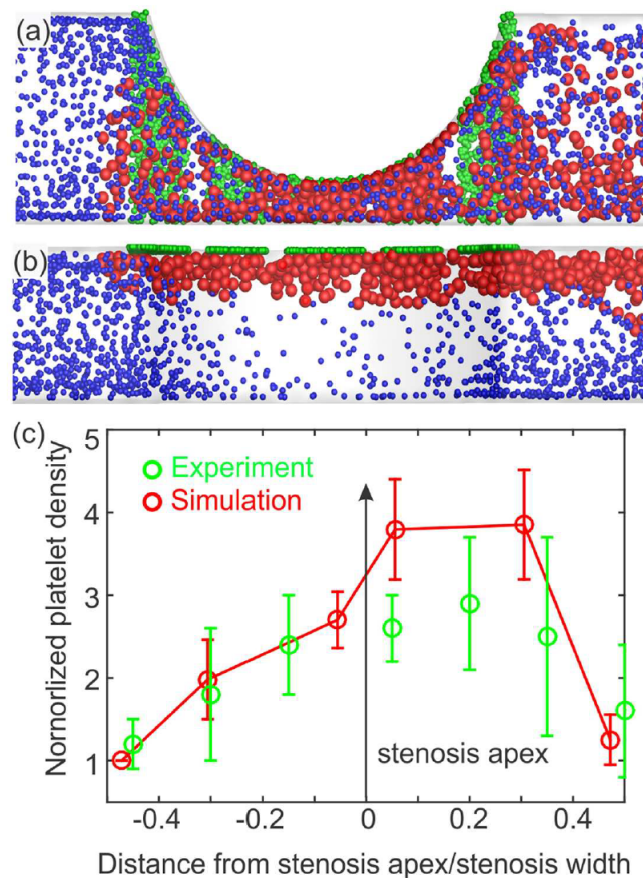


Fig. 1.15 Platelet aggregation at high shear rates in an stenosed channel, a) view normal to the flow b) above view, c) experimental and numerical results with uncertainties for normalized platelet density. The image is taken from [126]

Thrombosis models application on complex flow configurations

The previous models were used, in general, in simple flow configurations. In contrast, other authors have investigated thrombosis in more complex flow configurations. For instance, Biasetti et al. [17] studied the unsteady blood flow in aortic aneurysms using both a Newtonian and a non-Newtonian description of blood. A possible relation between vortex and intraluminal thrombus (ILT) formation was investigated. In a following work, Biasetti et al. [18] introduced a model in which biochemical reactions were added with a set of convection-diffusion-reaction equations from [62]. The results showed a big influence of the flow (shear rates and vortex) on the production of thrombin in the zones of ILT formation as shown in Fig. 1.16. A similar approach was used by Seo et al. [101] to study infarcted left ventricles. In this work, a correlation coefficient is calculated to quantify the spatial correlation between the hemodynamic and coagulation metrics, showing a moderate correlation.

Model reduction in in-vivo thrombus formation

The approaches used in the study of complex flow configurations, while interesting, remain computational intensive for clinical intervention-planning frameworks. Ngoepe et al. [87] pointed out that reducing the modeling complexity and considering minimal and sufficient biological details is important for interventional planning. In this context, a reduced model for near wall transport was presented by Hansen and Shadden [52]. This model focused on the micron-thick reaction layers present in aortic aneurysms. In this approach, an analogy to the boundary layer theory is used to obtain a surface equation for reaction-rate-limited and transport-limited applications. The general idea of this method is that in near wall regions, the transport problem can be considered as quasi steady and thus, analytic approximations of the flow field can be used to compute the concentrations of coagulation factors solving a surface equation derived from the flow approximation in near wall regions. The model of Hansen and Shadden was then applied to an abdominal aortic aneurysm geometry taken from [18] using a reduced model of thrombin formation [91]. The results aligned well for both regimes (reaction-rate and transport limited) outside of the entry regions and flow reattachment points with lower computational cost. Ngoepe and Ventikos [88] presented a model for clot development in patient specific cerebral aneurysm using a reduced model of the coagulation cascade proposed by Wagenvoort et al. [116]. The model uses a level-set method to track the clot phase (using the fibrin concentration as a threshold criteria), in this phase a mechanical effect of the growing clot is considered through a porous medium model. Their results showed that with further development, this type of approach, may be used for clinical intervention planning. In a similar approach, Menichini and Xu [80] developed a model based on local shear rates, residence time and platelet distribution. Shear rate was used to compute cell adhesion and thus identify regions prone to clot formation. Residence time is considered to bypass the complicated biochemical descriptions of the coagulation cascade. Populations of non-activated, activated and bounded platelets are considered. Menichini and Xu accounted for thrombus growth through a Brinkman term that depends on bounded platelets. The model of [80] was applied in patient-specific aortic dissections to study thrombus growth in the false lumen that is formed in this pathology [78, 79]. This strategy showed good predictive qualities at a reduced computational cost. Some of the limitations discussed by Menichini and Xu are related to modeling assumptions such as, geometry simplifications, rigid walls, kinetic rates adaptation to achieve non-physiological rapid thrombus formation. The model of Yazdani et al. [126] was further applied to study intraluminal thrombus formed in aortic dissections in [125]. In this case, a final value problem is studied with a data driven approach to understand the thrombus formation dynamics.

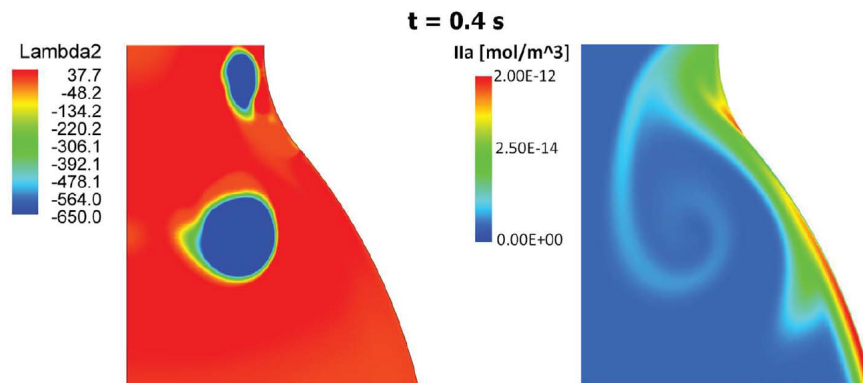


Fig. 1.16 Vortex educed using λ_2 criteria carrying thrombin in a characteristic counter-clockwise trail taken from [18]

Model reduction in platelet activity

Model reduction efforts have also included platelet activity; Shadden and Hendabadi [102] developed a platelet activation potential derived by integrating the strain rate over a Lagrangian trajectory. They applied their model to a stenosed channel showing a potential relation between the kinematics and the chemical dynamics of platelet activation. Achille et al. [1] formulated a predictor of intraluminal thrombus formation in abdominal aortic aneurysms (AAA) using a chemistry-free approach. The model was based on flow criteria (such as time average wall shear stress, oscillatory shear index) and on the platelet activation potential of [102]. Achille et al. [1] applied the risk criterion to 10 carotid arteries and 6 abdominal aortic aneurysms for healthy and pathological cases. The results showed that the predictor aligns well to in vivo results. However, more studies should be done to study nascent thrombus that were not considered in the study and that are crucial for medical practice. This type of approach can allow a quick evaluation of regions prone to thrombosis as shown in Fig. 1.17. The work in [102] was extended by Hansen et al. [51] who compared a Lagrangian, Eulerian and a power law descriptions of platelet activation potentials. The Eulerian approach was modeled as a continuum quantity using the convection-diffusion equation combined with a local platelet activation rate which is a function of the scalar stress. The power law model was taken from [107], which was derived experimentally and applied in an Eulerian framework. The three different models were applied to predict thrombus formation in abdominal aortic aneurysms. In terms of model comparison, the Lagrangian approach was twice longer to converge and showed similar activation levels as the Eulerian approaches. In terms of thrombus formation prediction, their results showed that for AAA geometries, mechanical activation of platelets does not play a significant role in thrombus for-

mation and suggests that other biochemical agonist of platelet activation should be considered.

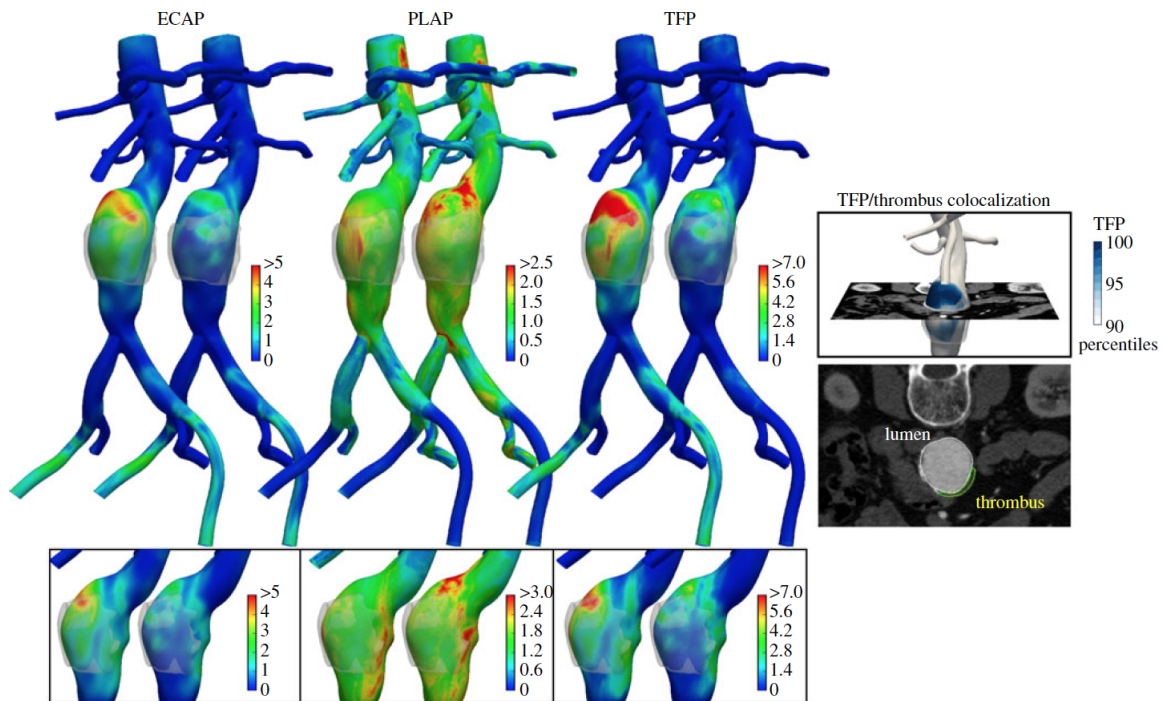


Fig. 1.17 Spatial distributions of three flow-based criteria for thrombosis risk. Endothelial cell activation potential (ECAP), platelet activation potential (PLAP), thrombus formation potential (TFP). The image was taken from [1].

1.3.2 Thrombus modeling in medical devices

A substantial number of models dedicated to device-related thrombosis have focused on platelet activity. Sorensen et al. [109] developed a model for platelet deposition and activation considering platelet-platelet and platelet-surface adhesion. Activation of platelets due to chemical agonist and platelet generation of thrombin along with a coagulation inhibitor and heparin were considered. In this approach, the velocity fields were modeled using the Hagen–Poiseuille analytical solution in a similar manner as [13]. The model was applied to a parallel-plate flow to observe the deposition of platelets into collagen. The deposition predicted aligns well with experimental results. Goodman et al. [46] present a model in which thrombus growth is handled by increasing the viscosity in mesh cells where the volume of adherent platelets was greater than the volume of the grid. The approach also considers platelet adhesion and platelet activation in a similar way as [109]. An interesting feature of the model is embolization, which was tracked through the fluid forces on the growing

thrombi that removed the thrombi from the wall when the shear force was greater than an arbitrarily embolization threshold. Finally, the model of Goodman et al. [46] is compared with experimental results showing good agreement for thrombus growth in a tubing with different diameter segments. Wu et al. [120] developed a model of thrombus deposition based on platelet activity considering the platelet activation pathways of Sorensen et al. [109] using a continuum representation of platelets inspired by the work of Fogelson [40]. Platelet activation due to chemical agonist and mechanical shear is considered, in addition, platelet deposition is modeled. Two platelet populations are considered: resting platelets and activated platelets. Thrombus growth is considered through the volume fraction of deposited platelets. In general terms the features of the model allow to study: thrombus-fluid interaction, thrombus inhibition, stabilization, dissolution and erosion. The model of [120] was applied to a continuous flow ventricular assist device (VAD) configuration in [121]. Their results accurately predict the regions of thrombus formation as shown in Fig. 1.18. In addition, their simulations suggest that thrombus accumulation can increase with lower flow rates and showed that it can be suppressed by anticoagulants or by improving the adhesive properties of the surface.

Reduced models dedicated to medical devices

Model reduction has also been useful in device-related thrombosis. The general goal of these models is to reduce the computational cost of detailed models in order to apply them to complex flow configurations. A damage model for platelets was developed from an unsteady simulation by Alemu and Bluestein [3]. In this approach, total stress and exposure time are combined to obtain a damage model expression along pertinent trajectories (hot spots of activation related to recirculation zones, strong jets and spiral vortices are included in the trajectories studied). The model was applied to a mechanical heart valve. The predicted levels of platelet activation aligned well with experimental results. Soares et al. [107] extended the work of Alemu and Bluestein [3] in a mathematical model of platelet activation due to stress histories. This model addressed the limitations of the power law model to account for load rate dependence and high stress conditions while retaining the good properties of the power law model at low stress. The model parameters were determined with experimental data from a hemodynamic shearing device. The model results showed good agreement with a variety of shear stress conditions which can be used in CFD simulations to reproduce platelet activation. Taylor et al. [112] developed a simplified model for thrombus growth following the work of Fogelson and Guy [41]. In this approach, mechanical activation of platelets is computed using a power law expression as in Soares et al. [107]. Chemical

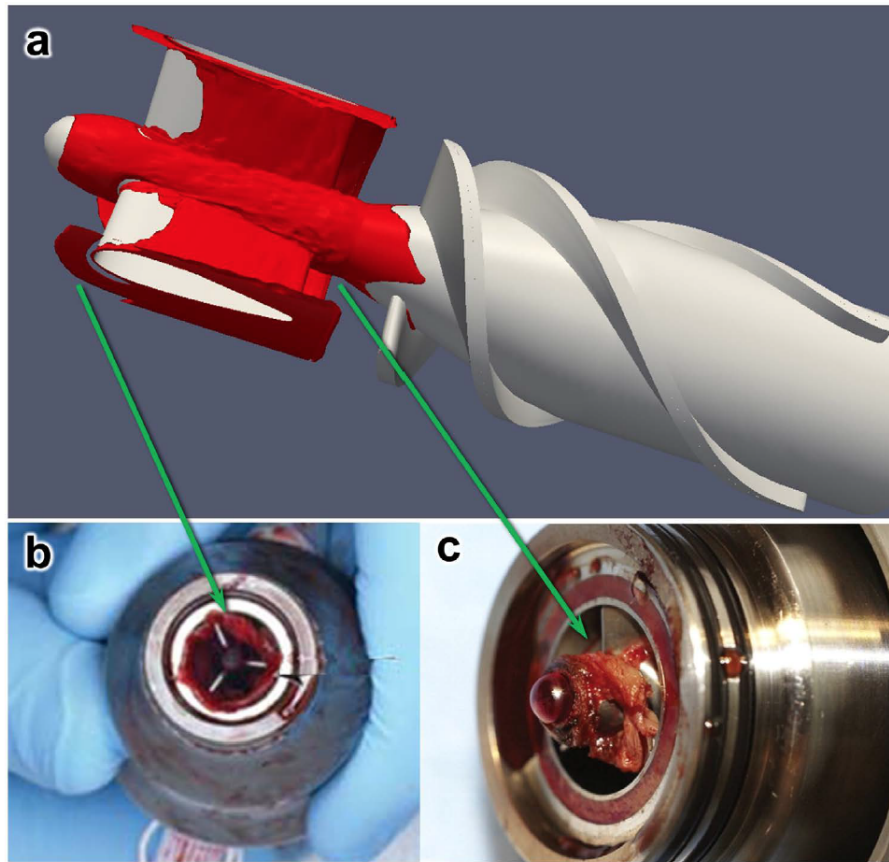


Fig. 1.18 a) Numerical simulation of thrombus formation based on platelet activity b) and c) are clinical images. The results show significant deposition upstream of the inlet straightener vane (zone of low WSS not shown). The image is taken from [121].

activation by ADP is calculated as in Sorensen et al. [109]. A platelet aggregation intensity is proposed as a metric for thrombus growth. This metric depends on empirical derived parameters of wall shear stress and scalar stress that regulate thrombus deposition and erosion. A modified Brinkman term was added to the momentum equations thus acting as a sink in thrombus regions in which high concentration of platelet-platelet links are present. This model was able to predict the growth of a thrombus in backward facing step configuration at a Reynolds number of $Re = 430$; the evolution of the growing thrombus is showed in Fig.1.19.

Modeling of the coagulation cascade in medical devices

As previously mentioned, thrombus formation depends on the intertwined process of platelet activity and coagulation reactions. However, only a small amount of models have been

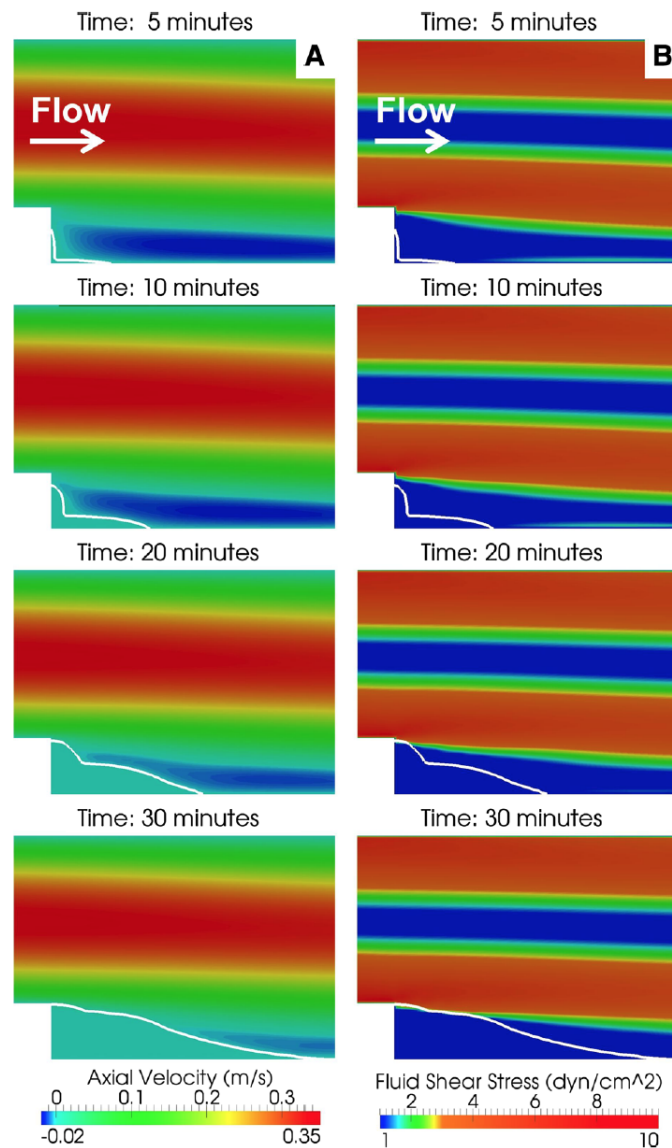


Fig. 1.19 Growing thrombus at a backward facing configuration. a) axial velocity b) shear stress. The platelet clot is represented by a white contour plot computed with an aggregation intensity threshold. The image is taken from [112].

dedicated to assess the formation of thrombin due to coagulation reactions triggered by the artificial surface. A specific model of the intrinsic and common pathways was presented by Gregory and Basmadjian [49]. The model comprised 20 dominant reactions with 11 components that were reduced to 4 coupled ODEs using Leveque's boundary approximation. A polynomial algebraic equation was obtained and 3 steady state concentrations for coagulants were obtained. In this model, the coagulation cascade is initiated by the activation of factor XII which was considered in 3 states (activated, bound to the surface and fragmented). A

mathematical model for the contact activation of factor XII by a pro-coagulant surface was developed by Guo et al. [50]. The model of Guo and colleges uses a Michaelis-Menten kinetic mechanism simplifying the coagulation cascade of enzymatic reactions in a single enzymatic reaction. The hypothesis of an homogeneous medium is used, only time evolution is studied. The model was studied in two steps; first, the activation of factor XII_a as a function of a catalytic surface potential (that variates according to the surfaces water-wettability properties) was computed. Then, factor XII_a interacts with the rest of the cascade of reactions in the form of a substrate. These two steps are combined to predict the coagulation time. Guo et al. [50] concluded that the material induced coagulation is a surface mediated event thus the coagulation time depends strongly on the surface area and on the properties of the surface. Finally their results suggest that procoagulant surfaces have no influence in enzymatic reactions other than factor XII activation. A detailed kinetic model of the coagulation cascade including the contact system was developed by [30]. This description was used to compute thrombin formation in resting human blood without adding TF . In a similar approach, [130] developed a model including both tissue factor related reactions and the contact activation system to compute thrombin formation in normal and deficient conditions. Before these models appeared none of the kinetic descriptions was able to predict thrombin formation without adding TF . It is important to mention that some other models include the intrinsic pathway ([129, 7]). However, the initiation mechanism used by these models is TF exposure, and thus, a straightforward application of this approaches is not possible for device-related thrombosis.

Model	Features				
	Biochemistry	Hemodynamics	Platelets	Clot growth	Contact system
Jones and Mann [62]	x				
Zarnitsina et al. [129]	x				
Hockin et al. [57]	x				
Zhu [130]	x				x
Chatterjee et al. [30]	x		x		x
Wagenvoort et al. [116]	x				
Papadopoulos et al. [91]	x		x		
Xu et al. [123]	x	x	x	x	x
Basmadjian [13]	x	x			
Anand et al. [7]	x	x	x	x	
Leiderman and Fogelson [70]	x	x	x	x	
Sorensen et al. [109]	x	x	x		
Yazdani et al. [126]	x	x	x	x	
Menichini and Xu [80]		x	x	x	
Ngoepe and Ventikos [88]	x	x		x	
Taylor et al. [112]		x	x	x	
Wu et al. [120]		x	x	x	
Biasetti et al. [17]	x	x			
Seo et al. [101]	x	x			
Achille et al. [1]		x			

Table 1.3 Summary of the existing models highlighting their general features.

Conclusion

Mathematical models have addressed a wide range of biological situations with fair predictive results. However, important biological aspects such as the contact activation system or the complement system have been neglected. Furthermore, in device-thrombosis a gold-standard model with the proper compromise between the biological description and computational cost has not been found yet.

1.4 Flow solver YALES2BIO

An in-house CFD software YALES2BIO (<http://www.math.univ-montp2.fr/~yales2bio/>) is used in this thesis to compute the blood flow and implement the coagulation reactions. A general presentation of the solver is given in this section. YALES2BIO is based on YALES2, which is an unstructured solver developed at CORIA, Rouen, France. YALES2 is dedicated to massively parallel computations of two-phase combustion problems [83, 84]. YALES2BIO is devoted to blood flow simulations and inherits the YALES2 parallel capabilities and high-order finite-volume schemes for complex geometries. Both macroscopic [32, 104, 131] and microscopic [68, 105, 76] configurations have been studied using YALES2BIO. Figure 1.20 shows two examples of macroscopic applications; in one case the flow inside a left ventricle is computed [34] and in the second case the flow in an artificial heart valve is considered [106].

Numerical Method

The numerical solution of the incompressible Navier-Stokes (NS) as implemented in YALES2BIO are explained in the following. The Newtonian fluid description is used in this work to focus on the biochemical aspects of thrombus formation (which are already complex). It should be noted however, that accounting for the shear thinning behavior of blood can impact quantities that are relevant to thrombotic events such as the wall shear stress or the rate of transport of the chemical species towards the thrombus. [7, 6]. Considering a Newtonian fluid, the mass conservation equation and the NS equations read:

$$\nabla \cdot \mathbf{u} = 0, \quad (1.3)$$

$$\frac{\partial \mathbf{u}}{\partial t} + \mathbf{u} \cdot \nabla \mathbf{u} = -\frac{\nabla p}{\rho} + \nu \nabla^2 \mathbf{u} + \frac{\mathbf{f}}{\rho}, \quad (1.4)$$

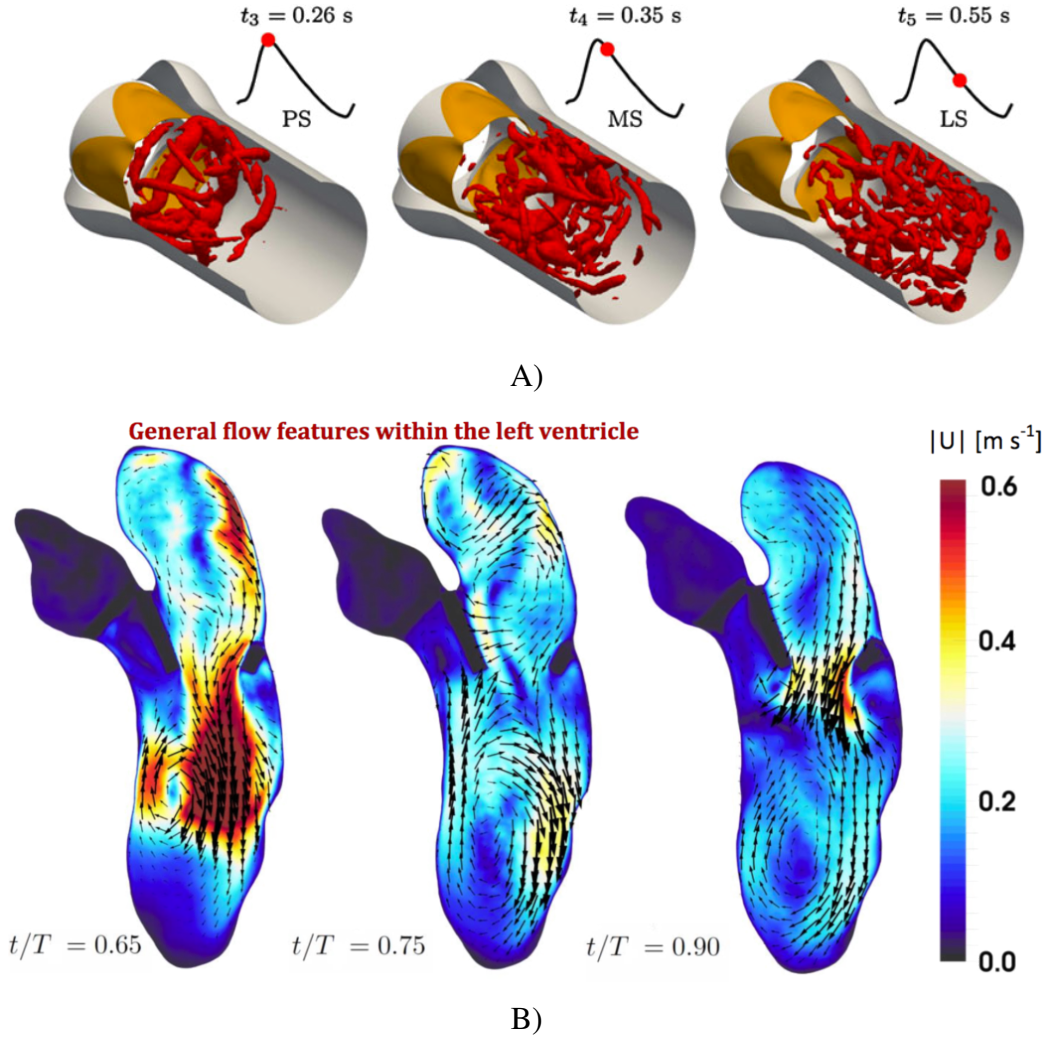


Fig. 1.20 Macroscopic examples of blood flows in A) Mechanical artificial heart valve computation without thrombosis from [106] (Iso-surfaces of the instantaneous Q criterion is shown). B) Velocity field inside a patient-specific left ventricle from [34].

where \mathbf{u} is the velocity vector, p is the pressure field, ρ stands for the density, \mathbf{f} is a force per unit of mass and ν is the kinematic viscosity.

The projection method of Chorin [35] is used to solve Eq. 1.3 and Eq. 1.4. Let us write the semi-discrete form of Eq.1.3 and Eq 1.4 in time using a Euler explicit scheme:

$$\nabla \cdot \mathbf{u}^{n+1} = 0, \quad (1.5)$$

$$\frac{\mathbf{u}^{n+1} - \mathbf{u}^n}{\Delta t} + \mathbf{u}^n \cdot \nabla \mathbf{u}^n = -\frac{\nabla p^{n+1}}{\rho} + \nu \nabla^2 \mathbf{u}^n + \frac{\mathbf{f}^n}{\rho}, \quad (1.6)$$

where ϕ^n is the value of a quantity ϕ at the beginning of the time step and ϕ^{n+1} is the value of ϕ at the end of the time step. A direct computation of \mathbf{u}^{n+1} is not possible since the pressure p^{n+1} is unknown. To overcome this, a splitting algorithm is used that yields to a prediction step of a velocity \mathbf{u}^* using the previous time step p^n as follows:

$$\frac{\mathbf{u}^* - \mathbf{u}^n}{\Delta t} + \mathbf{u}^n \cdot \nabla \mathbf{u}^n = -\frac{\nabla p^n}{\rho} + \nu \nabla^2 \mathbf{u}^n + \frac{\mathbf{f}^n}{\rho}, \quad (1.7)$$

Predicted velocity \mathbf{u}^* is subtracted to \mathbf{u}^{n+1} leading to:

$$\mathbf{u}^{n+1} - \mathbf{u}^* = -\Delta t \frac{\nabla(p^{n+1} - p^n)}{\rho} \quad (1.8)$$

At this step the predicted velocity \mathbf{u}^* is not divergence free, thus a correction step is performed. This is done by taking the divergence of Eq. 1.8 and applying the mass conservation constraint ($\nabla \cdot \mathbf{u}^{n+1} = 0$) leads to:

$$\frac{\Delta(p^{n+1} - p^n)}{\rho} = \frac{\nabla \cdot \mathbf{u}^*}{\Delta t} \quad (1.9)$$

The pressure increment ($p^{n+1} - p^n$) is computed using an iterative solver of the type conjugate gradient. In YALES2BIO several variants of this type of solver are available. In this thesis the Deflated Preconditioned Conjugate Gradient (DPCG) algorithm [72, 74] was used in most computations. Finally the predicted velocity \mathbf{u}^* is corrected by the the calculated pressure p^{n+1} using the following equation:

$$\mathbf{u}^{n+1} = \mathbf{u}^* - \Delta t \frac{\nabla(p^{n+1} - p^n)}{\rho} \quad (1.10)$$

Time and spatial integration schemes

A 4th-order Runge-Kutta scheme in time [118] is used to compute \mathbf{u}^* . The finite-volume method (FVM) of 4th-order is used for spatial discretization.

1.5 Objectives of the thesis and chapter contents

The main objectives of the thesis are the following:

- **Couple an existing detailed kinetic model of the coagulation cascade with a CFD solver to assess thrombin production in realistic flow configurations**

- **Improve our understanding of the detailed kinetic model using a global method of sensitivity analysis**
- **Reduce the complexity of the detailed kinetic model to improve the computational efficiency in complex flow applications**
- **Couple the coagulation cascade with an existing platelet-based model of thrombus formation dedicated to medical devices**

After this introductory Chapter 1 the thesis is organized as follows:

Chapter 2. In this chapter a numerical framework for the initiation of coagulation due to the contact activation of blood with an artificial surface is presented. The contact activation system was modeled through a reactive surface boundary condition. The kinetic model of the coagulation cascade of Chatterjee et al. [30] is applied to a backward facing step configuration. The objective of this chapter is to properly model the initiation of the coagulation cascade at a surface and provide insights about the production of thrombin due to artificial surfaces. This work was published in *Biomechanics and Modeling in Mechanobiology*. The article is entitled "Introducing the pro-coagulant contact system in the numerical assessment of device-related thrombosis" [77].

Chapter 3 explores the sensitivity of the results to the reaction rates in the model of Chatterjee et al. [30] using a global sensitivity method. From the sensitivity analysis, a reduced set of biochemical reactions is proposed to model thrombin production due to contact activated reactions. The parameters involved in the kinetic reduced model were inferred using the Bayesian statistical framework. The aim of this chapter is to identify the most important kinetic parameters of the model of [30] and propose a reduced scheme of reactions that includes contact activation. The reduced model could help to include the coagulation reactions in CFD computations of device-related thrombosis in a computationally efficient manner.

Chapter 4. The platelet-based model of Taylor et al. [111] for thrombus formation was implemented in YALES2BIO. The global objective of this chapter is to include platelet activation by thrombin in the model of Taylor et al. [111]. This is done by including the reduced model developed in Chapter 3 through the boundary condition explained in Chapter 2.

Chapter 5. In this concluding chapter the main results are summarized and some perspectives on device-related thrombosis modeling are discussed.

Chapter 2

The contact system in device-related thrombosis modeling

This chapter corresponds to an article entitled "Introducing the pro-coagulant contact system in the numerical assessment of device-related thrombosis" (Méndez Rojano et al. [77]) that was published in *Biomechanics and Modeling in Mechanobiology*. In Section 2.1 a brief introduction on thrombosis modeling related to blood coated medical devices is presented. Then, a novel numerical framework that allows to properly trigger coagulation reactions at the surface of a medical-device is developed. Finally, an academic application in a backward facing step configuration is studied using the reactive surface boundary condition to start coagulation.

2.1 Introduction

The use of blood-coated devices is a common medical practice to treat several cardiovascular conditions. However, the poor thrombotic performance of some types of medical devices remains an issue in clinical practice (Chan et al. [28], Mehra et al. [75], Hastings et al. [53]). For instance, thrombus formation may lead to device malfunction, thrombo-embolism or increased risk of a hemorrhagic stroke due to the anti-coagulant therapy. Thrombosis is a complex phenomenon that involves several processes such as coagulation reactions, platelet activation/aggregation, blood flow dynamics, among others. Furthermore, these mechanisms interact with each other at different time and spatial scales as explained in Furie and Furie [44]. When it comes to device-related thrombosis, the artificial wall of the device interacts with the thrombotic processes as pointed out by Gorbet and Sefton [47]. Wall protein adsorp-

tion (Vroman effect) drives contact activation that initiates the coagulation reactions. At the same time, platelets adhesion and activation take place (Jaffer et al. [60]), constituting the platelet-fibrin clot that will form the stable thrombus.

In recent studies, computational fluid dynamics has been used to predict the flow in medical devices, with the long-term objective of improving their thrombotic performance (Alemu et al. [4], Piatti et al. [92]). However, most of the thrombus formation models are dedicated to platelet activity or in-vivo situations in which no medical device is present. For instance, numerical studies that consider platelet activity are notably focused on the characterization of mechanical activation of platelets (Hellums [54], Kroll et al. [65], Jetsy et al. [61], Nobili et al. [89], Shadden and Hendabadi [102]). In contrast, in-vivo models are based on a series of reaction equations modeling the coagulation cascade, from the exposure of tissue factor to the generation of thrombin (Sorensen et al. [109], Kuharsky and Fogelson [67], Fogelson and Guy [42], Anand et al. [8], Seo et al. [100], Yazdani et al. [126]). Generally, in vivo models, prescribe an injury zone determined by the user producing tissue factor and thus, initiating the coagulation reactions (Biasseti et al. [18], Seo et al. [100]). This type of approach cannot be used for device-related thrombosis due to the lack of a priori knowledge of the thrombotic zone. For this reason, the models dedicated to evaluate the device thrombotic performance have focused on platelet activity. For instance, Goodman et al. [46] developed a model to predict device-induced thrombosis based on platelet activation (agonist induced platelet activation as in [109] and mechanical platelet activation by shear stress). Furthermore, the model accounts for platelet adhesion to artificial surfaces and thrombus growth by substantially increasing the fluid viscosity. Taylor et al. [112] developed a macroscopic model that includes platelet activation and thrombus growth in regions related to high and low wall shear stress (WSS), respectively. Their model was derived from the work of Fogelson [40] with some modifications to account for device-related thrombosis.

While platelet activity has been extensively considered, other major players like the complement and contact activation systems must be included in the modeling, as pointed out by Gorbet and Sefton [47]. Moreover, considering contact activation could provide significant information to platelet models since one mechanism of their activation is due to thrombin as explained in Fogelson and Neeves [43], the latter being partially produced by reactions initiated by the contact system (Larsson et al. [69]). To the best of our knowledge, the only model considering the interaction of an idealized flow configuration and the contact activation system is the one of Gregory and Basmadjian [49]. In their work, a steady-state solution of a kinetic model is analyzed. The coagulation reactions in this model include contact activation of factor XII and the common pathway of the coagulation cascade (until factor XI_a). The model results showed significant sensitivity to the flow dynamics and surface activity. A

more recent kinetic model that considers the contact system in a platelet plasma kinetic network was developed by Chatterjee et al. [30]. Their model predicts the coagulation time of quiescent human blood samples without the action of tissue factor (TF). The results show that coagulation is due to the combined action of factors $XIII_a$ and XI_a .

In parallel, recent clinical studies have pointed at the contact activation phase as a promising therapeutic target providing an anticoagulant strategy without increasing the risk of bleeding (Jaffer et al. [60], Larsson et al. [69]). A model that incorporates the contact activation system and the coagulation reactions until thrombin formation coupled with a realistic representation of flow dynamics is thus needed. To this respect, the objective of this study is to evaluate the potential of the contact system to initiate thrombin production. The role of the anionic phospholipids (platelet activity), fibrin formation and fluid-structure interaction of a growing thrombus were thus neglected, since these phenomena, although prominent in the general thrombus formation mechanism, are not specifically involved in the surface production of thrombin. A surface-mediated thrombin production model is presented in a computational hemodynamics framework. The model accounts for interaction of the blood flow with the contact activation system and the rest of the blood coagulation cascade; it is detailed in Section 2.2, together with the numerical method. Furthermore, the model was applied to a device-characteristic flow configuration presented in the experimental work of Taylor et al. [111]. To this end, a specific boundary condition was developed to mimic the contact activation at the device surface. The results discussed in section 3 illustrate the potential of the approach.

2.2 Materials and Methods

2.2.1 Governing equations

Fluid dynamics equations

Flow dynamics is described by the incompressible Navier Stokes equations that read

$$\nabla \cdot \mathbf{u} = 0, \quad (2.1)$$

$$\rho \left(\frac{\partial \mathbf{u}}{\partial t} + \mathbf{u} \cdot \nabla \mathbf{u} \right) = -\nabla p + \mu \nabla^2 \mathbf{u}, \quad (2.2)$$

where \mathbf{u} is the velocity field, p is the pressure field, ρ stands for the density and μ is the dynamic viscosity (both assumed constant-valued). The blood was considered as a Newtonian fluid (constant viscosity) since the objective of the present study was not focused on the effects due to Non-Newtonian behavior of blood.

Convection-Diffusion-Reaction equations

To account for the coagulation reactions, a set of evolution equations (one for each coagulation factor) is solved. The equation that captures the spatial and temporal evolution of the biochemical species is widely known as the convection-diffusion-reaction equation

$$\frac{\partial C_i}{\partial t} + \nabla \cdot (C_i \mathbf{u}) = \nabla \cdot (D_i \nabla C_i) + R_i, \quad (2.3)$$

where C_i ($M = \text{mol L}^{-1} = 10^3 \text{ mol m}^{-3}$) and D_i ($\text{m}^2 \text{ s}^{-1}$) are the molar concentration and diffusion coefficients for each species i , R_i ($M \text{ s}^{-1}$) is the reaction source term (computed according to the reactions rates presented in Table 2.1).

2.2.2 Coagulation model

A wide variety of models has been proposed to predict thrombin formation inside the blood stream (Anand et al. [6], Leiderman and Fogelson [70], Biasetti et al. [18]). In those models, coagulation reactions start at the extrinsic pathway by the exposure of TF. In the present work, the presence of an artificial surface in contact with blood is accounted for by including the contact activation system (Basmadjian et al. [14]). For this purpose the kinetic model of Chatterjee et al. [30] is adopted. This set of reactions predicts thrombin production in the absence of exogenous TF and starts the coagulation reactions by the contact activation of factor *XII*. Figure 2.1 shows a schematic of the coagulation model used for the simulations including the contact activation system and the rest of the coagulation cascade reactions.

In Table 2.1, the 26 reactions used are listed with their respective reaction rates. The types of reaction kinetics are of first order, second order and Michaelis-Menten. Reaction rates for the different reactions are listed in three different columns according to their type. The source terms R_i appearing in Eq. 2.3 are deduced from the coagulation reactions. It is important to mention that the 53 reaction rates values do not consider the platelet activity that is also reported by Chatterjee et al. [30].

Diffusion coefficients were estimated with the correlation of Young et al. [128]. The molecular weight of each chemical species is needed to estimate the diffusion coefficient along with the temperature and the dynamic viscosity. For the present study a temperature of $T = 25 \text{ }^\circ\text{C}$ and a dynamic viscosity of $\mu = 3.71 \times 10^{-3} \text{ Pa s}$ were used. The correlation used considers a partial specific volume of $0.73 \text{ cm}^3 \text{ g}^{-1}$ which is assumed to be common for all the species. The expression proposed by Young et al writes:

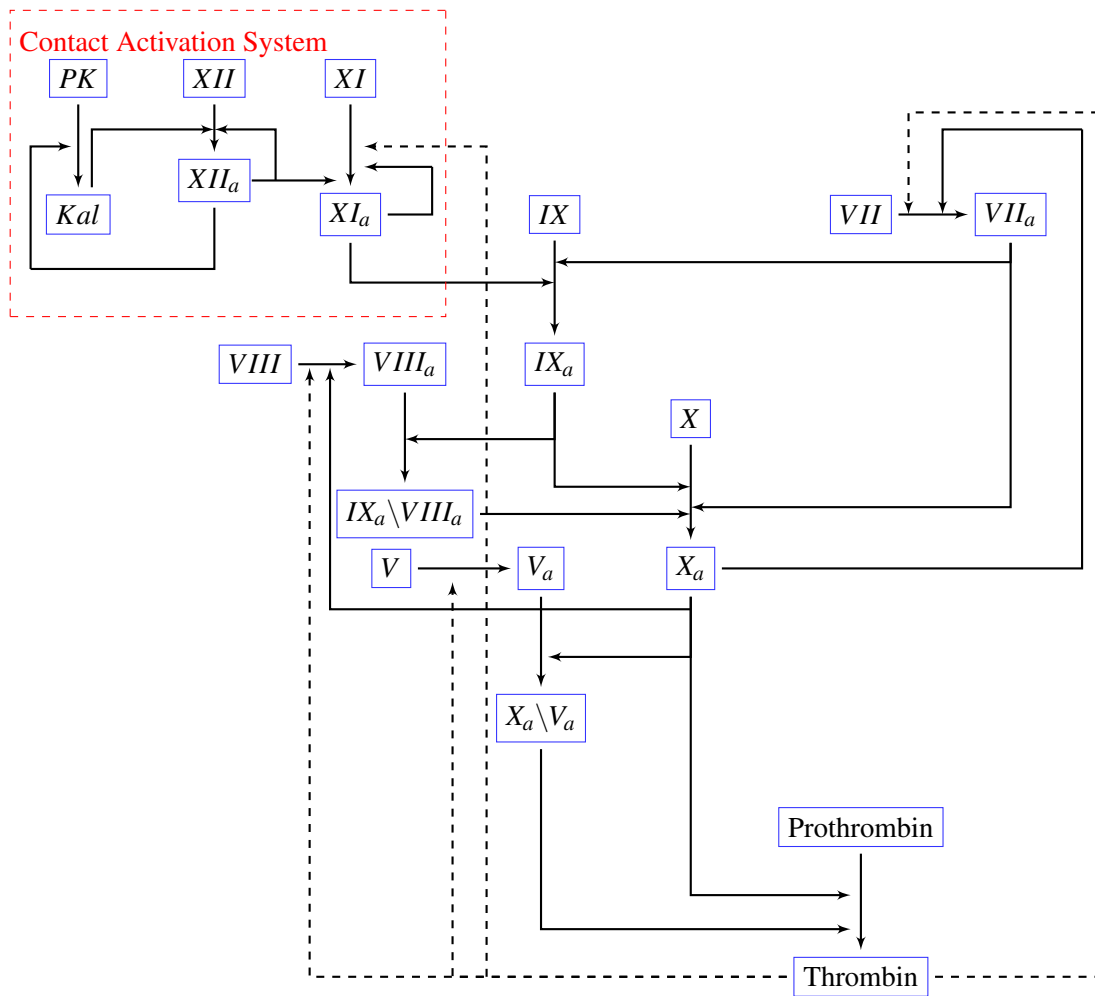


Fig. 2.1 Schematic of the coagulation reaction network. The kinetic network is inspired from the platelet-plasma model of Chatterjee et al. [30] without considering TF, inhibitors and fibrinogen reactions. The dashed lines correspond to the feedback loop reactions related to thrombin.

$$D = 8.34 \times 10^{-8} (T/\mu M)^{1/3} \quad (2.4)$$

The diffusion values estimated with Eq. 2.4 are extremely small (of the order of $10^{-11} \text{ m}^2 \text{ s}^{-1}$). If these values were to be used, numerical instabilities and large diffusion characteristic times would render the convergence to a steady state solution extremely difficult. This problem has been emphasized in studies using numerical models for coagulation. This difficulty is either overcome by refining the mesh which is hardly feasible except for 1D simulations, or by increasing artificially the diffusion coefficients as in Biasseti et al. [18]. Here, we follow the latter approach and multiply all diffusion coefficients by a factor of 1000.

The main objective of this work is to evaluate the potential of the contact activation system to initiate thrombin formation. Consequently, the model did not include inhibitors, TF and fibrin-related reactions that are included in Chatterjee et al. [30]. Finally the model assumes an infinite number of binding sites (infinite platelet supply), as in Biasseti et al. [18]. The reader is referred to Kuharsky and Fogelson [67], Anand et al. [6] for a discussion on the role of a finite number of binding sites.

It is important to note that the scope of this article is not to model the complete and complex dynamics of thrombus formation. A full model must include the role of anionic phospholipids, platelet adhesion and aggregation as in Leiderman and Fogelson [70]. Other important players for a robust model should be included such as fibrin production (Neeves et al. [86]), coagulation inhibitors (Zhu [130], Rice et al. [96]) or thrombus growth (solid-fluid interaction) as model by Ngoepe and Ventikos [88]. Such a comprehensive model may provide a good prediction tool to contribute to the optimization of medical devices. However, the potential of the contact activation system to initiate coagulation reactions is better assessed by focusing on this mechanism alone, without including all the other phenomena relevant to thrombus formation. This is the methodology followed in this study.

2.2.3 A boundary condition for the contact activation

To model the contact activation of factor *XIII*, a wall boundary condition is derived from the species mass balance at the wall where protein adsorption takes place followed by contact activation. The balance is obtained by integrating Eq. 2.3 over a rectangular control volume Ω (which includes a volume of fluid and a volume of wall, see Fig. 2) of surface Σ .

#	Reaction	Forward $M^{-1} s^{-1}$	Reverse s^{-1}	Forward s^{-1}
1	$Xa + VII \rightarrow Xa + VIIa$	$k_1 = 1.3 \times 10^7$		
2	$IIa + VII \rightarrow IIa + VIIa$	$k_2 = 2.3 \times 10^4$		
3	$II + Xa \rightarrow IIa + Xa$	$k_3 = 7.5 \times 10^3$		
4	$IIa + VIII \rightarrow IIa + VIIIa$	$k_4 = 2.0 \times 10^7$		
5	$VIIIa + IXa \leftrightarrow IXa + VIIIa$	$k_5 = 1.0 \times 10^7$	$k_6 = 5.0 \times 10^{-3}$	$k_9 = 8.2$
6	$IXa = VIIIa + X \leftrightarrow IXa = VIIIa = X \rightarrow IXa = VIIIa + Xa$	$k_7 = 1.0 \times 10^8$	$k_8 = 1.0 \times 10^{-3}$	$k_{11} = 2.2 \times 10^4$
7	$VIIIa \leftrightarrow VIIIa_1 \cdot L + VIIIa_2$		$k_{10} = 6.0 \times 10^{-3}$	
8	$IXa = VIIIa = X \rightarrow VIIIa_1 \cdot L + VIIIa_2 + X + IXa$		$k_{12} = 1.0 \times 10^{-3}$	
9	$IXa = VIIIa \rightarrow VIIIa_1 \cdot L + VIIIa_2 + IXa$		$k_{13} = 1.0 \times 10^{-3}$	
10	$IIa + V \rightarrow IIa + Va$	$k_{14} = 2.0 \times 10^7$		
11	$Xa + Va \leftrightarrow Xa + Va$	$k_{15} = 4.0 \times 10^8$	$k_{16} = 0.2$	
12	$Xa = Va + II \leftrightarrow Xa = Va = II \rightarrow Xa = Va + mIIa$	$k_{17} = 1.0 \times 10^8$	$k_{18} = 103$	$k_{19} = 63.5$
13	$Xa = Va + mIIa \rightarrow Xa = Va + IIa$	$k_{20} = 1.5 \times 10^7$		
14*	$XII \rightarrow XIIa$			
15	$XIIa + XII \leftrightarrow XIIa = XII \rightarrow XIIa + XIIa$	$k_{22} = 1 \times 10^8$		$k_s = 5.0 \times 10^{-7} ms^{-1}$
16	$XIIa + PK \leftrightarrow XIIa = PK \rightarrow XIIa + K$	$k_{25} = 1 \times 10^8$	$k_{23} = 750$	$k_{24} = 3.3 \times 10^{-2}$
17	$XII + K \leftrightarrow XII = K \rightarrow XIIa + K$	$k_{28} = 1 \times 10^8$	$k_{26} = 3.6 \times 10^3$	$k_{27} = 40$
18	$PK + K \rightarrow K + K$	$k_{31} = 2.7 \times 10^4$	$k_{29} = 45.3$	$k_{30} = 5.7$
19	$XI + IIa \leftrightarrow XI = IIa \rightarrow XIa + IIa$	$k_{32} = 1 \times 10^8$	$k_{33} = 5$	$k_{34} = 1.3 \times 10^{-4}$
20	$XIIa + XI \leftrightarrow XIIa = XI \rightarrow XIIa + XIa$	$k_{35} = 1.0 \times 10^8$	$k_{36} = 200$	$k_{37} = 5.7 \times 10^{-4}$
21	$XIa + XI \rightarrow XIa + XIa$	$k_{38} = 3.19 \times 10^6$		
22	$XIa + IX \leftrightarrow XIa = IX \rightarrow XIa + IXa$	$k_{39} = 1.0 \times 10^8$	$k_{40} = 41.0$	$k_{41} = 7.7$
23	$IXa + X \leftrightarrow IXa = X \rightarrow IXa + Xa$	$k_{42} = 1.0 \times 10^8$	$k_{43} = 0.64$	$k_{44} = 7.0 \times 10^{-4}$
24	$Xa + VIII \leftrightarrow Xa = VIII \rightarrow Xa + VIIIa$	$k_{45} = 1.0 \times 10^8$	$k_{46} = 2.1$	$k_{47} = 0.023$
25	$VIIIa + IX \leftrightarrow VIIIa = IX \rightarrow VIIIa + IXa$	$k_{48} = 1.0 \times 10^8$	$k_{49} = 0.9$	$k_{50} = 3.6 \times 10^{-5}$
26	$VIIa + X \leftrightarrow VIIa = X \rightarrow VIIa + Xa$	$k_{51} = 1.0 \times 10^8$	$k_{52} = 210$	$k_{53} = 1.6 \times 10^{-6}$

Table 2.1 Coagulation reactions. Kinetic parameters and coagulation reactions used in the simulations. Reaction 14 is taken into account only at the surface by means of the wall boundary condition. Parameter k_s units ($m s^{-1}$) correspond to a surface reaction; its value was obtained by adapting the volume reaction rate from Chatterjee et al. [30].

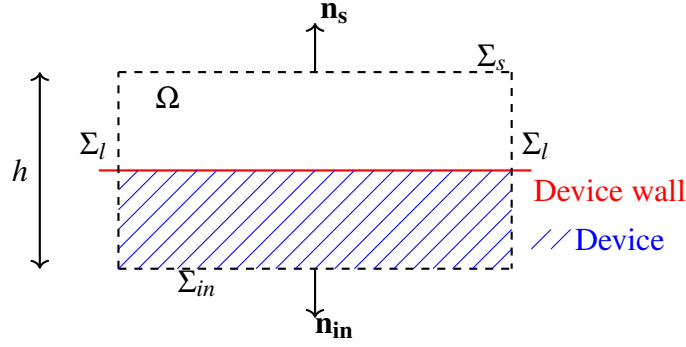


Fig. 2.2 Mass balance around the device wall. Ω Control of volume, Σ Surface envelope of the control volume, Sub index *in*, *s* and *l* stand for the inferior, superior and lateral surfaces respectively, h height of the control volume.

Using the divergence theorem to reformulate the conservative terms and integrating over Ω leads to:

$$\int_{\Omega} \frac{\partial C_i}{\partial t} d\Omega + \int_{\Omega} -R_i d\Omega = \int_{\Sigma} (D_i \nabla C_i) \cdot \mathbf{n} d\Sigma - \int_{\Sigma} C_i \mathbf{u} \cdot \mathbf{n} d\Sigma \quad (2.5)$$

The reaction source term R_i can be decomposed into the volume (blood-phase) reaction source term $\hat{\omega}_i$ and the surface source term \hat{s}_i multiplied by a Dirac function δ (which is no zero at the device surface). The mass balance becomes:

$$\int_{\Omega} \frac{\partial C_i}{\partial t} d\Omega + \int_{\Omega} -(\hat{\omega}_i + \delta \hat{s}_i) d\Omega = \int_{\Sigma} (D_i \nabla C_i) \cdot \mathbf{n} d\Sigma - \int_{\Sigma} C_i \mathbf{u} \cdot \mathbf{n} d\Sigma \quad (2.6)$$

The surface Σ can be separated in lateral, inferior and superior surfaces respectively $\Sigma = 2\Sigma_l + \Sigma_{in} + \Sigma_s$. If the height h tends to zero ($h \rightarrow 0$) the volume integrals over Ω and the surface integrals over the lateral surfaces Σ_l are equal to zero; the inferior surface Σ_{in} collapse with the device wall and the surface reaction source term can be transformed in a surface integral over the device wall thanks to the Dirac function. In addition the convection fluxes at the device surface are equal to zero (assuming the wall is at rest and impermeable), thus Eq.2.5 can be rewritten as:

$$- \int_{\Sigma_s} (D_i \nabla C_i) \cdot \mathbf{n}_s d\Sigma_s = \int_{\Sigma_{in}} (D_i \nabla C_i) \cdot \mathbf{n}_{in} d\Sigma_{in} + \int_{\Sigma_{in}} \hat{s}_i d\Sigma_{in} \quad (2.7)$$

The diffusion flux inside the solid domain is zero since no species is present in the device itself; thus one can write:

$$-\int_{\Sigma_s} (D_i \nabla C_i) \cdot \mathbf{n}_s d\Sigma_s = \int_{\Sigma_{in}} \dot{s}_i d\Sigma_{in} \quad (2.8)$$

A boundary condition can be obtained by applying Eq. 2.8 to factor XII_a . The surface source term is obtained assuming an infinitely fast adsorption and an infinite number of binding sites for factor XII , thus the reaction that takes places is the conversion of the near-wall factor XII (indexed by w) to XII_a . Finally the following wall boundary condition is obtained:

$$D_{XII_a} \frac{\partial C_{XII_a}}{\partial n} = -k_s C_{XII_w} \quad (2.9)$$

where k_s is a material property (surface reaction rate) and the direction n is the normal direction pointing to the blood-phase of the domain. In this study the value published in Chatterjee et al. [30] for the activation of factor XII in a perfectly mixed environment (volumetric reaction rate) was converted to a surface reaction rate k_s . From a straightforward dimensional analysis, one obtains $k_s \sim k_v \frac{V_{batch}}{S_{batch}}$ where V_{batch} and S_{batch} are the characteristic volume and the active surface of the experimental set up respectively. The surface reaction rate $k_s = 5.0 \times 10^{-7} \text{ ms}^{-1}$ is retrieved by using $V_{batch} \sim 10 \mu\text{L}$ and $S_{batch} \sim 0.1 \text{ cm}^2$ following the experimental values reported in Chatterjee et al. [30]. A range of values was also considered to investigate the effect of this physical quantity on the results (see section 2.3).

2.2.4 Numerical implementation and verification

Equations 4.7 and 4.8 were solved with a fourth-order finite-volume method on an unstructured grid, implemented in the in-house YALES2BIO¹ solver. YALES2BIO is based on a massivel parallel finite volume solver for incompressible flows (Moureau et al. [84]) and has been extensively validated for several biomedical applications at micro and macro scale (Chnafa et al. [33, 31], Mendez et al. [76], Sigüenza et al. [105], Chnafa et al. [34], Lanotte et al. [68], Zmijanovic et al. [131]). It uses a spatial fourth-order scheme with an explicit four-step Runge-Kutta scheme in time. The pressure term is handle with the Chorin's projection-correction method. Equation 2.3 was also solved using a fourth-order scheme in space and time for each species. Several test cases were developed to verify the implementation of Eq. 2.3 in YALES2BIO. Test cases with reactions of the Michaelis-Menten type (Michaelis et al. [81]), as well as first and second order reactions were compared against analytic solutions. Furthermore, the results of the kinetic model introduced by Hockin

¹<http://www.math.univ-montp2.fr/~yales2bio/>

et al. [57] were reproduced. In this test case the reactions start with an initial condition of exogenous TF. This allows to validate the different types of reactions that are shared by the different coagulation kinetic schemes; for instance, reactions 1 to 13 in Table 2.1 are shared with the scheme of Hockin et al. [57].

Moreover, a simple 1D diffusive test case involving a volume and a surface reaction (contact activation boundary condition) without convection was specifically designed during the course of this study. In this academical configuration illustrated in Fig. 2.3, a species A can be either activated at the bottom wall and become A_a (surface reaction rate k_s) or transformed into species B in the flow domain (volume reaction rate k_v), whereas the upper wall acts like an infinite reservoir at concentration $C_A(h) = \alpha$. In the calculations the domain is 2D, with periodic conditions in the directions tangential to the walls. The analytic steady state solution for the concentration of species A reads:

$$C_A(y) = \frac{\alpha e^{\beta(h-y)}(k_s(e^{2\beta y} - 1) + \beta D_A(1 + e^{2\beta y}))}{k_s(e^{2\beta h} - 1) + \beta D_A(1 + e^{2\beta h})} \quad (2.10)$$

where k_s and k_v are the surface and volume reaction rates, respectively, $\beta = \sqrt{\frac{k_v}{D_A}}$ and h is the channel height. Table 2.2 shows the three different operating points that were used to verify the results.

Cases	$k_s \text{ m s}^{-1}$	$k_v \text{ s}^{-1}$
Case ₁	1.0×10^{-4}	1.0×10^4
Case ₂	1.0×10^{-4}	1.0×10^3
Case ₃	1.0×10^{-2}	1.0×10^2

Table 2.2 Operating points. The different set of parameters (k_s and k_v) used for the verification of the code. The corresponding steady state solutions are shown in Fig. 2.3.

Figure 2.3 shows the steady state solution of species A for both the numerical and analytic cases. An excellent agreement is obtained for all of the operating points.

2.2.5 Backward facing step configuration

Numerical simulations are performed in a backward facing step (BFS) configuration presented in Fig. 2.4, advancing the set of reactions presented in Table 2.1. This type of configuration involves a flow separation that several medical devices could feature and which has been related to thrombus formation (Hastings et al. [53], Taylor et al. [111]). The step height

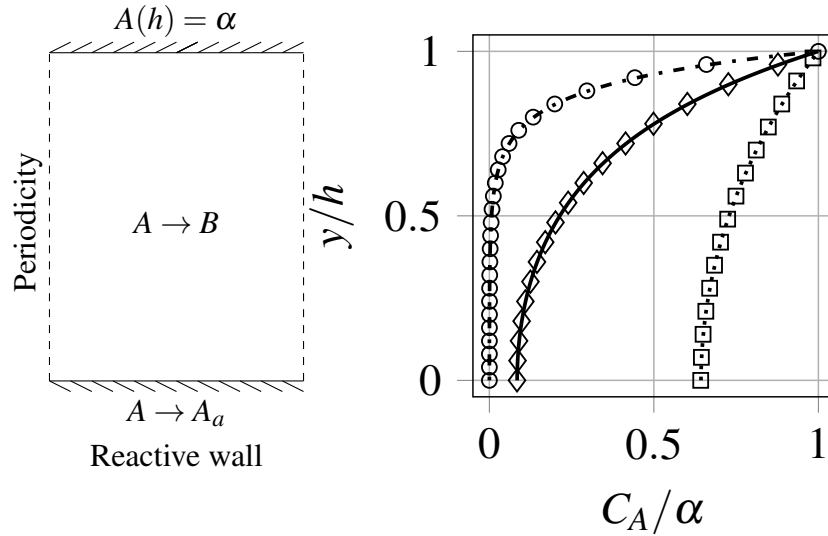


Fig. 2.3 1D reaction-diffusion test case. $C_A = \alpha = 1.0 \mu\text{M}$, initial volume concentration of all the species $C_i = 0 \text{ M}$, diffusion coefficient of species $D_A = D_B = 1.0 \times 10^{-2} \text{ m}^2 \text{ s}^{-1}$, channel height $h = 0.01 \text{ m}$. Numerical results (*Case*₁ \circ , *Case*₂ \diamond , *Case*₃ \square) and analytic Eq. 2.10 data (*Case*₁ \cdots , *Case*₂ — , *Case*₃ \cdots).

$h_s = 2.5 \text{ mm}$ and vessel height $H = 10 \text{ mm}$ match the experimental dimensions presented by Taylor et al. [111].

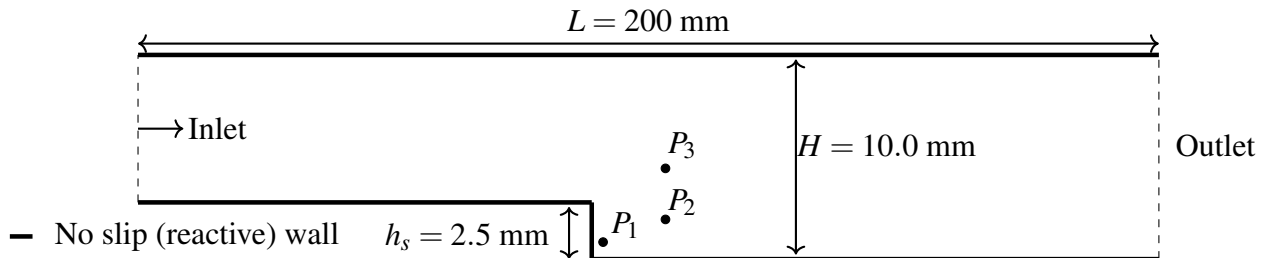


Fig. 2.4 2D Backward facing step computational domain. P_i are the locations of the probes used in Figs. 2.5, 2.7 and Fig. 2.12 ($P_1 = (0.5, 0.5)$, $P_2 = (4.0, 1.5)$, $P_3 = (4.0, 4.0)$ mm); the step and channel heights match the experimental values of Taylor et al. [111]. The thick black line denotes the solid boundary where boundary condition Eq. 2.9 is applied and activation of factor XII is allowed.

The inlet and outlet conditions were placed at a distance of $10H$ to avoid boundary effects on the region of interest located downstream of the step: the expected recirculation zone for the flow regime considered (Reynolds number $Re = 430$, based on the inlet channel height and the upstream bulk velocity) is $Xr = 8.9h_s$ according the results of Kim and Moin [63]. The kinematic viscosity was set to a constant value $\nu = 3.5 \times 10^{-6} \text{ m}^2 \text{ s}^{-1}$.

Boundary and initial conditions. The inlet velocity was set to $U_x = 0.2 \text{ m s}^{-1}$, consistently with the experimental conditions described in Taylor et al. [111]. Table 2.3 shows the initial and inlet boundary conditions factors that were taken from Chatterjee et al. [30] and which correspond to physiological values. The boundary and initial conditions for the rest of the factors were set to zero. One of the most important features of the simulation is the reactive surface boundary condition, Eq. 2.9. The boundary condition for the contact activation of factor *XII* was applied at the entire wall of the computational domain (see Fig. 2.4).

Factor	Concentration (M)
<i>VII</i>	1.0×10^{-8}
<i>VIIa</i>	1.0×10^{-10}
<i>X</i>	1.6×10^{-7}
<i>IX</i>	9.0×10^{-8}
<i>II</i>	1.4×10^{-6}
<i>VIII</i>	7.0×10^{-10}
<i>V</i>	2.0×10^{-8}
<i>XII</i>	3.4×10^{-7}
<i>PK</i>	4.5×10^{-7}
<i>XI</i>	3.1×10^{-8}

Table 2.3 Initial and inlet factor concentrations. Physiological values used in the simulations taken from Chatterjee et al. [30].

Spatial and temporal resolution. Several grids were used to ensure that the simulations yield results independent from the grid used in the calculation. Table 2.4 shows the representative cell size and the number of elements used for the computations. The simulation time step is given by the Courant-Friedrichs-Levy stability condition which is define using the time step Δt , the local velocity field u and the mesh size Δx as $CFL = \frac{u\Delta t}{\Delta x} \leq 1$. The value used in the current simulations is $CFL = 0.9$ which corresponds to a time step of the order 10^{-4} s.

Grid	Δ_h (μm)	Elements $\times 10^3$
Coarse	70	367
Medium	60	484
Fine	52	646

Table 2.4 Mesh properties. Δ_h is the representative cell size computed as in Celik et al. [27] and the total number of grid elements (triangles) are displayed.

2.3 Results: Backward facing step

2.3.1 Flow Dynamics

The velocity field reached a steady state solution before 1.0 s as shown in Fig. 2.5 for different spatial point probes located inside and outside the recirculation zone.

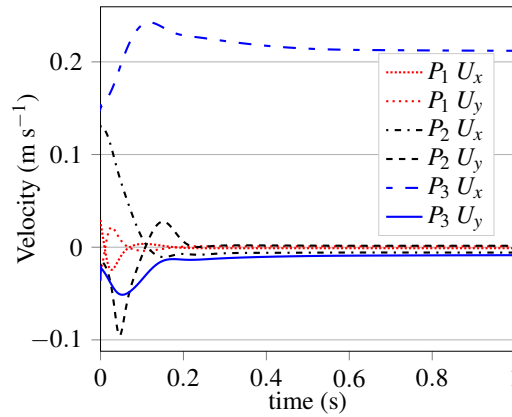


Fig. 2.5 Temporal evolution of x and y velocity components in different point probes.

Figure 2.6 shows the steady state velocity field as well as the streamlines that allow the visualization of recirculation region after the step. The reattachment length X_r is in good agreement with the numerical and experimental results published in Kim and Moin [63], Armaly et al. [11] which lead to $X_r = 8.9h$. The comparison was performed for all the grids used in this study. The percentage error of the coarser mesh was $e_{rel} = 3.1\%$ and for the medium and fine mesh of about $e_{rel} = 2.9\%$ which is a fair approximation considering the main objective of the current study.

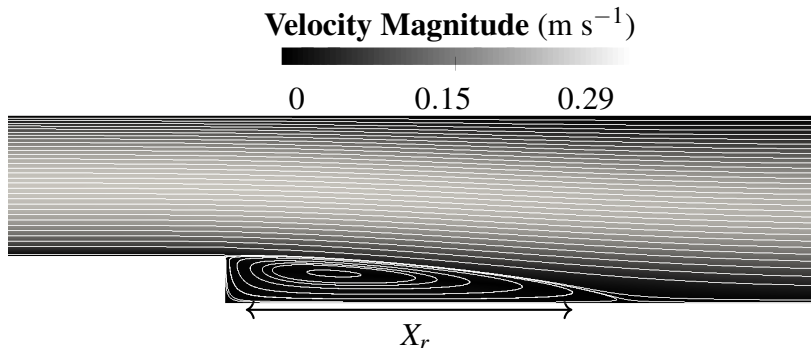


Fig. 2.6 Velocity magnitude with white stream lines. The reattachment length X_r is shown.

2.3.2 Coagulation cascade

In order to quantify the outcome of the coagulation cascade, the value of total thrombin is considered ($II_a + 1.2mII_a$ is a quantitative measure of thrombin activity in the system, according to Hockin et al. [57]). First, a mesh convergence study was performed using the mean value of the total thrombin in the computational domain. The methodology published in Celik et al. [27] was used. The convergence grid index is used to quantify the distance of a computed value (simulation result) to the asymptotic value estimated by an extrapolation method using the different levels of discretization. For the finest mesh the convergence grid index obtained was $CGI_{finest} = 0.41\%$ with a relative extrapolated error of $e_{ext} = 0.33\%$, the quantity used for the analysis was the total thrombin concentration value of a point probe inside the recirculation region. These values ensure that the total thrombin concentration field would not substantially change with even a finer mesh. The surface rate used for the mesh convergence study was $k_s = 5.0 \times 10^{-4} \text{ m s}^{-1}$, in order to reduce the computational cost of the study.

Figure 2.7 shows the time evolution of total thrombin at point probes P_1 , P_2 and P_3 (see Fig. 2.4 for the location of the probes). The time response is characterized by a lag time of about 100 s. Then, a propagation phase is observed until a small peak which evolves into a more stable plateau close to the inlet value of $II = 1.4 \mu\text{M}$.

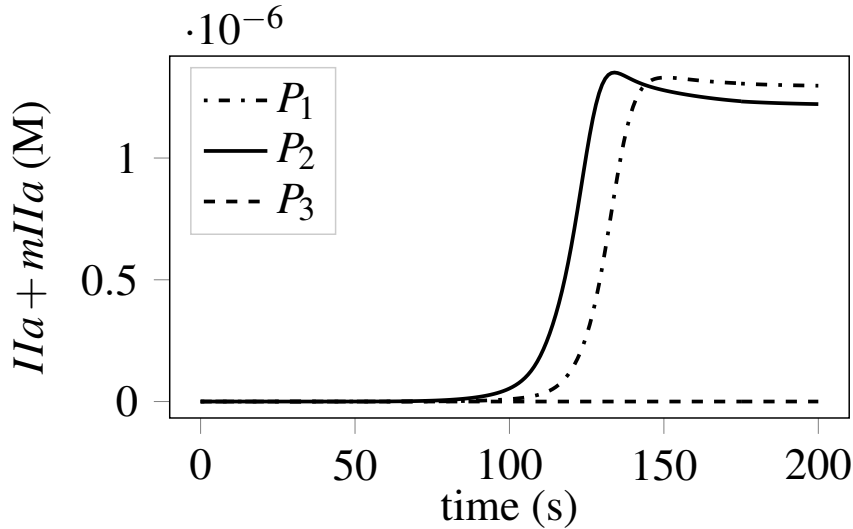


Fig. 2.7 Time evolution of $II_a + 1.2mII_a$ for each point probe (see Fig. 2.4). P_1 is near the wall region, P_2 inside the recirculation zone and P_3 outside the recirculation region.

Figure 2.8 a) shows the concentration field evolution of total thrombin at different time values. It can be observed that the region of largest total thrombin concentration is located inside the recirculation zone downstream of the step. Large concentrations of total thrombin extend further downstream at the lower wall. The numerical results are contrasted against the experimental data in Fig. 2.8 b) and c) which show the location of thrombus formation.

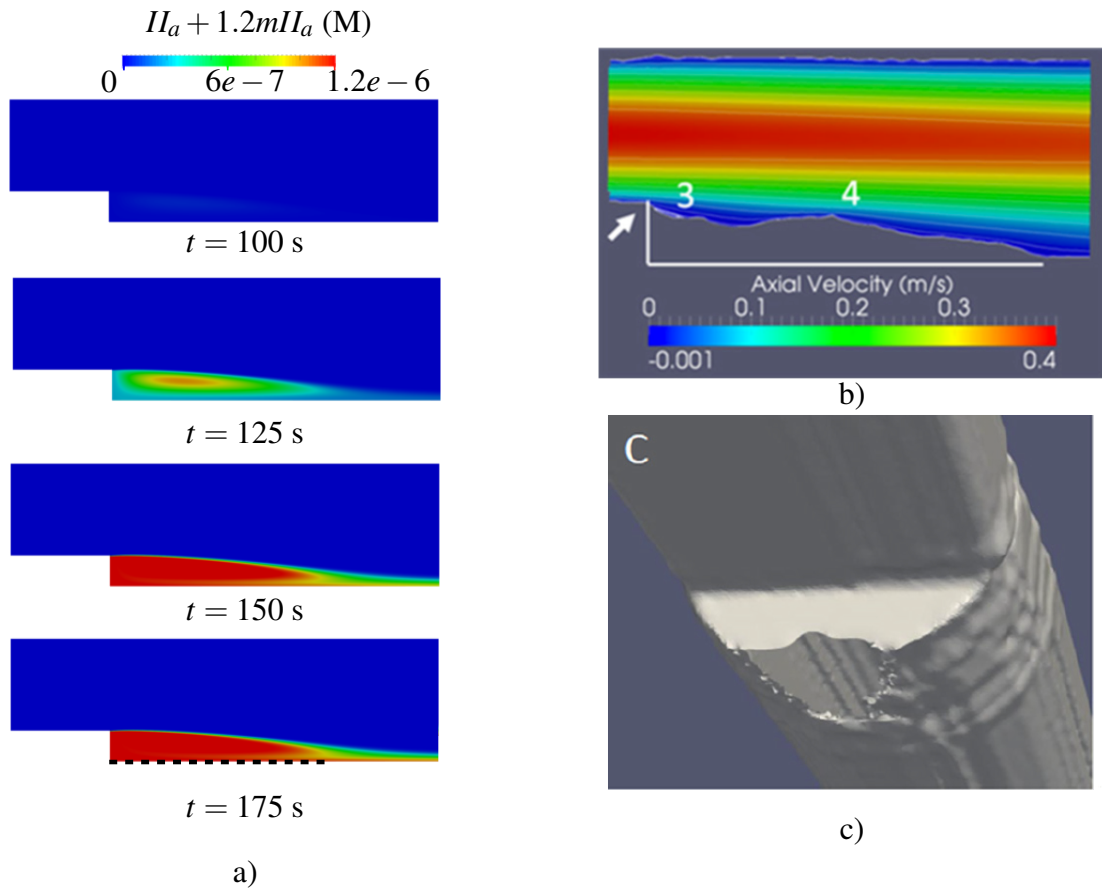


Fig. 2.8 a) Total thrombin concentration field at $t = 100, 125, 150$ and 175 s. The black dashed line represents over which total thrombin is plotted in Fig. 2.9. b) is taken from Taylor et al. [111] showing the velocity field around the thrombus at the BFS (inside the thrombus the velocity is not showed) c) the 3-dimensional form of the thrombus is showed, again the image is taken from Taylor et al. [111]

The local concentration of coagulation factors inside the recirculation region is shown in Fig. 2.9. The plot is extracted along a profile located at the half height of the step (h_s), $y = 1.25$ mm. It can be observed that the largest concentration of total thrombin is located at the step wall.

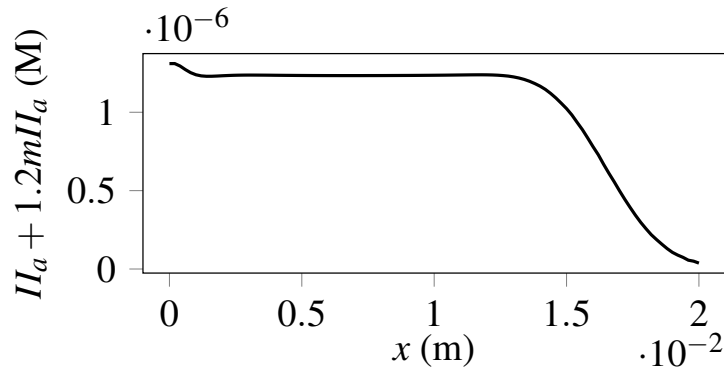


Fig. 2.9 $II_a + 1.2mII_a$ concentration in the recirculation zone.

A simulation including the inhibitor *ATIII* was performed as a first attempt to evaluate the production of thrombin. Figure 2.10 shows the evolution of thrombin over the time for probe P_1 and the concentration of thrombin at $t = 400$ s. This results were not converged to the steady state solution due to the high computational cost. Relevant levels of thrombin are produce to other physiological processes such as firbinogen polymerization or platelet activation.

Thrombin concentration levels at the recirculation region are large enough to form a stable thrombus (Biasetti et al. [18]). Furthermore, the zone with the largest concentration of thrombin aligns well with the experimental zone in which thrombus is formed (Taylor et al. [111]).

In macroscopic applications, flow metrics such as the wall shear stress are commonly used to evaluate the thrombogenic performance of medical devices. Such flow quantities are practical to use due to their low computational cost compared to a reacting flow study. It is thus interesting to investigate how the outcome from the contact system and the wall shear stress correlate. Figure 2.11 shows a scatter plot of the wall shear stress against the near wall concentrations of factors XII_a and XI_a . The quantities were normalized by the maximum wall shear stress and maximum concentrations of species XII_a and XI_a . Factor XII_a is clearly not correlated to WSS. Even though a clear correlation is not observed neither for XI_a , this factor takes its largest values in areas where WSS is small. At the end, these results demonstrate that accounting for the contact system generates a physical behaviour which cannot be properly represented by WSS-based flow analysis.

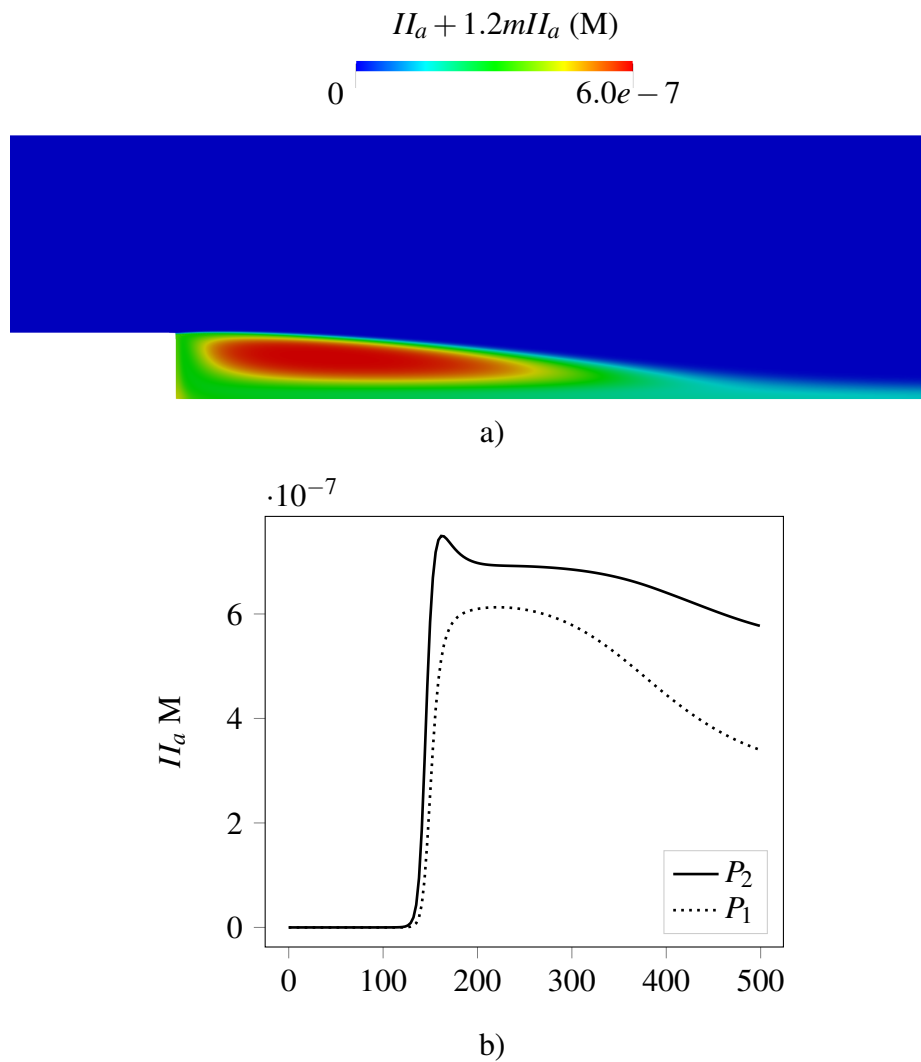


Fig. 2.10 Simulations including inhibitor *ATIII* and related reactions. a) Thrombin concentration at $t = 400$ s is shown in the upper part. b) Evolution of thrombin concentration at point probes P_1 and P_2 is shown in the lower part.

2.3.3 Parametric studies

Influence of surface kinetics k_s

As already mentioned, there is a lack of reliable data about the surface reaction rate (k_s contact activation) and this quantity may depend on the material type. The nominal value ($k_s = 5.0 \times 10^{-7} \text{ m s}^{-1}$) was obtained from the conversion of the volume reaction rate published in Chatterjee et al. [30], as previously explained, using a dimensional analysis that involves the characteristic volume and the active surface from the experimental set up reported in Chatterjee et al. [30]. To investigate how the outcome of the simulations depends

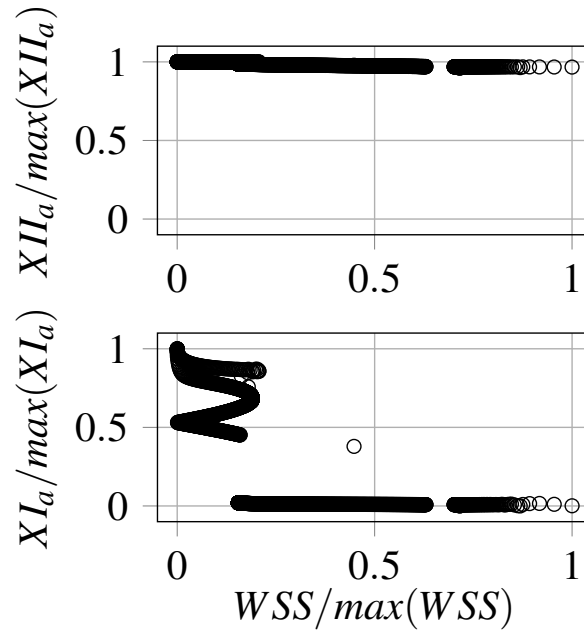


Fig. 2.11 Scatter plot of wall shear stress and wall concentrations of factors XII_a and XI_a .

on this parameter, a parametric study was performed. Six values were considered in the range $k_s = [5.0 \times 10^{-5}, 5.0 \times 10^{-10}] \text{ m s}^{-1}$ spanning six orders of magnitude. Figure 2.12 shows the evolution at point probe P_1 of factors XII_a , XI_a and $II_a + 1.2mII_a$ over time. In addition, inserts in the plots display the variation of specific times of interest with respect to k_s . For $II_a + 1.2mII_a$ and XII_a , the inflection point of the time evolution graphs is extracted by fitting a hyperbolic tangent function. For factor XI_a , the insert shows the time at which the maximum concentration is reached. The thrombin generation starts earlier as the parameter k_s is increased. However, while five orders of magnitude are explored for the value of k_s , the impact on the thrombin generation time is moderate and the dependence appears to be logarithmic. In addition, the total thrombin concentration fields (steady state solution) were compared, showing no significant difference. It can be observed from the evolution of factors XII_a and XI_a that the time delay present in the dynamics of these factors follow the same trend as the one observed for $II_a + 1.2mII_a$. In other words, the initial delay in the activation of factor XII is directly responsible for the delay in thrombin generation. While the influence of k_s on the time needed for generation of factor XII_a is very large, this time has to be compared with the total time needed for the rest of the coagulation cascade, which is 10 times larger in the present case. It is important to note that when k_s was set to zero the thrombin concentration levels remained close zero (not shown).

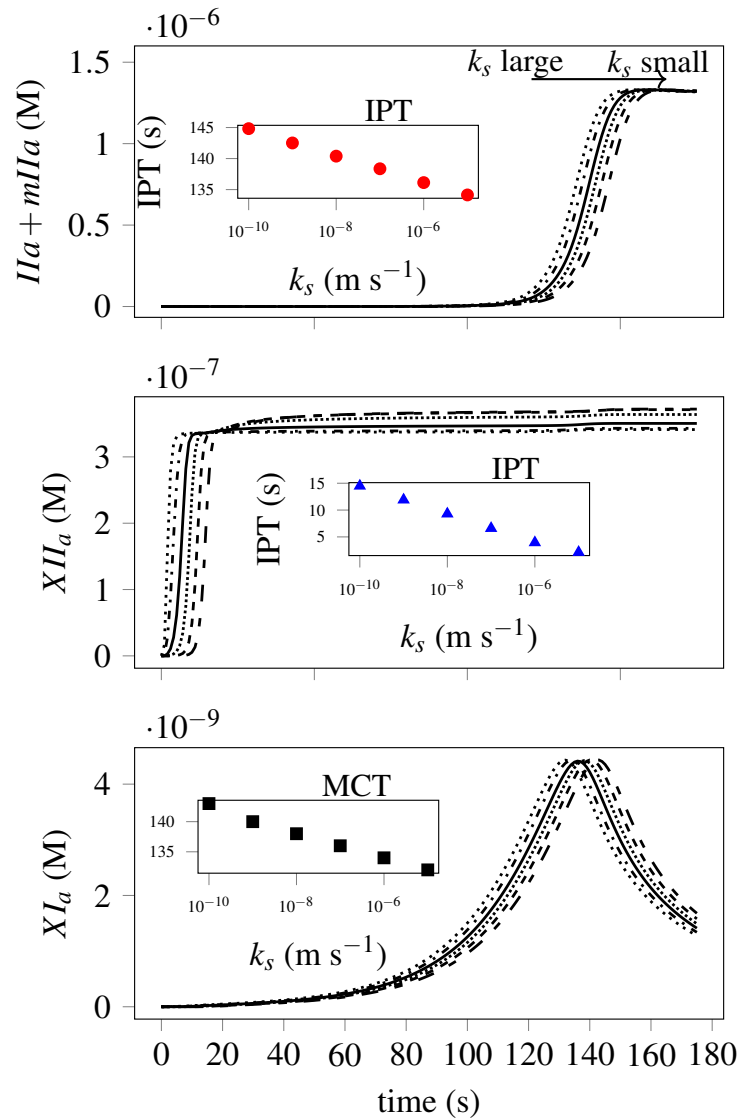


Fig. 2.12 Time evolution at point probe P_1 of total thrombin (upper), activated factor XII (medium) and activated factor XI (bottom). $k_s = 5 \times 10^{-5}$ (.....), $k_s = 5 \times 10^{-6}$ (- · - · -), $k_s = 5 \times 10^{-7}$ (—), $k_s = 5 \times 10^{-8}$ (.....), $k_s = 5 \times 10^{-9}$ (- - -), $k_s = 5 \times 10^{-10}$ (- -). The insets of $II_a + 1.2mII_a$ and XII_a factor show the Inflection Point Time (IPT) for each k_s value. For factor XI_a , the inset displays the maximum concentration time (MCT) as a function of k_s .

Influence of factor XII inlet boundary condition.

A parametric study on the influence of the concentration of factor XII at the inlet of the domain was also performed. This allows to evaluate the variability of the results to different samples with deficient factor XII . Table 2.5 shows the four different concentration values that were used for this purpose.

Case	XII (μM)
1	0.306
2	0.272
3	0.17
4	0.102

Table 2.5 Factor XII inlet concentrations used in the parametric study. These values correspond to 90%, 70%, 50% and 30% of the nominal concentration reported in Table 2.3.

Figure 2.13 shows the time evolution of factors XII_a , XI_a and $II_a + 1.2mII_a$ at the point probe P_1 . For each case, factor XII_a reaches a plateau equal to the inlet concentration of factor XII , as expected. The results show longer lag times for thrombin propagation as the concentration of factor XII is decreased. Interestingly the maximum production of factor XI_a is increased as factor XII concentration is reduced. This can be explained by the fact that a larger proportion of the available factor XI is activated by factor II_a (reaction 19) in this case, instead of being generated by factor XII_a (reaction 20). This behavior is confirmed by the time evolution of the source term of reactions 19 and 20 (not shown) and is also coherent with the reverse rate of reaction 19 (k_{33} in Table 2.1) being very small compared to the reverse rate of reaction 20 (k_{36} in Table 2.1). The results suggest that a small amount of activated factor XII (contact activation) is sufficient to initiate the thrombin propagation phase.

2.4 Discussion and Conclusion

Previous studies have modeled device-related thrombosis with an approach focussing on platelet activity (Goodman et al. [46], Taylor et al. [112]). However, the contact activation system is a key component of the thrombotic network (Larsson et al. [69], Jaffer et al. [60]) which up to date has not been included in a complete model of thrombus formation. The current model aims to serve as a first step towards the integration of the contact activation in a complete macroscopic thrombus formation model specific to medical devices. The current model was applied to a backward facing step configuration typical of medical devices.

One of the main features of the model is that it allows the initiation of the coagulation reactions without an a priori knowledge of the thrombotic zone. The results show that a significant amount of thrombin is generated in the recirculating region behind the backward facing step. This could be explained by comparing the characteristic residence and chemical times. Large residence time at the recirculating regions enhances the thrombin production reactions. Qualitatively, the model leads to higher total thrombin concentrations in regions

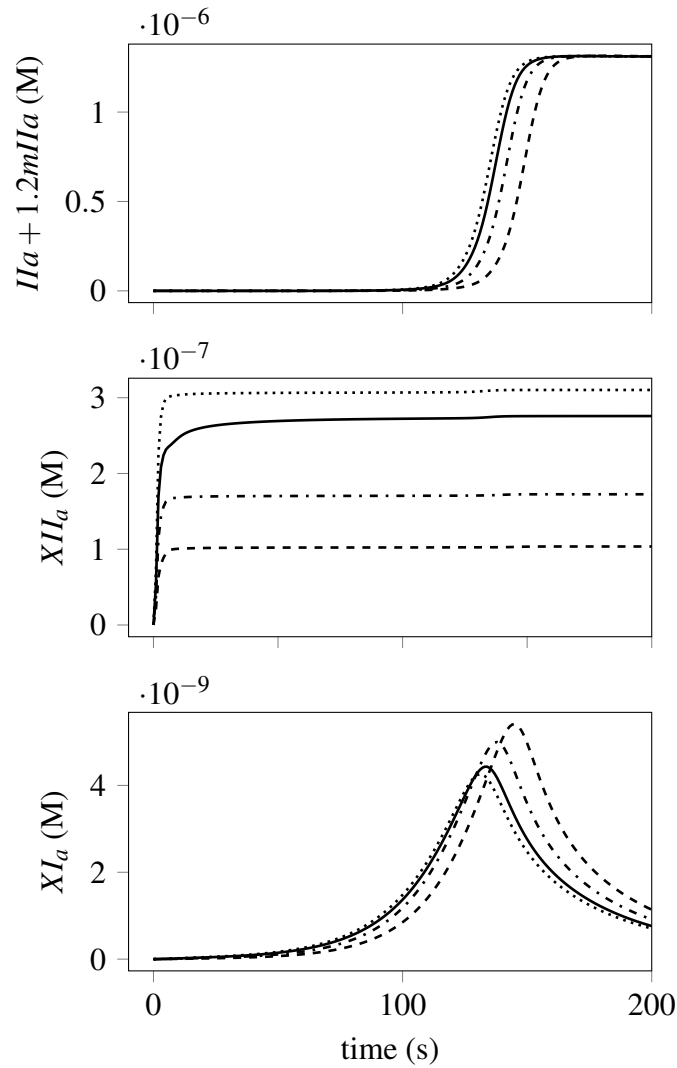


Fig. 2.13 Time evolution of point probe P_1 for total thrombin (upper), activated factor XII (medium) and activated factor XI (bottom) at point probe P_1 . The inlet and initial concentrations are $XII_{90\%} = 0.306 \mu M$ (---), $XII_{70\%} = 0.272 \mu M$ (-·-·-), $XII_{50\%} = 0.17 \mu M$ (—), $XII_{30\%} = 0.102 \mu M$ (·····).

where the thrombus formation was observed experimentally. The results also show a poor correlation between wall shear stress and near wall concentrations of factor XI_a , and no correlation for factor XII_a that is present all along the device surface. This suggests that the WSS should be complemented with other flow metrics that quantify diffusive and convective transports to characterize the thrombogenic performance of medical devices.

Molecular diffusivity of the species has been modified for numerical reasons (from $D_i \sim 10^{-11} \text{ m}^2 \text{ s}^{-1}$ to $D_i \sim 10^{-8} \text{ m}^2 \text{ s}^{-1}$), because the proper resolution of the species boundary layer would make the calculations prohibitive. However, it is most probably that if this

modification has a consequence, it is only in the sense of underestimating the thrombin generation by the contact system. First, in the main stream, convection clearly dominates, the Peclet number is of the order 10^7 and 10^4 for the molecular diffusivity of $D_i \sim 10^{-11} \text{ m}^2 \text{ s}^{-1}$ to $D_i \sim 10^{-8} \text{ m}^2 \text{ s}^{-1}$ respectively. In contrast, in the recirculation zone the results are controlled by the competition between reactions and diffusion. Large D_i values actually underestimate the local concentration of chemical species since they are diffused outside the recirculation region faster. The higher the diffusion coefficients, the lower the concentration of thrombin in the recirculation region. This is illustrated by two additional simulations with diffusion coefficient values of the order $D_i \sim 10^{-7} \text{ m}^2 \text{ s}^{-1}$ and $D_i \sim 10^{-6} \text{ m}^2 \text{ s}^{-1}$, which were performed to compare the concentration values inside the recirculation region. Figure 2.14 shows the underestimation of thrombin as the molecular diffusivity is augmented.

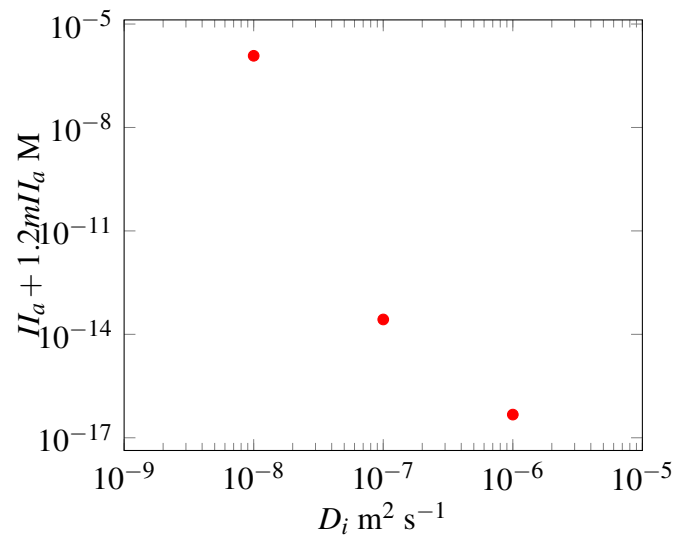


Fig. 2.14 Maximal total thrombin concentration inside the recirculation region for three orders of magnitude of the diffusion coefficients ($D_i \sim 10^{-8}, 10^{-7}, 10^{-6} \text{ m}^2 \text{ s}^{-1}$).

An interesting feature of the present model is that it includes a material property k_s (typical to each medical device) which is a novel feature for thrombus predictive models representing the kinetics of the contact surface reaction. A parametric study was performed on k_s showing a moderate influence of this parameter on the total thrombin generation, although it strongly modifies the generation time of factor XII_a . This is because the characteristic time of this later mechanism (reaction 14 in Table 2.1) is very small compared to the whole time required to generate thrombin.

In the end, the current study focuses on the contact system as one potential player in thrombin production. This approach could complement more complex models that consider platelet

activity, fibrin formation and fluid structure interaction of the growing thrombus, providing a proper initiation of the coagulation reactions in medical devices.

Chapter 3

Sensitivity analysis and model reduction

In this chapter a sensitivity analysis on the deterministic coagulation model from Chatterjee et al. [30] is performed. The general goal of the analysis is to identify the most sensitive kinetic parameters involved in the model. In a second part, a reduced set of reactions that forms thrombin is proposed, using the Bayesian statistical framework to infer the reaction rates involved in the model. One of the interesting features of the model is that it includes the contact activation system making it suitable for application in complex flow configurations happening in blood coated medical devices. This work has been submitted in *Biomechanics and Modeling in Mechanobiology*.

3.1 Introduction

The development of medical devices in contact with blood has been increasing over the last years. Such devices are used to treat cardiovascular or neurovascular disorders such as coronary artery diseases, heart valve diseases or aortic/brain aneurysms. One of the main problems of blood-coated devices is thrombus formation which can lead to device malfunction or thromboembolism [75, 119]. Blood clotting in devices is regulated by a series of intertwined biological processes, such as protein adsorption, platelet activity, complement system and coagulation reactions, as reviewed by Gorbet and Sefton [47]. These mechanisms appear due to the presence of the device whose artificial material lacks the endothelial properties of the vessel. At the material surface, contact activation of factor *XII* (zymogen of the coagulation cascade) takes place, initiating a cascade of enzymatic reactions [124] that produce thrombin, a key coagulation enzyme that activates platelets and forms fibrin. At the same time, platelet adhesion and activation can also occur at the device surface, as explained by Jaffer et al. [60]. In the last stage of the thrombus formation process, aggregated platelets

and polymerized fibrin form a stable clot that may hinder the device performance.

Computational fluid dynamics (CFD) has been used to study the flow on medical devices and evaluate the risk of thrombosis [127, 39]. A straightforward evaluation of thrombosis risk can be performed using specific flow patterns, such as high shear stress related to platelet activation [3, 102] or stasis which promotes coagulation [37]. Approaches focusing only on flow properties do not allow to study the biochemical processes, which play a major role in thrombus formation [43]. More exhaustive methods accounting for platelet activity, the coagulation cascade, clot growth and its interaction with the flow have been developed for thrombus triggered by vessel injury [70, 126]. However, only small computational domains $x \sim 100 \mu\text{m}$ can be considered due to the complexity of these models. Since a straightforward application of complicated models is not possible in the complex flow configurations linked to biomedical devices, reduced models accounting for platelet adhesion, activation (by chemical and mechanical pathways) and clot-flow interaction have been developed [112, 121]. Nevertheless, thrombin produced by the coagulation cascade triggered by the contact system has not been considered in a model of thrombus formation in devices.

The contact activation system has already been considered in kinetic models of the coagulation cascade [30, 130]. The kinetic descriptions have been used in CFD models to study thrombin formation triggered by the device wall in a typical flow configuration by Méndez Rojano et al. [77]. However, a straightforward coupling with platelet-based models is challenging due to the large number of reactions present in the kinetic models and the large physical time that must be computed in a thrombus growth process. Another issue is the large uncertainty in reactions rates due to non-standardized parameter characterization or variations among different subjects [36]. The uncertainty related to the kinetic models may lead to poor results in thrombin production as explained by Belyaev et al. [15].

Parameter uncertainty and kinetic model reduction have been addressed for models of thrombus generation initiated by Tissue Factor exposure which is related to endothelial damage. Danforth et al. [36] performed a sensitivity analysis on the kinetic model of Hockin et al. [57] to evaluate the sensitivity of thrombin generation to the 44 reaction rates that are present in the model. The model sensitivity was assessed using the one at time (OAT) methodology with linear spaced variations between 10 to 1000% of the normal reported rates value. The model outputs were evaluated at eight different instants which characterize the different phases of thrombin generation (initiation, amplification and propagation). Danforth and coworkers found that the model was especially sensitive to uncertainty in five parameters

involved in the formation of the $TF - VIIa$ complex which takes place at the initial part of the coagulation cascade. The authors suggest that improving the accuracy of the reaction rate measurement can improve the predictive capabilities of the kinetic model. In terms of model reduction, Wagenvoort et al. [116] showed that a model with a small number of reactions can reproduce the thrombin generation curve if it includes the basic mechanism of thrombin formation: initiation, amplification and propagation. Papadopoulos et al. [91] developed a minimal model for thrombin formation based on experimental data including these essential mechanisms. Reduced-order models allow computations in complex flow configurations. For instance, Ngoepe and Ventikos [88] used the reduced model of Wagenvoort et al. [116] to simulate thrombosis growth inside a cerebral aneurysm.

In the present work, a sensitivity analysis and a Bayesian inference method are used in device-related kinetic models. First, the kinetic model of Chatterjee et al. [30] initiated by the contact activation system is studied using a global screening technique that allows to identify the most sensitive parameters. Then, a reduced chemical model triggered by contact activation of factor XII is proposed. The optimal parameters of the reduced model are obtained using a data-driven Bayesian statistical framework to find the optimal parameters used in the reduced model.

3.2 Methods

3.2.1 Plasma Samples and TGA

Thrombin generation assay (TGA) was used to measure the evolution of thrombin concentration in time after coagulation was triggered by the contact activation system. Developed by Hemker et al. [55], the Calibrated Automated Thrombogram (CAT) is a test mainly used in hemostasis research to study the hemostatic profile. This method is time-consuming and suitable only for a small number of samples when compared to routine clinical tests which assess the first traces of thrombin (after coagulation is triggered) about 12 seconds for QT or 32 seconds for APPT for a normal plasma. In contrast, TGA assesses thrombin generation until 60 minutes and allows a better characterization of the coagulation cascade throughout all its phases initiation: amplification and propagation. Any traces of thrombin will cleave to a specific substrate $Z\text{-Gly-Gly-Arg-AMC}$ into a fluorescent form, detected by the thrombogram.

Samples: Biological assays were performed with pooled citrated platelet poor plasma (PPP) from healthy donors pooled normal plasma (PNP) [obtained from Cryopep, Montpellier France] to avoid any polymorphism factor. The plasma pool was diluted with thrombin

immunodeficient plasmas (qualified activity lower than 1% Siemens Healthcare, Erlangen, Germany) to obtain different final concentrations. Silica was used to trigger the coagulation, mixed with rabbit cephalin in STA-PPT A from Stago, Asnières-sur-Seine, France.

Calibrated automated measurement of thrombin generation: Thrombin generation was determined in PPP using Fluorocan Ascent (Flucakit, Thrombinoscope, Synapse BV, Maastrich, The Netherlands) according to the method described by Hemker et al. [55]. 80 μL of plasma were mixed with 20 μL of STA-PPT A and 20 μL of fluorescent reagent, FlucaKit. This reagent contains calcium chloride (necessary to trigger the coagulation cascade) and a mixture of fluorogenic substrate (Fluo-Substrate) and FluoBuffer. Thus, fluorescence intensity was detected at wavelengths of 390 nm (excitation filter) and 460 nm (emission filter), every 20 seconds. Each individual sample is analyzed with a thrombin calibrator as reference for a stable thrombin activity of 600 nM. The calibrator enables the conversion of the fluorescence signal into thrombin concentration. The signal is treated to correct inner filtering effects, substrate consumption and abnormal plasma color. Analyses were conducted, on Immulon 2HB round-bottom 96-well plates (Stago - Asnières-sur-Seine, France).

3.2.2 Detailed coagulation model

Sensitivity analysis is performed on the model introduced by Chatterjee et al. [30]. The model includes 37 reactions and 63 reaction rates and features:

- Initiation by the contact activation system considering factor XII auto-activation, reciprocal activation (by Kallikrein) and auto-hydrolysis (by factor XII_a),
- Extrinsic and common pathways following the model of Hockin et al. [57],
- Inhibition including Antithrombin ($ATIII$), Kallikrein inhibitor K_{inh} and C_1 inhibitor $C1_{inh}$.

#	Reaction	Forward $M^{-1} s^{-1}$	Reverse s^{-1}	Forward s^{-1}
1	$Xa + VII \rightarrow Xa + VIIa$	$k_1 = 1.3 \times 10^7$		
2	$Ila + VII \rightarrow Ila + VIIa$	$k_2 = 2.3 \times 10^4$		
3	$II + Xa \rightarrow Ila + Xa$	$k_3 = 7.5 \times 10^3$		
4	$Ila + VIII \rightarrow Ila + VIIIa$	$k_4 = 2.0 \times 10^7$		
5	$VIIIa + IXa \leftrightarrow IXa + VIIIa$	$k_5 = 1.0 \times 10^7$	$k_9 = 8.2$	
6	$IXa = VIIIa + X \leftrightarrow IXa = VIIIa = X \rightarrow IXa = VIIIa + Xa$	$k_6 = 5.0 \times 10^{-3}$	$k_8 = 1.0 \times 10^{-3}$	$k_{11} = 2.2 \times 10^4$
7	$VIIIa \leftrightarrow VIIIa_1 \cdot L + VIIIa_2$	$k_7 = 1.0 \times 10^8$	$k_{10} = 6.0 \times 10^{-3}$	
8	$IXa = VIIIa = X \rightarrow VIIIa_1 \cdot L + VIIIa_2 + X + IXa$		$k_{12} = 1.0 \times 10^{-3}$	
9	$IXa = VIIIa \rightarrow VIIIa_1 \cdot L + VIIIa_2 + IXa$		$k_{13} = 1.0 \times 10^{-3}$	
10	$Ila + V \rightarrow Ila + Va$	$k_{14} = 2.0 \times 10^7$		
11	$Xa + Va \leftrightarrow Xa + Va$	$k_{15} = 4.0 \times 10^8$	$k_{16} = 0.2$	
12	$Xa = Va + II \leftrightarrow Xa = Va = II \rightarrow Xa = Va + mIIa$	$k_{17} = 1.0 \times 10^8$	$k_{18} = 103$	$k_{19} = 63.5$
13	$Xa = Va + mIIa \rightarrow Xa = Va + Ila$	$k_{20} = 1.5 \times 10^7$		
14	$Xa + TFP1 \rightarrow Xa = TFP1$	$k_{21} = 9.0 \times 10^5$		
15	$Xa + ATIII \rightarrow Xa = ATIII$	$k_{23} = 1.5 \times 10^3$		
16	$mIIa + ATIII \rightarrow mIIa = ATIII$	$k_{24} = 7.1 \times 10^3$		
17	$IXa + ATIII \rightarrow IXa = ATIII$	$k_{25} = 4.9 \times 10^2$		
18	$Ila + ATIII \rightarrow Ila = ATIII$	$k_{26} = 7.1 \times 10^3$		
19	$BocVPRMCA + Ila \rightarrow BocVPRMCA = Ila$	$k_{27} = 1.0 \times 10^8$		
20	$XII \rightarrow XIIa$	$k_{30} = 5.0 \times 10^{-3}$	$k_{28} = 6.1 \times 10^3$	$k_{29} = 53.8$
21	$XIIa + XII \leftrightarrow XIIa = XII \rightarrow XIIa + XIIIa$	$k_{31} = 1 \times 10^8$		
22	$XIIa + PK \leftrightarrow XIIa = PK \rightarrow XIIa + K$	$k_{34} = 1 \times 10^8$	$k_{32} = 750$	$k_{33} = 3.3 \times 10^{-2}$
23	$XII + K \leftrightarrow XII = K \rightarrow XIIa + K$	$k_{37} = 1 \times 10^8$	$k_{35} = 3.6 \times 10^3$	$k_{36} = 40$
24	$PK + K \rightarrow K + K$	$k_{40} = 2.7 \times 10^4$	$k_{38} = 45.3$	$k_{39} = 5.7$
25	$K \rightarrow K_{inh}$			$k_{41} = 1.1 \times 10^{-2}$
26	$XIIa + C1_{inh} \rightarrow XIIa = C1_{inh}$	$k_{42} = 3.6 \times 10^3$		
27	$XIIa + ATIII \rightarrow XIIa = ATIII$	$k_{43} = 21.6$		
28	$XI + Ila \leftrightarrow XI = Ila \rightarrow XIa + Ila$	$k_{44} = 1 \times 10^8$	$k_{45} = 5$	$k_{46} = 1.3 \times 10^{-4}$
29	$XIIa + XI \leftrightarrow XIIa = XI \rightarrow XIIa + XIa$	$k_{47} = 1.0 \times 10^9$	$k_{48} = 200$	$k_{49} = 5.7 \times 10^{-3}$
30	$XIa + XI \rightarrow XIa + XIa$	$k_{50} = 3.19 \times 10^6$		
31	$XIa + ATIII \rightarrow XIa = ATIII$	$k_{51} = 3.2 \times 10^2$		
32	$XIa + C1_{inh} \rightarrow XIa = C1_{inh}$	$k_{52} = 1.8 \times 10^3$		
33	$XIa + \alpha_1 ATIII \rightarrow XIa = \alpha_1 ATIII$	$k_{53} = 1.0 \times 10^2$		
34	$XIa + \alpha_2 ATIII \rightarrow XIa = \alpha_2 ATIII$	$k_{54} = 4.3 \times 10^3$		
35	$XIa + IX \leftrightarrow XIa = IX \rightarrow XIa + IXa$	$k_{55} = 1.0 \times 10^8$	$k_{56} = 41.0$	$k_{57} = 7.7$
36	$IXa + X \leftrightarrow IXa = X \rightarrow IXa + Xa$	$k_{58} = 1.0 \times 10^8$	$k_{59} = 0.64$	$k_{60} = 7.0 \times 10^{-4}$
37	$Xa + VIII \leftrightarrow Xa = VIII \rightarrow Xa + VIIIa$	$k_{61} = 1.0 \times 10^8$	$k_{62} = 2.1$	$k_{63} = 0.023$

Table 3.1 Kinetic parameters and coagulation reactions used in the simulations. The model of Chatterjee et al. [30] was adapted to the experimental conditions detailed in Section 3.2.1.

The TGA experimental data generated in our laboratory was use as a test case for the model of Chatterjee et al. [30] with some modifications related to our experimental setup. The inhibition by corn trypsin inhibitor was suppressed since it was not used. The initial trigger reaction activation of factor *XII* (reaction 20) was modified, the original value in [30] is fitted using their specific experimental. Fibrin related reactions were not included in the model to reduce the computational cost of the model when performing the sensitivity analysis. The reactions of recombinant factor *VII* activation by thrombin (*II_a*) were not used since it is not present on PPP. Note that these modifications drastically improve the numerical-experimental comparison in the thrombin generation test cases considered in this study.

A system of ordinary differential equations (ODE) can be written from the biochemical reactions of the kinetic model (Table 3.1). The ODE system writes:

$$\frac{dC_i}{dt} = R_i \quad (3.1)$$

where C_i is the concentration of species i and R_i is the source term which is obtained by applying the law of mass action to the coagulation reactions of Table 3.1. As an example the source term of Kininogen K is developed as:

$$\begin{aligned} \frac{dC_K}{dt} = & -k_{41}C_K - k_{37}C_{XII}C_K + (k_{38} + k_{39})C_{XII=K} \\ & + 2k_{40}C_{PK}C_K + k_{36}C_{XII_a=PK} \end{aligned} \quad (3.2)$$

The solution of the system is computed using an integration Runge-Kutta scheme of the 4th order. This numerical scheme was implemented in the in-house CFD solver YALES2BIO¹. YALES2BIO has already been used in coagulation problems by Méndez Rojano et al. [77] and other cardiovascular flows in micro [105, 68] and macro [34, 131, 106] scale applications. Table 3.2 shows the initial concentrations used in the numerical simulations which correspond to the initial conditions of the thrombin generation assay.

In addition to the concentrations of species, which are patient-specific, the coagulation model is governed by 63 reaction rates (see Table 3.1). The reaction rates are derived from reactions observed under experimental conditions of saturating phospholipid concentration. Most of the kinetics models are build upon reaction rate values reported in literature [62, 130, 129]. Additional fitting is in general required due to non-physiological conditions in which some parameters are derived or extensively modified proteins which are used to obtain the parameter

¹<http://www.math.univ-montp2.fr/~yales2bio/>

value [57]. For this reason, reported values in different kinetic models sometimes present large variation. For instance, in factor *XI* activation reaction rates can be found in literature with a difference up to 5 orders of magnitude as highlighted by Belyaev et al. [15].

Factor	Initial Condition [nM]
<i>VII</i>	6.67
<i>VII_a</i>	0.667
<i>X</i>	106.67
<i>IX</i>	6.0
<i>II</i>	933.0
<i>VIII</i>	0.4667
<i>V</i>	13.33
<i>TFPI</i>	1.667
<i>ATIII</i>	2267.0
<i>XII</i>	226.7
<i>PK</i>	300.0
<i>C1_{inh}</i>	1667.0
<i>XI</i>	206.7
α_1ATIII	30000.0
α_2ATIII	667.0
BocVPRMCA	6670.0

Table 3.2 Factors concentrations based on TGA (concentrations are calculated after sample mixing with fluorescent reagent and using the values reported by Cryopep, Montpellier France) used as initial conditions in the numerical simulations.

Figure 3.1 shows the numerical and experimental data. The numerical set up here presented was used as a nominal reference for the sensitivity analysis. A reasonable agreement between the experimental TGA and the kinetic model of Chatterjee et al. [30] was obtained.

3.2.3 Morris Sensitivity Analysis

A full sensitivity analysis across the full range of parameter variations is prohibitive for this model, due to the large number of parameters and the large variation on the parameters values. As a consequence, a more simple screening technique is preferred, as commented in Danforth et al. [36]. The screening method of Morris [82] allows a fast exploration of a model through the discretization of the input parameters. This type of method is well suited to models with many parameters and a good compromise between accuracy and efficacy has been reported [59]. The general idea of the Morris analysis is to calculate a number of

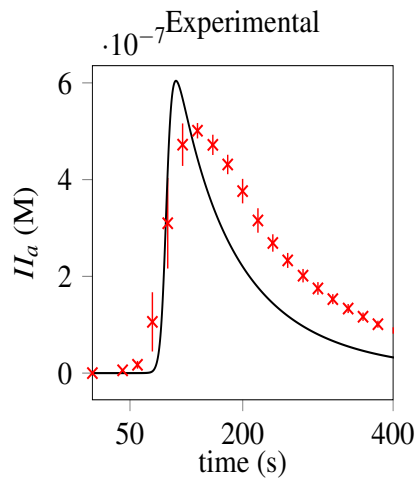


Fig. 3.1 Experimental results of thrombin generation assay (left) and numerical simulation using the kinetic scheme of Table 3.1 with the initial conditions of Table 3.2.

elementary effects for each input parameters and to compute basic statistics to identify the most sensitive parameters. In order to compute the elementary effects a discrete grid is built on the input variables and explored with an efficient sampling technique. In the current work, the python module SALIB² that follows the optimized version of the Morris method by Campolongo et al. [25] was used. The practical steps that were performed to conduct the analysis using the model of Chatterjee et al. [30] are the following:

1. Choice of discrete grid and sampling: a discrete grid on the $p = 63$ input variables is built with l probability levels uniformly distributed between $[0, 1]$. In this analysis 10 levels of discretization were used. Inside the input domain a number of trajectories r has to be determined in order to cover the input parameters space in an efficient manner. In the original method of Morris [82], the trajectories starting point is chosen randomly, then consecutive one-at-a-time increments are performed in the discrete grid with a random direction. To perform an optimal coverage of the input space, the optimized strategy of Campolongo et al. [25] was preferred in this analysis. In the optimal strategy, the dispersion of the starting points is maximized through the generation of several Morris trajectories (in this case $r_{max} = 500$). Then the most spread optimal trajectories are kept, for this case $r = 10$. The total number of experiments is then defined by $M = r(p + 1)$ thus, for the current model, $M = 640$ TGA simulations were required.

²<http://salib.readthedocs.io/en/latest/api.html>

- Mapping of parameters to actual distribution: once the sampling is performed a Design of Experiment (DoE) matrix with parameters between 0 and 1 is obtained. A quantile function is applied to transform the parameters to their actual values. This is a common practice in several screening strategies [98]. In our analysis, a log-uniform probability distribution is used for all the input parameters. This choice was motivated by the large parameter variations reported in the literature [56]. In addition, the actual distribution for each reaction rate is not available in literature. The quantile function used writes

$$Q(z_i) = c_{inf,i} \left(\frac{c_{sup,i}}{c_{inf,i}} \right)^{z_i} \quad (3.3)$$

where $[c_{inf,i}; c_{sup,i}]$ is the distribution support and z_i is the sampled value of the i parameter (between $[0,1]$). To guarantee that the mean μ_i of the sampled parameters coincides with the nominal input value k_i , the superior and the inferior support values must be estimated. To do so, the support ratio $\beta = \frac{c_{sup,i}}{c_{inf,i}}$ is introduced in the log-uniform mean expression $\mu_i = (c_{sup,i} - c_{inf,i}) / (\log(c_{sup,i}) - \log(c_{inf,i}))$. Imposing $\mu_i = k_i$ then leads to $c_{inf,i} = \frac{k_i \log(\beta)}{\beta - 1}$ and $c_{sup,i} = \beta c_{inf,i}$. In the current analysis, β was set equal to 100 which translates in parameters variation of about 4.5% – 450% of each parameter nominal values. Two trajectories in the (k_3, k_7) plane are displayed in Figure 3.2 to illustrate the method.

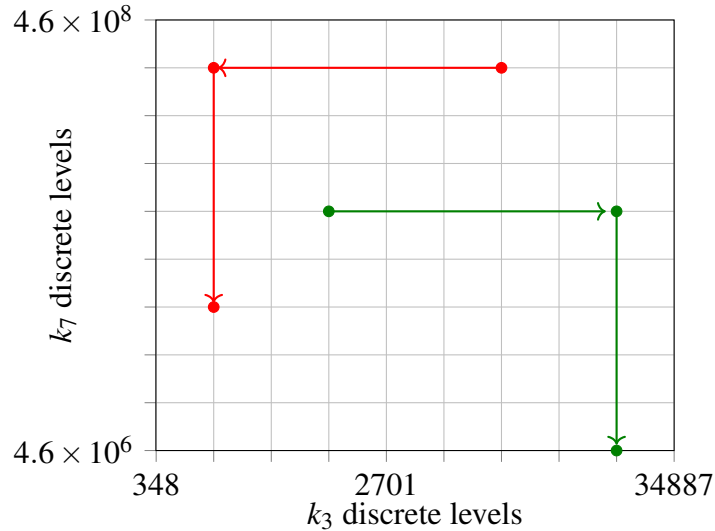


Fig. 3.2 2D parameter grid, the levels are mapped using the log uniform distribution. Two trajectories are shown as an illustration of the OAT random advancement.

3. Solution with YALES2BIO and Quantities of Interest (QoI) post-processing: The DoE simulations were performed using YALES2BIO with a fixed time step of $\Delta t = 1 \times 10^{-4}$ s. Post-processing included the extraction of the QoI from the thrombin formation curve. The QoI used in the sensibility analysis are shown in Fig. 3.3. The five QoI are:

- (a) $t_{(II_a=10.0nM)} \equiv t_{lag}$: the instant at which the thrombin concentration reaches 10 nM,
- (b) the maximum value of thrombin concentration $max(II_a)$,
- (c) the ascending slope m_1 defined from the lag point ($t_{lag}, II_a = 10.0nM$) and the maximum peak point ($t_{max}, max(II_a)$),
- (d) the descending slope m_2 defined with the maximum peak point ($t_{max}, max(II_a)$) and the descending point at ($t_d, II_a = 10$ nM) where t_d is the instant at which the concentration of thrombin falls bellow 10 nM,
- (e) endogenous thrombin potential (ETP) which stands for the area under the curve representing the total thrombin produced.

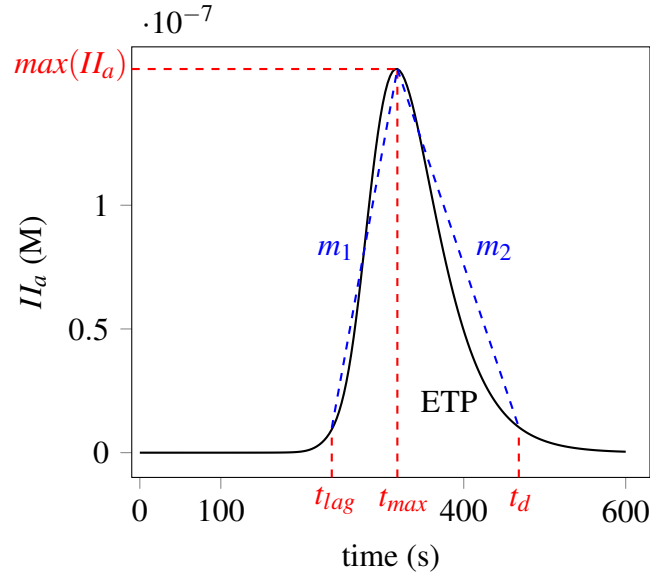


Fig. 3.3 Variables used in the sensibility analysis: t_{lag} , $max(II_a)$, m_1 , m_2 , ETP.

4. Elementary effects and sensitivity indices: the OAT incremental ratios allow to compute elementary effects of each parameter following Campolongo et al. [25]:

$$E_j^i = \frac{f(X_j^i + \delta_i) - f(X_j^i)}{\delta_i} \quad (3.4)$$

where X is the input parameter, j is the index of the input parameter, i stands for the repetition, δ_i is the variation value and the function f represents any of the five QoI from the thrombin generation curve. Two sensitivity coefficients are calculated [25]:

- $\mu_j^* = \frac{1}{r} \sum_{i=1}^r |E_j^i|$ is the mean of the absolute value of the elementary effects
- $\sigma_j = \sqrt{\frac{1}{r} \sum_{i=1}^r \left(E_j^i - \frac{1}{r} \sum_{i=1}^r E_j^i\right)^2}$ is the standard deviation of the elementary effects.

From the sensitivity indices distribution a quick identification of three different groups of parameters can be done depending on their impact on the QoI:

- parameters with little or no effect (low μ_j^* and σ_j),
- parameters with a strong linear dependency or an additive effect (large μ_j^*),
- parameters with non-linear and/or interaction effects (large σ_j),

With this classification the most sensitive parameters can be identified. In some cases, the sensitivity analysis can identify predominant reactions and contribute to reduce the complexity of the models, as discussed in Section 3.4.

3.2.4 A reduced model of coagulation initiated by contact activation

Wagenvoord et al. [116] proposed a minimal reaction mechanism of thrombin formation triggered by factor VII_a . The reduced model included reactions of the extrinsic and common pathways and can thus be applied in cases where TF is the initial mechanism. In this model, 14 parameters including 9 kinetic constants and 5 initial concentrations of coagulation factors must be optimized in order to correctly reproduce experimental trends of thrombin formation. It is worth mentioning that in reduced kinetic models, the species maybe fictive species and the optimal initial concentrations of factors are not representative of the actual concentrations in blood plasma. However, these models have been successful to reproduce thrombin formation triggered by the extrinsic pathway. In the current work a reduced model for thrombin production initiated by contact activation is proposed. The minimal reaction mechanisms consist of 5 reactions that are triggered by activation of factor XII , the reactions are listed on Table. 4.6. The model includes 8 reaction rates and 8 chemical species. The amplification and propagation phases are performed by the auto-activation loop through the activation of factor V_a , this mechanism also appearing in the model of Wagenvoord et al. [116]. Finally,

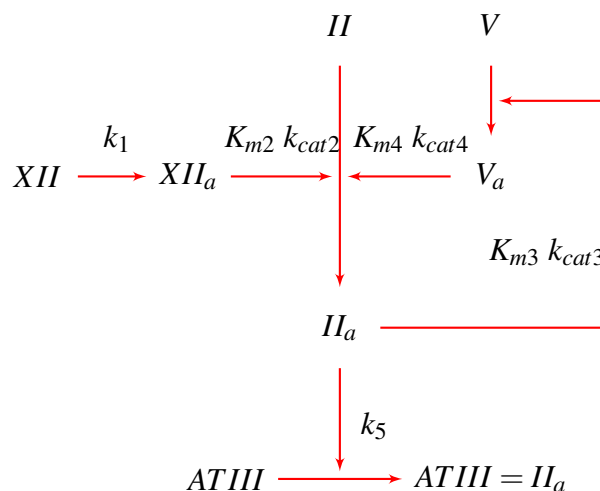


Fig. 3.4 Reduced model for thrombin generation triggered by the contact activation system. The notation K_{mi} , k_{cati} is used for reaction following Michaelis–Menten kinetics while k_i are first order reactions.

inhibition of thrombin is due to the activity of $ATIII$. Figure 3.4 shows a schematic of the model with the corresponding kinetic parameters.

#	Reaction	K_m M	k_{cat} s ⁻¹	k s ⁻¹
1	$XII \rightarrow XII_a$			k_1
2	$XII_a + II \rightarrow II_a + XII_a$	K_{m2}	k_{cat2}	
3	$II_a + V \rightarrow II_a + V_a$	K_{m3}	k_{cat3}	
4	$V_a + II \rightarrow V_a + II_a$	K_{m4}	k_{cat4}	
5	$II_a + ATIII \rightarrow II_a = ATIII$			k_5

Table 3.3 Reduced kinetic model for the coagulation cascade showed in Fig. 3.4. Reactions 1 and 5 are first order reaction, reactions 2, 3 and 4 follow Michaelis–Menten kinetics.

The kinetic model $\dot{\mathbf{C}} = \mathcal{M}(\mathbf{C}, t)$ can be represented by a system of ordinary equations that can be solved using a classical numerical scheme. The ODE system writes:

$$\begin{bmatrix} \dot{C}_{XII} \\ \dot{C}_{XIIa} \\ \dot{C}_{II} \\ \dot{C}_{IIa} \\ \dot{C}_V \\ \dot{C}_{Va} \\ \dot{C}_{ATIII} \\ \dot{C}_{ATIII=IIa} \end{bmatrix} = \begin{bmatrix} -k_1 C_{XII} \\ k_1 C_{XII} \\ \frac{k_{cat4} C_{Va} C_{II}}{K_{m4} + C_{II}} - \frac{k_{cat2} C_{XIIa} C_{II}}{K_{m2} + C_{II}} - k_5 C_{IIa} C_{ATIII} \\ \frac{k_{cat2} C_{XIIa} C_{II}}{K_{m2} + C_{II}} + \frac{k_{cat4} C_{Va} C_{II}}{K_{m4} + C_{II}} - k_5 C_{IIa} C_{ATIII} \\ \frac{k_{cat3} C_{IIa} C_V}{K_{m3} + C_V} \\ \frac{k_{cat3} C_{IIa} C_V}{K_{m3} + C_V} \\ -k_5 C_{IIa} C_{ATIII} \\ k_5 C_{IIa} C_{ATIII} \end{bmatrix}$$

Parameter values should be optimized to compute thrombin formation with a reasonable agreement with reference data. Here we use the experimental data generated by TGA triggered by contact activation.

3.2.5 Bayesian parameter inference

The proposed reduced-order coagulation model depends on a set of parameters which need to be calibrated. The idea behind this parametric calibration is to adjust the unknown parameters in order to lower the discrepancy between the numerical prediction and some indirect and imperfect (experimental) observations of the system. This is a computational burden because the model is nonlinear and brings in unknown relatively high-dimensional parameter spaces. Model inversion in the presence of measurement errors must typically take advantage of some type of regularization (e.g., Tikhonov regularization) in order to recover the existence and uniqueness of solutions or a robust optimization method [12]. A potentially more natural setting is the Bayesian statistics. The Bayesian statistical framework can be explained as a systematic use of probability dedicated to decision-making when using a model with uncertain parameters. It is advantageous because it allows the specification of a prior distribution which expresses probabilistically what is known about the parameters before observing the data. In this study, a Bayesian inference technique is used to obtain the optimal parameters

involved in the model that allow to capture the thrombin formation curve. The parameters to be inferred are the 8 reactions rate and the initial concentrations of species XII , V and $ATIII$, i.e. a total of 11 quantities.

This approach is used in inverse problems and relies on posterior sampling techniques. Thus, a prior distribution of the parameters to be calibrated is necessary, so that the estimation process delivers a probabilistic characterization of the parameters. In this work, a Markov-Chain Monte-Carlo algorithm is used considering the input parameters as random quantities that are sampled according to the posterior distribution.

A significant amount of literature exists on the Bayesian inference method. In the following, the work of Xiu [122], Birolleau et al. [19], Andrieu et al. [9] is used to present the steps of the parameter inference. In the Bayesian approach, a vector of unknown parameters is considered

$$\mathbf{k} = (k_1, K_{m2}, k_{cat2}, K_{m3}, k_{cat3}, K_{m4}, k_{cat4}, k_5, XII_{init}, V_{init}, ATIII_{init}). \quad (3.5)$$

The parameters are treated as random variables with a prior density distribution $\pi_{\text{prior}}(\mathbf{k})$. In the current inference procedure, log-uniform distributions were assumed as prior distributions for all the parameters. Observations of the QoI are necessary to perform the inference process. In this application, the observed variables $\mathbf{d} \in \mathbb{R}^{n_d}$ are the experimental measurements of the thrombin generation assay or the numerical results of the detailed kinetic model at n_t discrete time instants $C_{II_a}(n_t)$.

The Bayesian formula, involving conditional probabilities, can be applied as in Birolleau et al. [19] to obtain the parameters posterior distribution considering the reduced model, the prior parameters distribution and the experimental observations

$$\pi_{\text{post}}(\mathbf{k}|\mathbf{d}) \propto \pi_\ell(\mathbf{d}|\mathbf{k})\pi_{\text{prior}}(\mathbf{k}), \quad (3.6)$$

where $\pi_\ell(\mathbf{d}|\mathbf{k})$ is the likelihood function that combines the experimental data with the forward model and

$\pi_{\text{post}}(\mathbf{k}|\mathbf{d})$ the desired posterior density of the parameters. The initial concentration of prothrombin is not inferred, thus the physiological condition of pool plasma is used in the reduced kinetic model, $II = 933.0$ nM. Following Xiu [122] assuming additive measurement

noise $\boldsymbol{\varepsilon}$ and mutually independent random variables, one can write:

$$\boldsymbol{d} = \mathcal{G}(\boldsymbol{C}) + \boldsymbol{\varepsilon} = \mathcal{G}(\mathcal{M}(\boldsymbol{k}, t)) + \boldsymbol{\varepsilon}, \quad (3.7)$$

where $\mathcal{M} : \mathbb{R}^{n_k} \times \mathbb{R}^{n_t} \rightarrow \mathbb{R}^{n_c \times n_t}$ is the deterministic forward model, $\mathcal{G} : \mathbb{R}^{n_c \times n_t} \rightarrow \mathbb{R}^{n_d}$ is an observation operator that relates the model solution \boldsymbol{C} with the reference discrete concentration of thrombin \boldsymbol{d} and $\pi_{\boldsymbol{\varepsilon}}$ is the prescribed noise distribution of $\boldsymbol{\varepsilon}$. More specifically, in our case, the likelihood function can be expressed as follows:

$$\pi_{\ell}(\boldsymbol{d}|\boldsymbol{k}) = \prod_{i=1}^{n_t} \pi_{\boldsymbol{\varepsilon}} \left(d^{(i)} - \mathcal{G}(\mathcal{M}(\boldsymbol{k}, t^{(i)})) \right). \quad (3.8)$$

The likelihood function contains a stochastic source term that must encompass the response of the deterministic kinetic model over the support of $\pi_{\text{post}}(\boldsymbol{k}|\boldsymbol{d})$. Since the posterior distribution does not have in this case an analytic closed expression, posterior moments, expectations or maximum a posteriori values must be estimated via sampling methods such as Markov chain Monte Carlo (MCMC) as explained in Andrieu et al. [9]. The posterior sampling of the parameters is handled thanks to a standard Metropolis-Hastings scheme [53]. In our case, it requires many model realizations (about twenty thousand), which is not penalizing as the reduced-order model is not computationally demanding.

3.3 Results

3.3.1 Sensitivity Analysis of the full coagulation model

The first aspect of interest is the robustness of the detailed coagulation model of Chatterjee et al. [30] initiated by contact activation. Figure 3.5 shows the results of the sensitivity analysis using the screening Morris method for each quantity of interest. The basic statistics of the elementary effects σ_j and μ_j^* are computed using the thrombin concentration of the 640 simulations. An arbitrary threshold of 30% of the largest value of both sensitivity indices is used to keep apart the sensitive parameters.

The important parameters identified for the time lag t_{lag} (Fig. 3.5a) belong to the intrinsic pathway; activation of factors IX (reaction 35) and XI (reaction 29) have large impacts on t_{lag} .

The parameters relevant to $\max(II_a)$ are reactions rates involved in the activation of factor II (Fig. 3.5b). In addition, thrombin inhibition due to $ATIII$ presents a large influence on the maximum value of thrombin. The ascending slope m_1 (Fig. 3.5c) shows a large influence to reaction rates involved in reaction 12 which is formation of mII_a by the Prothrombinase complex. Furthermore, reaction rates involved in the intrinsic pathway, activation of factors, XI_a , IX , X and $VIII$, showed to be important for m_1 for instance.

The descending slope of thrombin evolution m_2 (Fig. 3.5d) is mostly influenced by the thrombin inhibition activity of $ATIII$ and by the production of mII_A and II_a in reactions 18 and 20, respectively.

Finally, the results on ETP (Fig. 3.5e) show that the most influential parameters are involved in the inhibition activity of $ATIII$ by means of complex formation with II_a and mII_a . Reaction rate k_{20} which is involved in the conversion of mII_a into II_a is also relevant to ETP. The histogram shows that the conversion of mII_a into II_a determined by k_{20} is relevant to all the QoI. In a similar way, inhibition activity by $ATIII$ due to parameter k_{26} is important for 4 QoI, excluding only t_{lag} . Six reaction rates are sensitive to at least three QoI, the majority of these parameters are involved directly in the production of II_a with the exclusion of parameter k_{60} which is involved in the activation of factor X by IX_a .

The parameters identified by the sensitivity analysis are consistent with the nature of the QoI. It is important to note that the results were verified using a second strategy for global sensitivity analysis. To do so, the Sobol indices using a Stroud quadrature of the level $P = 2$ were calculated as in [108]. This sampling method requires few points to approximate the central moments of the joint probability distribution. In this case, 126 simulations were performed. Sobol indices are a variance-based method of global sensitivity analysis that can identify the parameters that cause large variation on the output of a given model. Figure 3.6 shows the Sobol coefficients of the 63 parameters for t_{lag} . The parameters marked with a **x** are the parameters with with large variance. A remarkable consistency with the Morris method is observed for all the QoI (results for the 4 remaining QoI are not shown).

3.3.2 Reduced model for thrombin generation

Whatever the confidence we have in a coagulation model, it can only be used in CFD if its computational cost remains tractable. As a result, model reduction is particularly useful to build coagulation models with a limited number of species. Of course, such models involve

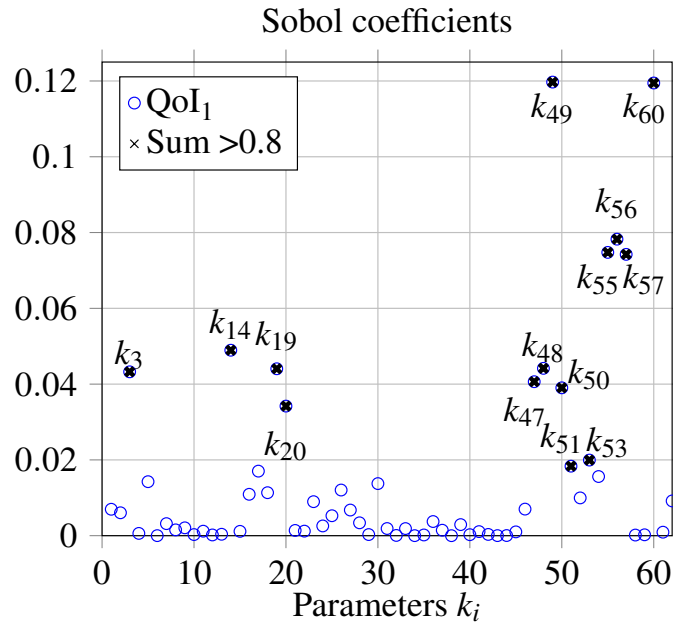


Fig. 3.6 Sobol coefficients of the 63 parameters for t_{lag} calculated with 126 Stroud data points, with Legendre Polynomials. Coefficients marked with \times are responsible for 80% of the output variance

new parameters whose values need to be determined using reference data sets.

Eight thrombin generation assays initiated by contact activation were conducted to obtain the data sets relevant to thrombin. The mean of these thrombin formation curves was used to perform the Bayesian inference assuming a 4 % of observation uncertainty. Optimal parameters obtained after 20,000 MCMC (Metropolis-Hastings sampling algorithm) iterations are listed in Table 3.4. Figure 3.7 shows the experimental data and the numerical results using the Bayesian optimal parameters in the reduced coagulation model. Numerical results using the Bayesian optimal parameters aligned well with TGA experimental data.

To evaluate the predictive capabilities of the proposed reduced model, the initial condition of factor II was varied. Figure 3.8 shows both the numerical and TGA results for three prothrombin concentrations. The three cases correspond to the physiological condition $C_{II} = 933.0$ nM, 50% and 15% of the physiological values, respectively. It can be noticed that both cases at low prothrombin concentrations are shifted with longer lag times than the TGA data. In addition, the amplitude of the II_a curves is, in both cases, smaller than the experimental results. However, the numerical results reproduce fairly well the trends of thrombin formation, demonstrating the good predictive capabilities of the reduced model

#	k	<i>optimal</i>
1	k_1	6.4×10^{-3}
2	k_{cat2}	8.21
3	k_{m2}	8.95×10^{-9}
4	k_{cat3}	3.5×10^{-3}
5	k_{m3}	2.0×10^{-9}
6	k_{cat4}	4.98
7	k_{m4}	8.25×10^{-7}
8	k_5	7.79×10^{-3}
9	C_{XII}	9.36×10^{-11}
11	C_V	6.2×10^{-9}
12	C_{ATIII}	1.665×10^{-6}

Table 3.4 Optimal parameters obtained from Bayesian inference; the initial concentration of prothrombin $C_{II} = 933.0$ nM is not inferred.

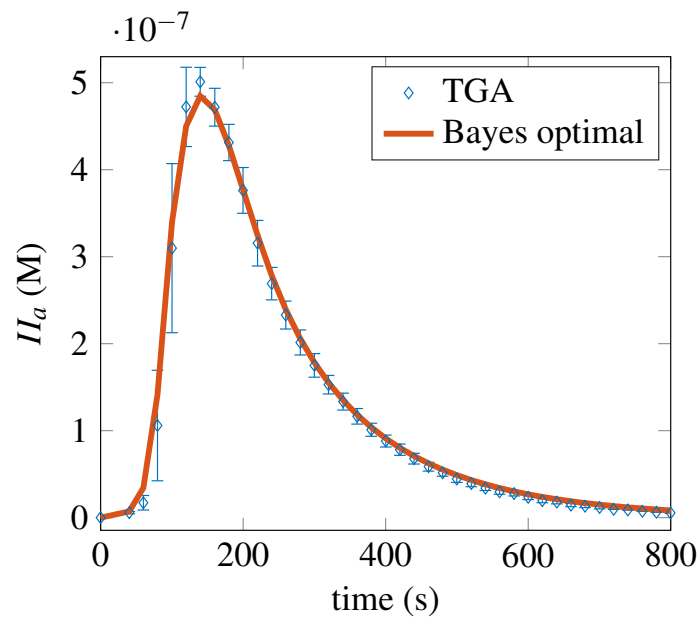


Fig. 3.7 Mean of the eight TGA data sets for physiological data and numerical thrombin formation using the reduced model (Fig. 3.4) with optimal parameters from Bayesian inference. The error bars represent the variance of the TGA data sets. The optimal parameters were obtained after 20000 MCMC iterations.

using the Bayesian optimal parameters.

The inference process was also performed using as a reference the numerical data from the detailed model of Chatterjee et al. [30] assuming an uncertainty on thrombin concentration of 4 %. Table 3.5 shows the values of the inferred parameters. This approach can be

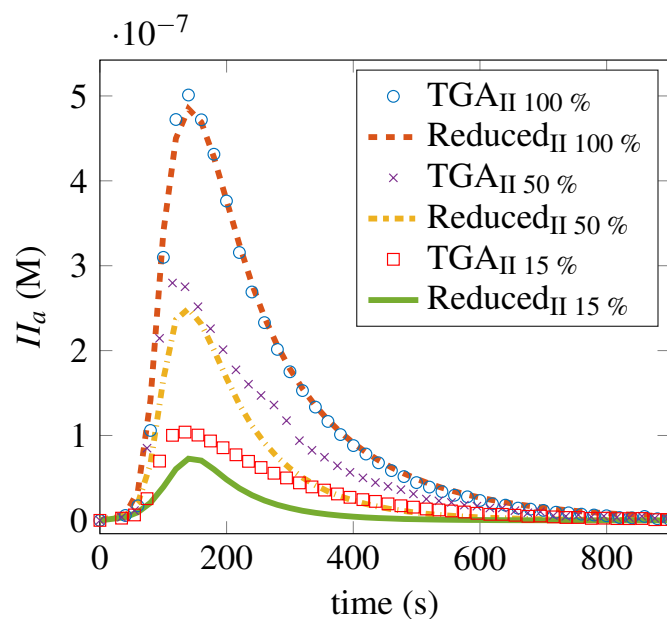


Fig. 3.8 Experimental TGA and numerical data using the reduced model with optimal parameters of Table 3.4 for a range of factor II initial concentrations, 100% =physiological PPP concentration, 50%, 15%)

applied to more general cases in which the experimental conditions differ from the TGA samples previously presented.

#	k	<i>optimal</i>
1	k_1	1.2×10^{-3}
2	k_{cat_2}	0.28
3	k_{m_2}	3.72×10^{-7}
4	k_{cat_3}	7.7×10^{-3}
5	k_{m_3}	6.4×10^{-10}
6	k_{cat_4}	7.01
7	k_{m_4}	9.54×10^{-7}
8	k_5	9.88×10^3
9	C_{XII}	7.91×10^{-11}
11	C_V	1.8×10^{-8}
12	C_{ATIII}	1.977×10^{-6}

Table 3.5 Optimal parameters obtained from Bayesian inference using the numerical data of the detailed model of Chatterjee et al. [30]. The initial concentration of prothrombin $C_{II} = 933.0$ nM is not inferred.

Figure 3.9 shows the thrombin generation curves using the inferred parameters of Table 3.5. A lag time between the model of Chatterjee et al. and the reduced model is observed for the case of 15% prothrombin initial concentration. A good trend is however observed in the reference and 50% cases.

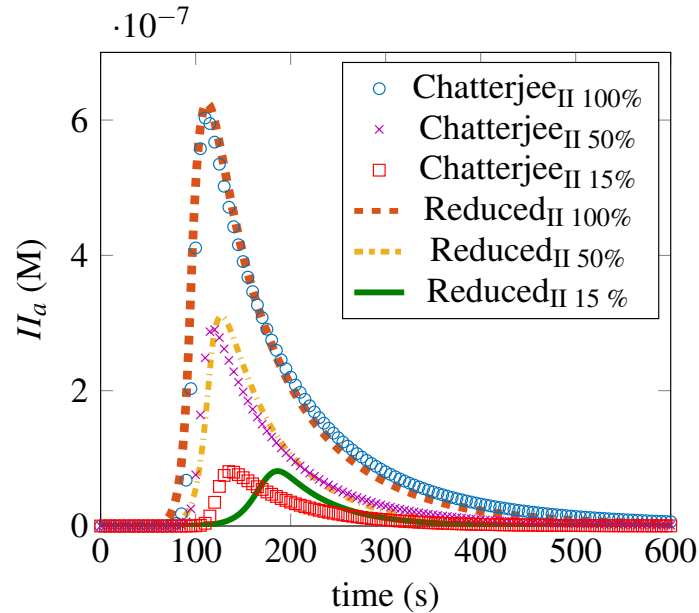


Fig. 3.9 Numerical results of the detailed model of Chatterjee et al. [30] and numerical data using the reduced model with optimal parameters of Table 3.5 for a range of factor II initial concentrations, 100% =physiological PPP concentration, 50%, 15%)

3.4 Discussion

In this work, two kinetic models of the coagulation cascade initiated by contact activation with a different level of complexity are used: a full reference model from the literature and a reduced model introduced here for the first time. First, the Morris [82] method for sensitivity analysis is applied to the existing detailed model of the coagulation cascade initiated by the contact activation system. This screening technique allowed the identification of the parameters that have a significant impact on the model QoI's. The kinetic rates that had the largest impact on the time before the reactions take up t_{lag} are involved in the intrinsic coagulation pathway ($k_{57}, k_{55}, k_{60}, k_{56}, k_{48}, k_{49}$). Interestingly, the reaction rate k_{30} which is implicated in the contact activation of factor XII does not have a significant effect on t_{lag} , thus suggesting that its role is only to trigger the cascade of reactions. This results are consistent with the numerical results of Méndez Rojano et al. [77] in which a parametric

study on the activation rate of factor XII_a showed a limited impact on thrombin formation. This effect may explain the difficulties of developing a full non-thrombotic material since reducing the contact activation rate does not help to reduce the thrombin concentrations levels.

The ascending slope m_1 is particularly sensitive to k_{50} which is involved in the auto-activation of factor XI . In addition parameters k_{61} and k_{63} participating in the formation of thrombin and activation of factor $VIII$ showed large impact on this QoI. For the other quantities $max(II_a)$, m_2 and ETP, the reaction rates that were identified correspond to reactions that are directly involved in the production of thrombin or the inhibition activity of $ATIII$ (k_{26} , k_{20} , k_{23} , k_{24} , k_{18} , k_{19}).

To verify the results, another sensitivity analysis using the Stroud sampling quadrature and the Sobol indices was performed and the results were qualitatively confirmed for all the QoI's. In the histogram showed in Fig. 3.5, parameter k_{20} was identified to be important for all the QoI. Reaction rate k_{26} is sensitive to four QoI except for t_{lag} . These findings align well with the sensitivity study of Danforth et al. [36] on the coagulation model triggered by $TF = VII_a$. Danforth and coworkers found that the thrombin formation levels were sensitive to variations on reaction rates k_{26} and k_{20} . Many reaction rates identified by Danforth participate in the initiation phase of the extrinsic pathway. In the current work reactions rates k_{57} , k_{56} and k_{55} participating in the intrinsic system have a considerable impact on the QoI's t_{lag} and m_1 . Finally, six reactions rates were found to be important to three output variables, k_{18} , k_{19} , k_{24} which are involved in the production and inhibition of mII_a and k_{60} which participates in the activation of factor X by IX_a . A better experimental characterization of these six reactions may lead to an improvement in the robustness of the model.

As pointed out by Ngoepe et al. [87] thrombosis models should be sophisticated enough to provide precious clinical information with a reasonable computational cost. To tackle this challenge in the context of device-associated thrombosis, a reduced model for thrombin generation triggered by contact activation of factor XII is proposed. This model allows for the characterization of the patient thrombin formation profile with a minimal reaction mechanisms. The reduced model was constructed based on previous reduction approaches [116] and by substituting the extrinsic pathway with the contact activation system. The sensitivity results also guided the construction of the reduced model. For instance, the sensitivity analysis showed that formation of thrombin and meizothrombin by factor V_a had an important role by means of parameters k_{18} , k_{19} and k_{20} . In addition, inhibition activity of $ATIII$ showed to be relevant through parameters k_{26} and k_{24} . Thus, these two mechanisms

were incorporated with the minimum number of reactions in the reduced model. Finally, in order to compute thrombin evolution, the 11 parameters involved in the model (kinetic rates and initial constants) have to be calibrated. A Bayesian inference framework with a MCMC sampling method was used to infer the optimal parameters using the concentration of thrombin in time as reference data from both the TGA and the detailed model of Chatterjee et al. [30]. The set of parameters found by the Bayesian inference method could reproduce the experimental TGA trend when the initial concentration of factor *II* was decreased to 50 and 15 % from its physiological value. A supplemental set of parameter values was inferred using the detailed kinetic model of Chatterjee et al. The set of parameters aligned well with the trend presented by Chatterjee's model; this set of parameters may be used in general purpose CFD computations in which the conditions of the case are not the same as in our experimental configuration. Using such a reduced kinetic model in hemodynamic computations lowers the computational cost of chemical species transport by almost a factor of seven.

The results contribute to improve the predicting capabilities of the model of Chatterjee et al. [30]. To the best of our knowledge, this is the first time that a minimal reaction mechanism triggered by the contact activation system is proposed. The reduced model combined with proper boundary conditions [77] may be particularly useful in situations in which the coagulation reactions are triggered by contact activation of factor XII.

Chapter 4

Thrombus growth and its influence on the flow

In the current chapter, the reduced kinetic model developed in Chapter 3 is included in the thrombus growth of Taylor et al. [112], which is based on platelet activity. The model of Taylor et al. was implemented in YALES2BIO and verified in the backward facing step configuration of [111]. The results show robustness issues in Taylor's model related to the background activation levels of platelets. This issue is addressed by including platelet activation due to thrombin which is produced by coagulation reactions triggered at the backward facing step wall. The reactions are triggered using the reactive boundary conditions developed in Chapter 2.

4.1 Introduction

Thrombus growth (TG) dynamics has been extensively studied in vessel injury configurations [5, 70, 126]. The models in which a detailed biochemical description is used (coagulation cascade, platelet activation and aggregation and their interactions) were only applied to simple hemodynamic configurations. These models are too sophisticated and therefore not suitable for applications in complex flow configurations such as prosthetic heart valves or aortic dissections. To overcome this challenge and develop computational cost-effective frameworks, reduced models have been developed [51, 52, 79, 88]. In general, the main goal of these models is, the identification of regions prone to thrombosis and the prediction of the thrombus evolution in time. Most reduced models dedicated to blood coated medical devices have focused on platelet activity [112, 120]. These models have an affordable computational

cost and have been used to predict thrombus formation in ventricular assist devices [121]. In this application, high shear stress are observed and thus platelet activity is the triggering thrombotic mechanism. In these approaches, the coagulation reactions triggered by the presence of the foreign surface in the blood flow [77] have not been considered. However, a model that accounts for coagulation may be capable of capturing thrombus formation in situations in which shear stress is low, and therefore platelet activity is not the driving mechanism. This can be achieved by considering coagulation reactions triggered by the contact activation system.

In the current approach, the reduced model for thrombin formation of Chapter 3 is included on the platelet-based model developed by Taylor et al. [112]. To our knowledge, only two models of thrombus growth dedicated to medical devices have been developed. In our work the model of Taylor et al. [112] was chosen over the model of Wu et al. [120] due to its simplicity and lower computational cost. First, the implementation of Taylor's platelet-based model is presented with a detailed explanation of each modeling element. The implementation is verified in the backward facing step (BFS) benchmark also used in Chapter 2. The original model of Taylor et al. is used to study the pulsatile effects in the BFS benchmark. Finally, thrombin formation initiated at the device wall is included in the model, and platelet activation by thrombin is added. Results show that accounting for thrombin formation suppressed the original model dependency to background activation levels of platelets.

4.2 Platelet-based model description and implementation

The model of Taylor et al. [112] considers three biochemical species:

- non-activated platelets (NP)
- activated platelets (AP)
- Adenosine diphosphate (ADP)

Mechanical and chemical activation mechanisms are considered in the model. In this approach, mechanical stress is related to mechanical activation. When a platelet is activated, a certain amount of ADP is released. Once a threshold concentration of ADP is reached, chemical activation takes place. As in mechanical activation, chemical activation of platelets also releases ADP and an auto-amplification loop is formed. To quantify thrombus growth, a platelet aggregation intensity is computed. A steep thrombus frontier is considered through

an aggregation threshold which defines the regions in which aggregation is sufficient to form a thrombus. Finally, the impact of the growing thrombus in the flow is modeled using a Brinkman term considering the thrombus as a porous material. The different parts of the model are explained in this section.

4.2.1 Species transport and platelet activation

The species transport is modeled through a convection-diffusion-reaction equation of the form

$$\frac{\partial C_i}{\partial t} + \nabla \cdot (C_i \mathbf{u}) = \nabla \cdot (D_i \nabla C_i) + R_i \quad (4.1)$$

where C_i and D_i are the molar concentration and diffusion coefficients respectively, an equation is considered for each species i . R_i is the source term derived from chemical and mechanical activation pathways. These pathways are modeled following Soares et al. [107] and Sorensen et al. [109] for mechanical and chemical activation respectively.

Chemical activation

Chemical activation rate is computed by a function based on ADP concentration C_{ADP} , a characteristic activation time t_{ADP} and a threshold concentration of ADP C_{ADP}^{thr} . The activation source term is switched on when C_{ADP}^{thr} is attained. This form of the chemical activation rate was originally presented by [109] and later used in [120]. The rate of chemical platelet activation (A_C) writes

$$A_C(C_{ADP}) = \begin{cases} 0 & \text{for } \frac{C_{ADP}}{C_{ADP}^{thr}} < 1, \\ \frac{C_{ADP}}{C_{ADP}^{thr} \cdot t_{ADP}} & \text{for } \frac{C_{ADP}}{C_{ADP}^{thr}} \geq 1. \end{cases} \quad (4.2)$$

Mechanical activation

Mechanical activation is computed through a simplified form of the Lagrangian power law model developed by [107]. Originally, the power law of Soares and co-workers [107] considers stress history, scalar shear rate and stress rate. In the model of Taylor et al. [112], stress history and stress rate are neglected. The power law adapted into an Eulerian framework leads to the following activation rate expression:

$$A_M(\phi_f, \tau) = (1 - \phi_f) c^{\frac{1}{\beta}} \beta \phi_f^{\frac{\beta-1}{\beta}} \tau^{\frac{\alpha}{\beta}}, \quad (4.3)$$

in which ϕ_f is the fraction of activated platelets $\phi_f = \frac{C_{AP}}{C_{AP} + C_{NP}}$. Parameters c , α and β are empirically derived from the in-vitro data sets published by [111]. The scalar shear stress τ is computed according the definition of [20]

$$\tau = \left[\frac{1}{6} \sum_{i,j=1}^3 (\sigma_{ii} - \sigma_{jj})(\sigma_{ii} - \sigma_{jj}) + \sigma_{ij}\sigma_{ij} \right]^{0.5} \quad (4.4)$$

were σ_{ij} is the viscous stress tensor. The choice of the Eulerian framework over Lagrangian approaches is based on the observations of Hansen et al. [51]. Hansen and Shadden compared both approaches in an abdominal aneurysm and found that platelet activation differed by only 1%, which is small compared to background activation of platelets. It is important to note that the Eulerian approximation is computationally cheaper than the Lagrangian framework and thus suitable for biomedical devices.

With the previous activation rates, the source term for both platelets species writes

$$R_{CAP} = -R_{CNP} = C_{NP}A_C + A_M(C_{AP} + C_{NP}) = C_{NP}(A_C + c^{\frac{1}{\beta}}\beta\phi_f^{\frac{\beta-1}{\beta}}\tau^{\frac{\alpha}{\beta}}) \quad (4.5)$$

The source term for ADP has to be corrected by the amount of ADP (λ) released in platelet activation leading to

$$R_{ADP} = \lambda R_{CAP} \quad (4.6)$$

The values of the parameters used in the model are listed in Table 4.1.

Parameter	Value
c	1.4854×10^{-7}
α	1.4854
β	1.4401
λ	3×10^{-17}
D_{CNP}	$1.58 \times 10^{-11} \text{ m}^2/\text{s}$
D_{CAP}	$1.58 \times 10^{-11} \text{ m}^2/\text{s}$
D_{ADP}	$2.37 \times 10^{-10} \text{ m}^2/\text{s}$
t_{ADP}	1 s
ADP_t	2 μM

Table 4.1 Parameters involved in the source terms and transport of species in the model of Taylor et al. [112].

4.2.2 Aggregation intensity and the impact of the thrombus in the flow

In the model of Taylor et al. [112], the framework for platelet aggregation developed by Fogelson [40] is adapted to blood-coated medical devices. A platelet aggregation intensity ε is introduced as a strategy to quantify thrombus presence and density. Then a Brinkman term as a function of ε is introduced in the momentum conservation equation to account for the growing thrombus. The equations governing the flow motion including the Brinkman term that accounts for the porous behavior inside the thrombus can be expressed as follows:

$$\nabla \cdot \mathbf{u} = 0, \quad (4.7)$$

$$\rho \left(\frac{\partial \mathbf{u}}{\partial t} + \mathbf{u} \cdot \nabla \mathbf{u} \right) = -\nabla p + \mu \nabla^2 \mathbf{u} - \mu F(\varepsilon) \mathbf{u}, \quad (4.8)$$

$$F(\varepsilon) = \begin{cases} 0 & \text{if } \varepsilon < \varepsilon_t \\ \frac{1}{k} \frac{\varepsilon/\varepsilon_t}{\varepsilon/\varepsilon_t + 1} & \text{if } \varepsilon \geq \varepsilon_t \end{cases} \quad (4.9)$$

where \mathbf{u} is the velocity field, p is the pressure field, ρ stands for the density, μ is the dynamic viscosity, k is the thrombus permeability and ε_t is a threshold value that defines the thrombus frontier. The blood was considered as a Newtonian fluid (constant viscosity) since the objective of the present study was not focused on the Non-Newtonian behavior of blood. Eq. 4.9 is the piece-wise function involved in the Brinkman term which depends on the aggregation intensity.

Thrombus deposition, growth and breakdown are controlled at the wall and in the volume by the following equation

$$\frac{\partial \varepsilon}{\partial t} = \alpha_\varepsilon P_{TSP}(\tau_w) C_{AP}^2 - \beta_\varepsilon(\tau_w) \varepsilon \quad (4.10)$$

in which α_ε is the thrombus volumetric growth rate, P_{TSP} is a weighting function defined as the thrombus susceptibility potential, β_ε is the weighting function that determines thrombus breakdown and τ_w is the scalar shear stress. The thrombus initially grows from the wall, therefore, ε is initially only computed at the wall. To quantify the aggregation intensity in the volume, a threshold value is introduced ε_t . Once ε_t is attained at one wall cell, the aggregation intensity equation is turned on in the neighbor cells. In order to have a mesh-independent growth, Eq. 4.10 is multiplied by the rate $\frac{D}{d_c}$, which is the rate of the distance between the current and the neighbor cell d_c and a characteristic mesh-size D (constant) used to normalize

the growth. The thrombus susceptibility potential, P_{TSP} is computed as follows:

$$P_{TSP}(\tau_w) = \begin{cases} 1 & \text{for } |\tau_w| < \tau_{low} \\ 1 - \left(\frac{|\tau_w|}{\tau_{high}}\right) \cdot \frac{\exp\left(\frac{|\tau_w| - \tau_{low}}{\tau_{high} - \tau_{low}}\right) - 1}{\exp(1) - 1} & \text{for } \tau_{low} < |\tau_w| < \tau_{high} \\ 0 & \text{for } |\tau_w| \geq \tau_{high} \end{cases} \quad (4.11)$$

Note that this function is used for both thrombus deposition and growth. τ_{low} and τ_{high} are the lower and higher threshold values of the scalar shear stress that determine thrombus deposition. In the range $[\tau_w = 0, \tau_w = \tau_{low}]$ the maximum deposition is achieved, $[\tau_w = \tau_{low}, \tau_w = \tau_{high}]$ is the transition range with moderate thrombus deposition, finally if $\tau_w \geq \tau_{high}$ the function is set to zero (no deposition). It should be noted that on one hand thrombus wall deposition is computed using the norm of the wall shear stress and on the other hand thrombus growth is calculated using τ as in Eq. 4.4.

The second term of Eq. 4.10 is related to thrombus breakdown. The breakdown weighting function writes

$$\beta_\varepsilon(\tau_w) = \begin{cases} 0 & \text{for } |\tau_w| < \tau_{breakdown} \\ B & \text{for } |\tau_w| > \tau_{breakdown} \end{cases} \quad (4.12)$$

where B is the thrombus breakdown rate. Thrombus breakdown takes place when the scalar shear stress is larger than a threshold value $\tau_{breakdown}$ of the scalar shear stress. It should be noted that: τ_{low} , τ_{high} , $\tau_{breakdown}$, B and α_ε are empirical derived parameters used for the evolution of the piecewise functions and the thrombus volumetric growth rate. Table 4.2 shows the parameters values used in the wall and volume computations of the aggregation intensity which were from the experimental data of [111].

The model can be summarized as follows:

1. Mechanical activation of platelets is triggered by high scalar shear stress or wall shear stress releasing ADP
2. Platelets aggregate at the wall in places where the wall shear stress is low enough
3. Chemical activation is triggered when sufficient ADP is produced (C_{ADP}^{thr}) due to mechanical platelet activation
4. Thrombus growth starts when the threshold value of aggregation ε_t is reached at a wall cell. Growth in volume is permitted
5. The growing thrombus impacts the flow through the Brinkman term

Parameter	Value
α_ϵ	$3.7 \times 10^{-11} \text{ cm}^3 \text{ s}^{-1}$
$\tau_{low,wall}$	$0.05 \text{ N}\cdot\text{m}^{-1}$
$\tau_{high,wall}$	$0.2 \text{ N}\cdot\text{m}^{-1}$
$\tau_{breakdown,wall}$	$0.8 \text{ N}\cdot\text{m}^{-1}$
$\tau_{low,thrombus}$	$0.1 \text{ N}\cdot\text{m}^{-1}$
$\tau_{high,thrombus}$	$0.3 \text{ N}\cdot\text{m}^{-1}$
$\tau_{breakdown,thrombus}$	$0.9 \text{ N}\cdot\text{m}^{-1}$
B	2000 s^{-1}
ϵ_t	$5 \times 10^{18} \text{ m}^{-3}$
D	$5 \times 10^{-4} \text{ m}$
k	$9.5 \times 10^{-10} \text{ m}^2$

Table 4.2 Parameters use to calculate thrombus deposition and growth, all of the parameters are taken from [112].

4.2.3 Code verification

Chemical activation due to ADP

A batch reactor simulation was performed to verify this implementation. Following [112], the parameters involved in A_C were set to $t_{ADP} = 1 \text{ s}$ and $C_{ADP}^{thr} = 2 \mu\text{M}$. In this configuration, the species concentration is homogeneous in space. Thus, the transport equations can be simplified into a system of ordinary differential equations in time

$$\frac{\partial C_i}{\partial t} = R_i. \quad (4.13)$$

Eq. 4.13 was solved using a 4th order Runge–Kutta method using the initial conditions shown in Table 4.3.

Species	Initial condition
C_{AP}	$2.5 \times 10^{13} \text{ PLT m}^{-3}$
C_{NP}	$4.75 \times 10^{14} \text{ PLT m}^{-3}$
C_{ADP}	$2.0 \mu\text{M}$

Table 4.3 Initial conditions of platelets and ADP used to solve Eq. 4.13 considering only platelet chemical activation. PLT m^{-3} stand for platelet count per unit of volume. Initially $C_{ADP} = C_{ADP}^{thr}$

Figure 4.1 shows the evolution in time of species concentration. It can be observed that at, $t = 1$ s, platelets are fully activated following the characteristic activation time.

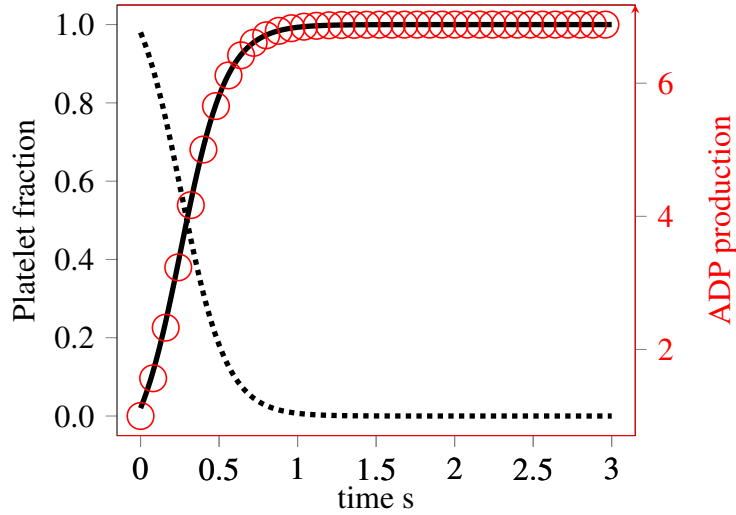


Fig. 4.1 Batch test case verification of chemical activation of platelets by ADP. Time evolution of activated platelets fraction $\frac{C_{AP}}{C_{NP}+C_{AP}}$ (—), non activated platelets fraction $\frac{C_{NP}}{C_{AP}+C_{NP}}$ (.....) and normalized ADP $\frac{C_{ADP}}{C_{ADP}^{thr}}$ (○) (right y axis)

4.2.4 Verification: Backward facing Step Application

The benchmark presented by Taylor et al. [111] was used to verify the implementation of the model for thrombus growth in YALES2BIO. Fig 4.2 shows the computational domain of the BFS benchmark; this case was already used in Chapter 2. The Reynolds number of this configuration is $Re = 430$ based on the inlet channel height, the kinematic viscosity $\nu = 3.5 \times 10^{-6} \text{ m}^2\text{s}^{-1}$, the density $\rho = 1060 \text{ kg m}^{-3}$ and the upstream bulk velocity $u_x = 0.229 \text{ m}\cdot\text{s}^{-1}$. The mesh contains 268162 triangular elements with a maximum spatial resolution of $\Delta x_{ax} = 0.1 \text{ mm}$ and a refinement zone at the mixing layer after the step of $\Delta x_{min} = 0.025 \text{ mm}$. The initial and inlet conditions for platelets and ADP are identified. Their values are shown in Table 4.3. Background platelet activation of 5 % was set, to match [112].

Fig 4.3 shows the scalar field of τ . Note that the locations of low scalar shear stress are susceptible to thrombus deposition and growth. It can also be observed that high activation of platelets due to high scalar shear stress is observed near the edge of the step.

Species	Concentrations
C_{AP}	$2.5 \times 10^{13} \text{ PLT m}^{-3}$
C_{NP}	$4.75 \times 10^{14} \text{ PLT m}^{-3}$
C_{ADP}	$0 \mu\text{M}$

Table 4.4 Inlet and initial conditions of platelets and ADP used in the BFS benchmark.

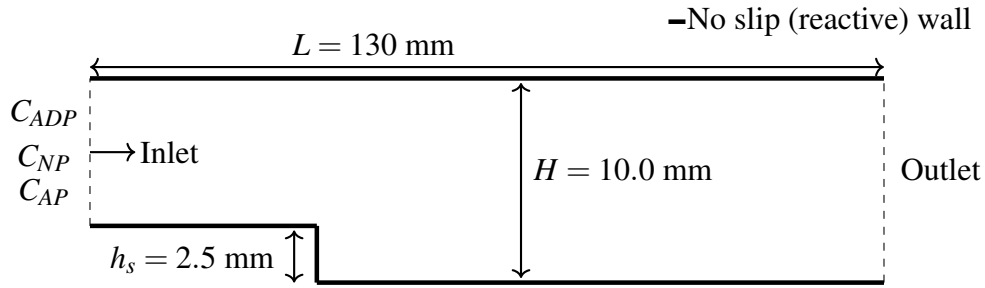
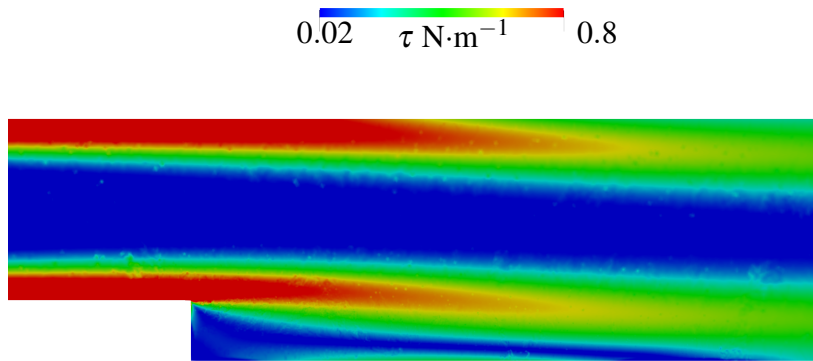


Fig. 4.2 Backward facing step computational domain based on [111]

Fig. 4.3 Field of scalar stress, activation taking place at zones of high τ .

Thrombus growth in time is shown in Fig. 4.5. A white contour using ε_t shows the thrombus progress. A reduction in velocity is observed inside the thrombus.

In Fig. 4.5, thrombus length T_L and height T_H at the step wall are used to compare the experimental results [111] and the original model [112] with the current numerical results. The implemented model captures the general trend of thrombus growth. The small deviations to the original model of Taylor et al. may be due to different numerical schemes or to the different topology of the meshes used in the simulations (structured versus unstructured).

Note however that a second thrombus is formed at the reattachment length in areas in which the wall shear stress is lower than τ_{low} . Figure 4.6 shows the formation of the second clot. This thrombus is not formed in the experimental configuration of Taylor et al. [111].

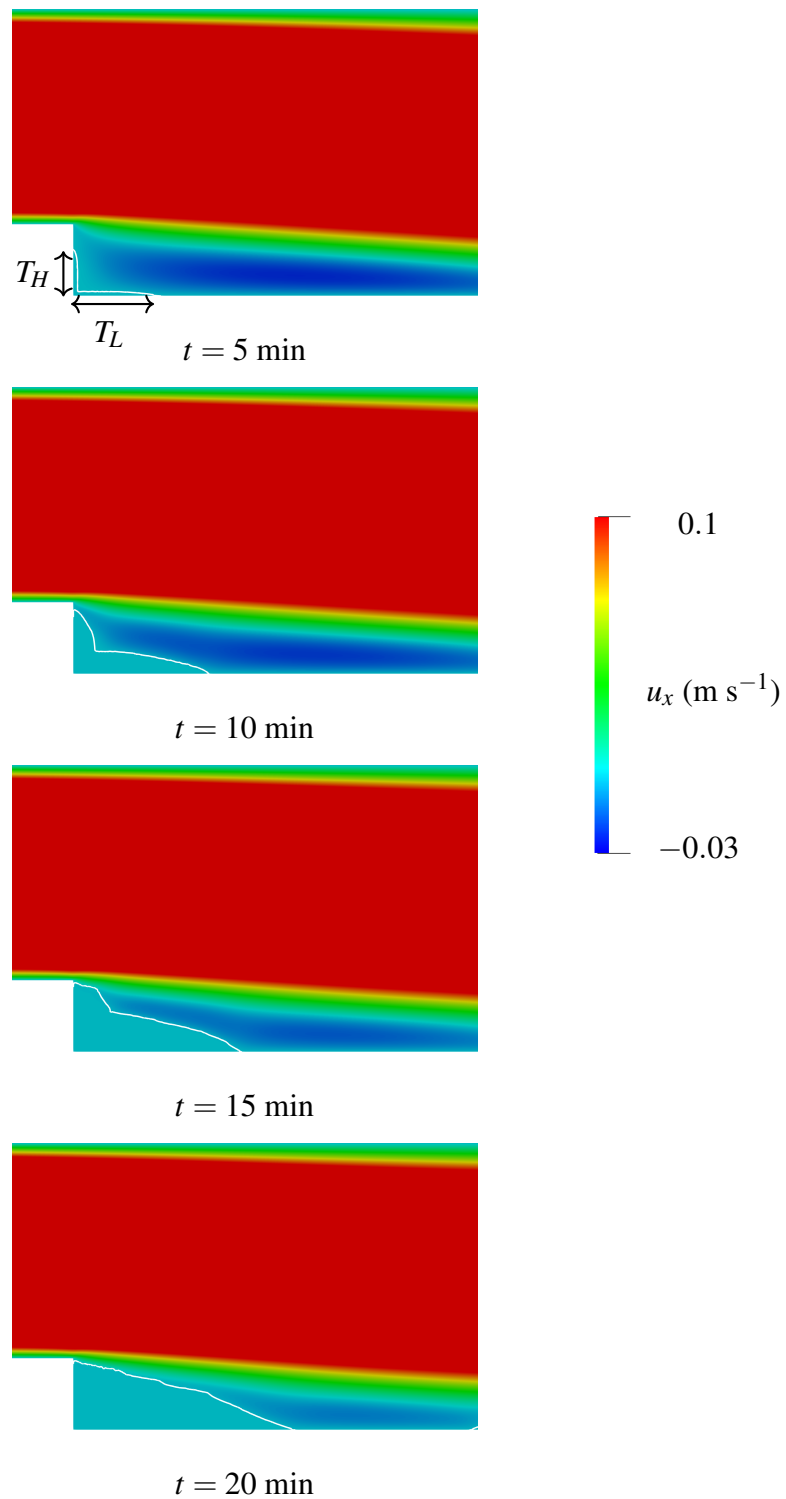


Fig. 4.4 Velocity field in x direction with white contour of ε_t showing the thrombus. The general agreement is fair.

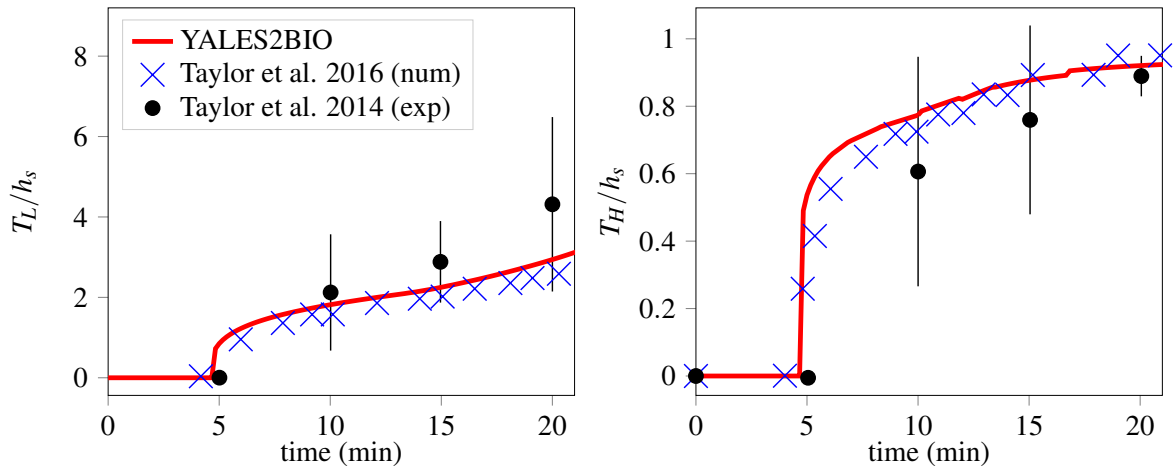


Fig. 4.5 The numerical results from the current implementation of the model from [112] compared against numerical and experimental results

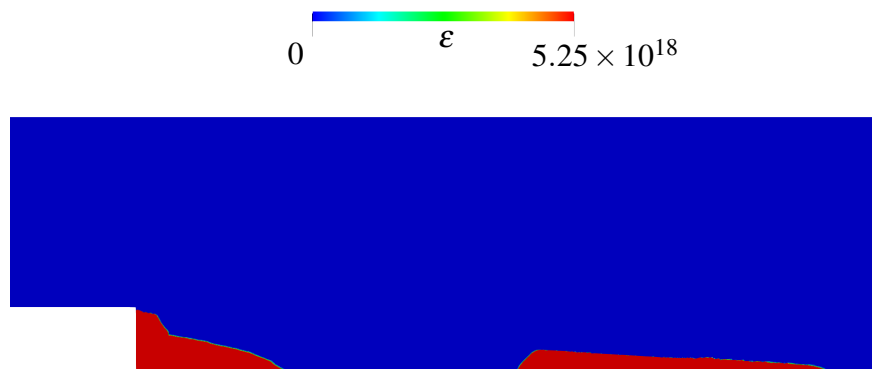


Fig. 4.6 Platelet aggregation scalar field ϵ , a second thrombus formed at the reattachment point, this effect is not observed in the experimental configuration of [111].

The second thrombus is also observed in the numerical results of [112], although not discussed. One of the possible causes of this effect is that the pulsatile nature of the pump which can induce low-level flow rate perturbations are not accounted in the model of Taylor et al. and a constant velocity inlet is applied. Zmijanovic et al. [131] showed that including inlet perturbations may help to solve a similar type of issue and improve the robustness of the simulations. A simulation including arbitrary inlet perturbations of the

form $u = 0.229(1.0 + \sum_{i=1}^3 A_i \sin(2\pi f_i t))$ was performed. The perturbations amplitudes and frequencies used on the simulations are displayed on Table 4.5.

i	f	A
1	5	0.05
2	0.5	0.01
3	2.3	0.025

Table 4.5 Perturbations frequencies and amplitudes used at the velocity inlet boundary condition. These values were arbitrary chosen.

Figure 4.7 shows the results of the original implemented model of Taylor and the inlet-perturbed case at $t = 340$ s. When inlet perturbations are included, it can be observed that the second thrombus is not formed, even if the amplitude of the perturbations are a few percents only. It is also observed that the size of the main thrombus at the corner is reduced or slow down.

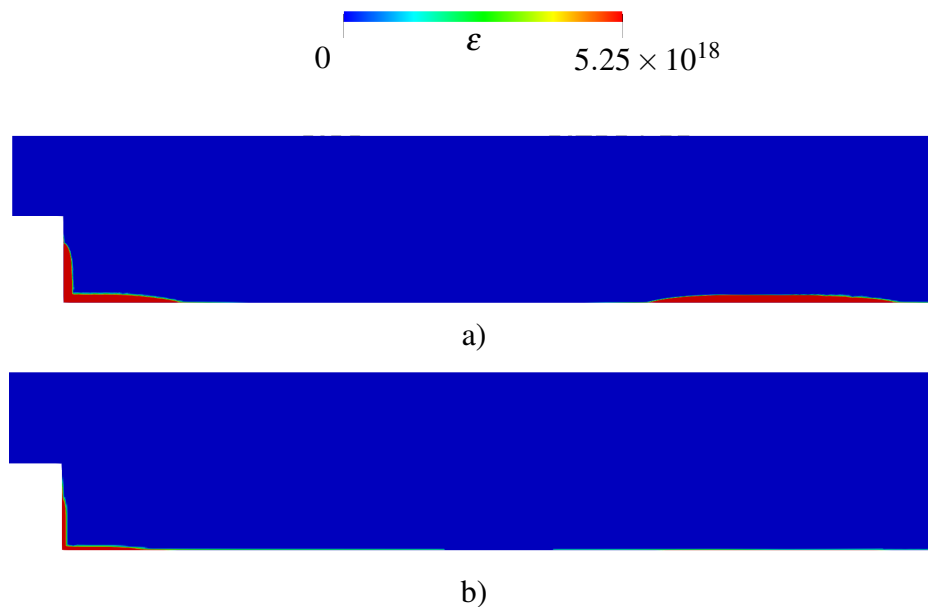


Fig. 4.7 Platelet aggregation intensity at $t = 340$ s, a) case with inlet perturbations b) constant velocity inlet.

4.3 Including the coagulation cascade

Method description

It is well known that a powerful activator of platelets is thrombin [44]. The activation model proposed by [107] considers platelet activation by thrombin. In the model of Soares and colleagues, thrombin is released by platelets activation being the only source of thrombin. The same form of Eq. 4.2 is proposed for thrombin activation considering a concentration threshold of $C_{II_a}^{thr} = 0.833$ nM and a characteristic time of $t_{II_a} = 1.0$ s as in [120]. Data is thus available about the activation of platelets by thrombin. Nevertheless, the coagulation cascade, which is one of the main sources of thrombin, has not been considered in these models dedicated to medical-devices.

The main challenge to directly include the coagulation cascade in complex flow configurations is the large number of species used in reference models [18, 100, 77]. Considering a large number of species is computationally prohibitive when analyzing thrombus formation due to the long characteristic time of thrombus formation $t \sim 30$ min as explained in [15, 87]. In this context reduced models are particularly interesting since they allow to capture the basic dynamics of thrombus formation with a significant reduction in the species transported.

In the current work, the reduced model of Chapter 3 is one-way coupled with the platelet-based thrombus growth proposed in [112]. Tab 4.6 lists the reactions of the reduced kinetic scheme. Reaction 1* is applied as reactive boundary condition following [77], in this approach the reaction source term of 1* is equal to the diffusive flux normal to the wall, as detailed in Chapter 2.

#	Reaction	K_m M	k_{cat} s ⁻¹	First order k s ⁻¹
1*	$XII \rightarrow XII_a$			$k_1 = 6.4 \times 10^{-3} ms^{-1}$
2	$XII_a + II \rightarrow II_a + XII_a$	$K_{m2} = 8.95 \times 10^{-9}$	$k_{cat2} = 8.21$	
3	$II_a + V \rightarrow II_a + V_a$	$K_{m3} = 2.0 \times 10^{-9}$	$k_{cat3} = 3.5 \times 10^3$	
4	$V_a + II \rightarrow V_a + II_a$	$K_{m4} = 8.25 \times 10^{-7}$	$k_{cat4} = 4.98$	
5	$II_a + ATIII \rightarrow II_a = ATIII$			$k_5 = 7.79 \times 10^{-3}$

Table 4.6 Reduced kinetic model for the coagulation cascade showed in Fig. 3.4. Reaction 1* is a first order surface reaction, reactions 2, 3 and 4 follow Michaelis–Menten kinetics, finally, reaction 5 is first order

Simulation including coagulation

A simulation including thrombin production due to the coagulation cascade in the BFS benchmark is performed. The inlet and the initial conditions of species are shown in Table 4.7.

Species	Condition
C_{XII}	9.36×10^{-11} M
C_{II}	9.33×10^{-5} M
C_V	6.2×10^{-9} M
C_{ATIII}	1.665×10^{-6} M
C_{AP}	2.5×10^{13} PLT m^{-3}
C_{NP}	4.75×10^{14} PLT m^{-3}
C_{ADP}	0 M

Table 4.7 Initial and inlet concentrations used in BFS benchmark simulation including thrombin formation due to coagulation. The values are taken from the reduced kinetic model developed in Chapter 3.

Figure 4.8 shows the thrombus height and length advancement in time. They both show a good agreement with both experimental [111] and numerical results [112].

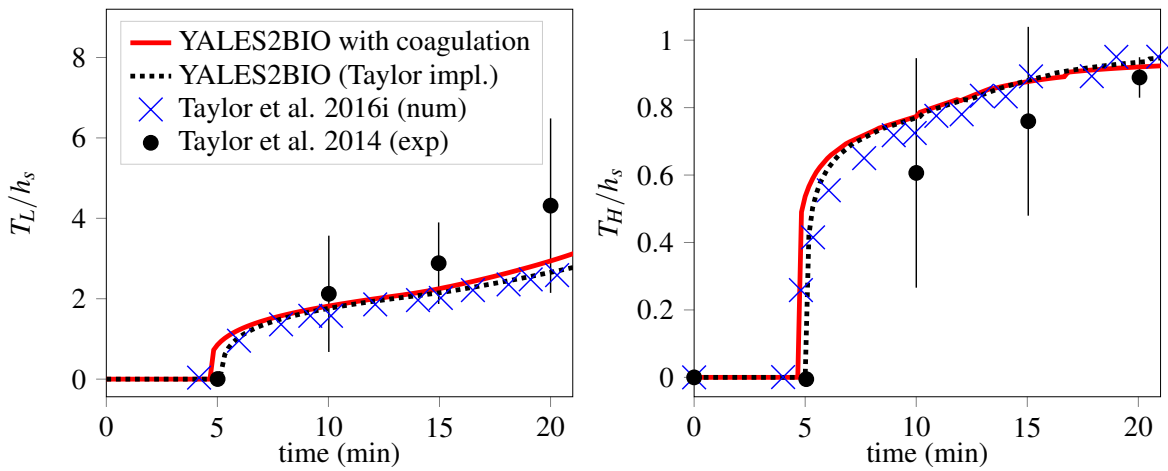


Fig. 4.8 Numerical results with coagulation, platelet-based model [112] and experimental results from [111]

4.4 Discussion

The platelet-based model for thrombus growth of Taylor et al. [111] was implemented in an in-house CFD solver YALES2BIO. Thrombin effect on platelet activation and thrombus growth was studied by coupling a reduced order model of the coagulation cascade initiated by contact activation with the thrombus growth model. The results aligned well with experimental and previous numerical data from [111, 112]. One of the model limitations is the empirical parameters derived specifically for the BFS benchmark. Thus, when a different configuration or wall material are studied, parameters such as τ_{low} , τ_{high} , or the volumetric growth rate α_e must be adapted. Compared to mechanical activation, thrombin driven activation was higher than mechanical activation. The thrombin threshold for thrombus activation was obtained at about 50 seconds, as showed in Fig. 4.9.

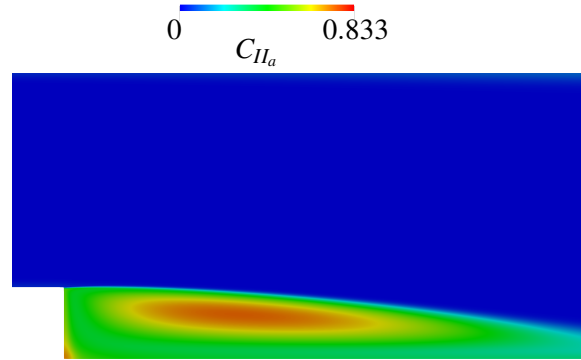


Fig. 4.9 Thrombin field at $t = 50$ s, the thrombin activation threshold $C_{II_a}^{thr} = 0.833$ nM is reached in the step lower corner and inside the recirculation region

Following the thrombin characteristic activation time $t_{II_a} \sim 1$ s and irreversible activation of platelets is shortly obtained after 51 s. This state of activation reaches all the recirculating region at about 1 min as observed in Fig. 4.10. In the same figure, the thrombin field is displayed at 1 min. It can be observed that activation of platelets propagates downstream along the lower wall following thrombin.

Eq. 4.10 showed that aggregation intensity depends on the squared of activated platelets. In the results of [112], final platelet activation levels were of about 8%. Due to this reason thrombus growth is highly dependent on background levels of platelet activation, arbitrary fixed at 5%. When coagulation is added, the totality of non-activated platelet become activated in the recirculating zone. Furthermore, this activation takes place very early in the simulation (at about 1 min). This decreases the influence of background activation of platelets

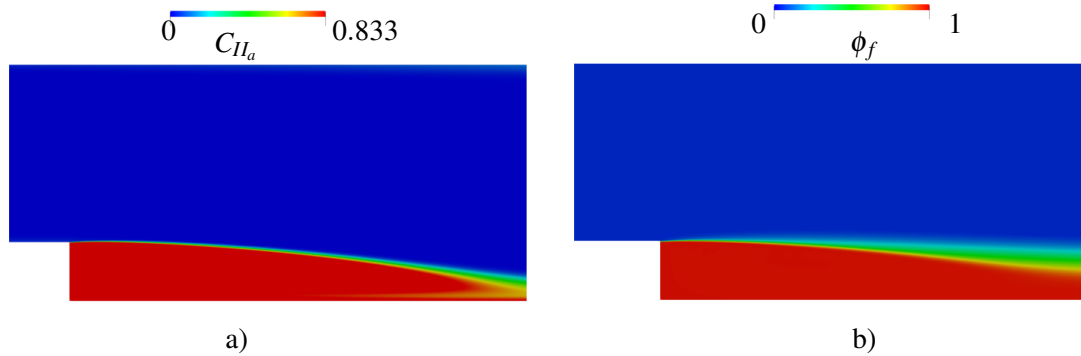


Fig. 4.10 a) Thrombin concentration (nM) at 60 s b) Activated platelet fraction ϕ_f at 60 s.

in the evolution of thrombin in time. A background activation of 7.5 % was tested without a significant difference on thrombus growth dynamics. Since platelet activation is higher than the original model of Taylor, the threshold value ε_t must be calibrated for the new levels of platelets aggregation. In the current case $\varepsilon_t = 2.0 \times 10^{21}$ was used. This value can be adapted since the aggregation intensity threshold is only a quantitative metric to capture thrombus growth and has no physical basis. Table 4.8 shows the values of background platelet activation used in 3 different simulations performed by Taylor et al. [112] and two simulations including platelet activation by thrombin with two values of background platelet activation.

Case	Background platelet activation (PLT m^{-3})
YALES2BIO Coagulation 1	2.5×10^{13}
YALES2BIO Coagulation 2	7.5×10^{13}
Taylor et al. [112] 1	1.5×10^{13}
Taylor et al. [112] 2	2.5×10^{13}
Taylor et al. [112] 3	3.7×10^{13}

Table 4.8 Background activation of platelets used in YALES2BIO simulations including platelet activation by thrombin and three cases computed by Taylor et al. [112].

Figure 4.11 shows that the results obtained in the model considering the coagulation cascade is robust when background platelet activation is varied. This is not the case for the original model of [112].

In conclusion, a possible explanation to the second thrombus formation at the reattachment point are the pulsatile perturbations present in the experimental set-up. When

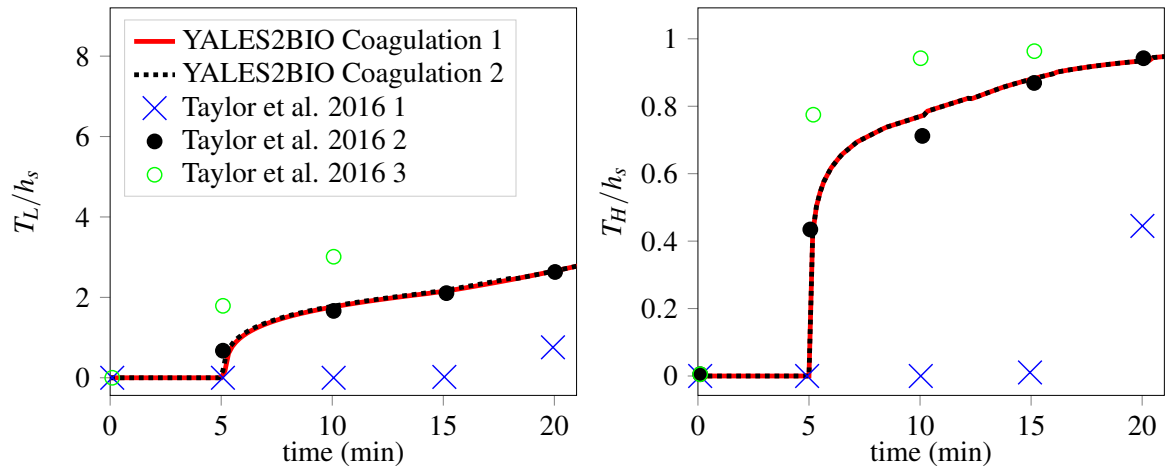


Fig. 4.11 Background activation dependency on platelet for the values of background platelet activation from Table 4.8.

considering inlet perturbations in the numerical simulations the second thrombus is not formed. The platelet-based model enriched with coagulation reactions may help to improve the robustness of the model proposed by Taylor et al. [112]. In addition, platelet activation by thrombin provides an additional triggering mechanism of thrombus formation in situations where mechanical activation of platelets is low.

Chapter 5

Conclusions and Perspectives

In this chapter the main results of the current work are summarized. Also perspectives in thrombosis related to blood-coated medical devices are discussed.

5.1 Main results

Chapter 2 In this chapter a numerical framework for proper initiation of the coagulation reactions was developed. A reactive boundary condition derived from a mass balance at the device wall was obtained considering the contact activation system. The model was applied to a BFS configuration using the kinetic model of Chatterjee et al. [30]. The novel reactive boundary condition for contact activation of factor *XII* was applied over all the BFS wall. A steady state solution was obtained and thrombin was formed in the same region where thrombus formed experimentally. The flow thus naturally selects the region whose coagulation takes place, even if the contact activation is triggered everywhere.

Chapter 3 The sensitivity of kinetic parameters in the model of Chatterjee et al. [30] was studied using the global screening technique of Morris [82]. The six most sensitive parameters to relevant quantities of interest were identified. The results were confirmed with a remarkable precision using a Stroud quadrature and calculating the Sobol indices. A reduced kinetic scheme for thrombin formation triggered by the contact activation system is proposed. The reactions that appear in the reduced model are mainly derived from the sensitive analysis. Bayes statistical framework is used to find the optimal parameters that include kinetic rates and species initial concentrations. When initial prothrombin concentration is varied, the reduced order model shows fair predictive capabilities for a fixed set of optimal parameters.

Chapter 4 The model of Taylor et al. [112] for thrombus growth based on platelet activity was implemented in YALES2BIO. The model was applied to the BFS benchmark already used in Chapter 2. Thrombus length and height advancement are correctly captured by the implemented model. However, a second thrombus is observed at the reattachment point, which is not present in the in-vitro experimental configuration. Low-level velocity perturbations at the inlet boundary suppressed the growth of the thrombus at the reattachment point. Finally the platelet-based model was one-way coupled with the reduced kinetic model of Chapter 3 considering chemical activation of platelets due to thrombin. The strong platelet activation due to thrombin eliminates the results sensitivity to background activation of platelets from the original model of Taylor.

This thesis contributes to the efforts of thrombus modeling in medical devices towards the long term objective of device optimization and intervention planning. To this end, robust models, sophisticated enough and computationally affordable are needed. A numerical framework addressing these challenges is introduced in this work.

5.2 Perspectives

Surface impact on factor *XII* activation

In the parametric study of the activation rate of factor *XII* performed in Chapter 2 a small impact on thrombin production was observed. This contrast to the model of Guo et al. [50] in which the surface properties impacted the thrombin production by modifying the auto-activation rate of factor *XII* along with reciprocal activation and auto-hydrolysis reaction rates. The reciprocal activation and auto-hydrolysis rates were not modified in our parametric study. Therefore, investigating this effect and adding other elements such as finite binding sites for factor *XII* and other proteins like Fibrinogen on the device surface could help to develop a surface-specific kinetic model.

Role of phospholipids

Phospholipids are present in the membranes of activated platelets, providing a surface on which the Tenase and Prothrombinase complexes are assembled. The binding sites available for the complex limit the formation of thrombin; a detailed description of this process and its modeling can be found in the work of [70]. In our modified version of the platelet-based model of Taylor et al. [112] in Chapter 4 coagulation was included without accounting for this

effect. If phospholipids are considered they may limit the large concentration of thrombin and thus the activation of platelets. The role of phospholipids should be investigated to evaluate its impact on device-related thrombosis.

Chemical activation of platelets and deposition

In Chapter 4 chemical activation of platelets is modeled using the approach proposed by [109] which was developed almost two decades ago. This model was able to capture platelet deposition and activation in a collagen surface. However, this work should be revisited and extent to account for different levels of activation and deposition in other bio-material surfaces.

Role of turbulence in device-related thrombosis

Turbulence influence in thrombosis is not well understood. In particular, medical devices often induce non-physiological flow regimes that may promote turbulence such as mechanical hear valves [106]. This type of effects can be included in the model of Taylor and quantify, for example, the effects on platelet activation or enhance mixing in biochemical species.

Sensitivity analysis on reduced and detailed models

A sensitivity analysis can be performed to the reduced model to further reduce the complexity if needed or improve our understanding of the reactions taking place in the model.

Sensitivity analysis methods could be useful to identify situations in which the current biological descriptions do not explain experimental observations and thus the role of new pathways or biological events could be pointed out by performing sensitivity analysis on specific quantity of interest.

Model validation in different types of devices

The thrombus growth model based on platelet aggregation and coagulation reactions should be tested in other academic configurations [46, 120]. This would help to learn if the model parameters are robust in different flow regimes and understand the dynamics of thrombus formation in these configurations. Also, complicated device applications should be studied

using this model to identify limitations and improve the models.

References

- [1] Achille, P. D., Tellides, G., Figueroa, C. A., and Humphrey, J. D. (2014). A haemodynamic predictor of intraluminal thrombus formation in abdominal aortic aneurysms. *Proc. R. Soc. A*, 470(20140163).
- [2] Alderazi, Y. J., Shastri, D., Kass-Hout, T., Prestigiacomo, C. J., and Gandhi, C. D. (2014). Flow diverters for intracranial aneurysms. *Stroke Res. and Treat.*, 2014(415653):1–12.
- [3] Alemu, Y. and Bluestein, D. (2007). Flow-induced platelet activation and damage accumulation in a mechanical heart valve: Numerical studies. *Artif. Organs*, 31(9):677–688.
- [4] Alemu, Y., Girdhar, G., Xenos, M., Sheriff, J., Jesty, J., Einav, S., and Bluestein, D. (2010). Design optimization of a mechanical heart valve for reducing valve thrombogenicity - a case study with ats valve. *Am. Soc. Artif. Intern. Org.*, 56(5):389–396.
- [5] Anand, M. and Rajagopal, K. (2017). A short review of advances in the modelling of blood rheology and clot formation. *Fluids*, 2(3).
- [6] Anand, M., Rajagopal, K., and Rajagopal, K. R. (2003). A model incorporating some of the mechanical and biochemical factors underlying clot formation and dissolution in flowing blood. *J. Theor. Med.*, 5:183–218.
- [7] Anand, M., Rajagopal, K., and Rajagopal, K. R. (2006). A model for the formation and lysis of blood clots. *Pathophysiol. Haemost. Thromb.*, 34:109–120.
- [8] Anand, M., Rajagopal, K., and Rajagopal, K. R. (2008). A model for the formation, growth, and lysis of clots in quiescent plasma. a comparison between the effects of antithrombin iii deficiency and protein c deficiency. *J. Theor. Biol.*, 253:725–738.
- [9] Andrieu, C., De Freitas, N., Doucet, A., and Jordan, M. I. (2003). An introduction to mcmc for machine learning. *Mach. Learn.*, 50:5–43.
- [10] Antonini, G., Guiffant, G., Quemada, D., and Dosne, A. (1978). Estimation of platelet diffusivity in flowing blood. *Biorheo.*, 15:111–117.
- [11] Armaly, B. F., Durst, F., and Pereira, J. C. F. (1983). Experimental and theoretical investigation of backward-facing step flow. *J. Fluid Mech.*, 127:473–496.
- [12] Ashyraliyev, M., Fomekong-Nanfack, Y., Kaandorp, J. A., and Blom, J. G. (2009). Systems biology: parameter estimation for biochemical models. *FEBS J.*, 276(4):886–902.

- [13] Basmadjian, D. (1990). The effect of flow and mass transport in thrombogenesis. *Ann. of Biomed. Eng.*, 18:685–709.
- [14] Basmadjian, D., Sefton, M. V., and Baldwin, S. A. (1997). Coagulation on biomaterials in flowing blood: Some theoretical considerations. *Biomaterials*, 18:1511–1522.
- [15] Belyaev, A. V., Dunster, J., Gibbins, J., Panteleev, M., and Volpert, V. P. o. L. R. (2018). Modeling thrombosis in silico: Frontiers, challenges, unresolved problems and milestones. *Phys. Life Rev.*, in press.
- [16] Bhogal, P., Martinez Moreno, R., Ganslandt, O., Bätzner, H., Henkes, H., and Perez, M. A. (2017). Use of flow diverters in the treatment of unruptured saccular aneurysms of the anterior cerebral artery. *J. Neurointerv. Surg.*, 9(3):283–289.
- [17] Biasetti, J., Hussain, F., and Gasser, T. C. (2011). Blood flow and coherent vortices in the normal and aneurysmatic aortas: a fluid dynamical approach to intra-luminal thrombus formation. *J. R. Soc. Interf.*, 8:1449–1461.
- [18] Biasetti, J., Spazzini, P. G., Swedenborg, J., and Gasser, T. C. (2012). An integrated fluid-chemical model toward modeling the formation of intra-luminal thrombus in abdominal aortic aneurysms. *Front. Physiol.*, 3(266).
- [19] Birolleau, A., Poëtte, G., and Lucor, D. (2014). Adaptive bayesian inference for discontinuous inverse problems, application to hyperbolic conservation laws. *Commun. Comput. Phys.*, 16(1):1–34.
- [20] Bludszuweit (1995). Three-dimensional numerical prediction of stress loading of blood particles in a centrifugal pump. *Artif. Organs*, 19(7):590–596.
- [21] Bodnár, T. and Sequeira, A. (2008). Numerical simulation of the coagulation dynamics of blood. *Comput. Math. Meth. Med.*, 9:83–104.
- [22] Brummel-Ziedins, K. E., Orfeo, T., Callas, P. W., Gissel, M., Mann, K. G., and Bovill, E. G. (2012). The prothrombotic phenotypes in familial protein c deficiency are differentiated by computational modeling of thrombin generation. *PLoS One*, 7(9).
- [23] Brummel-Ziedins, K. E. and Wolberg, A. S. (2014). Global assays of hemostasis. , 21(5):395–403.
- [24] Cadroy, Y. and Hanson, S. R. (1990). Effects of red blood cell concentration on hemostasis and thrombus formation in a primate model. *Blood*, 75(11):2185–2193.
- [25] Campolongo, F., Cariboni, J., and Saltelli, A. (2007). An effective screening design for sensitivity analysis of large models. *Environ. Mod. Soft.*, 22(10):1509—1518.
- [26] Casa, L. D. C. and Ku, D. N. (2017). Thrombus formation at high shear rates. *Ann. Rev. Biomed. Eng.*, 19(1):415–433.
- [27] Celik, I. B., Ghia, U., Roache, P. J., Freitas, C. J., Coleman, H., and Raad, P. E. (2008). Procedure for estimation and reporting of uncertainty due to discretization in cfd applications. *J. Fluids Eng.*, 130. article id 078001.

- [28] Chan, M. Y., Weitz, J. I., Merhi, Y., Harrington, R. A., and Becker, R. C. (2009). Catheter thrombosis and percutaneous coronary intervention: fundamental perspectives on blood, artificial surfaces and antithrombotic drugs. *J. Thromb. Thrombol.*, 28:366–380.
- [29] Chatterjee, K., Thornton, J. L., Bauer, J. W., Vogler, E. A., and Siedlecki, C. A. (2009). Moderation of prekallikrein-factor xii interactions in surface activation of coagulation by protein-adsorption competition. *Biomaterials*, 30(28):4915–4920.
- [30] Chatterjee, M. S., Denney, W. S., Jing, H., and Diamond, S. L. (2010). Systems biology of coagulation initiation: Kinetics of thrombin generation in resting and activated human blood. *PLoS Comp. Biol.*, 6(9).
- [31] Chnafa, C., Mendez, S., Moreno, R., and Nicoud, F. (2014a). *The Cardio-Circulatory System : from Modeling to Clinical Applications*, chapter Using image-based CFD to investigate the intracardiac turbulence. Springer.
- [32] Chnafa, C., Mendez, S., and Nicoud, F. (2013). Multi-cycle large-eddy simulations of the flow in a left heart. In *8th Symposium on Turbulent and Shear Flow Phenomena, 28-30 August 2013, Poitiers, FRANCE*.
- [33] Chnafa, C., Mendez, S., and Nicoud, F. (2014b). Image-based large-eddy simulation in a realistic left heart. *Comput. Fluids*, 94:173–187.
- [34] Chnafa, C., Mendez, S., and Nicoud, F. (2016). Image-based simulations show important flow fluctuations in a normal left ventricle: What could be the implications? *Ann. of Biomed. Eng.*, 44(11):3346–3358.
- [35] Chorin, A. (1968). Numerical solution of the Navier–Stokes equations. *Math. Comp.*, 22:745–762.
- [36] Danforth, C. M., Orfeo, T., Mann, K. G., Brummel-Ziedins, K. E., and Everse, S. J. (2009). The impact of uncertainty in a blood coagulation model. *Math. Med. Biol.*, 26(4):323—336.
- [37] De Biasi, A. R., Manning, K. B., and Salemi, A. (2015). Science for surgeons: Understanding pump thrombogenesis in continuous-flow left ventricular assist devices. *J. Thorac. Cardiovasc. Surg.*, 149(3):667–673.
- [38] Diamond, S. L. (2016). Systems analysis of thrombus formation. *Circ. Res.*, 118(9):1348–1362.
- [39] Dumont, K., Vierendeels, J., Kaminsky, R., van Nooten, G., Verdonck, P., and Bluestein, D. d. (2007). Comparison of the hemodynamic and thrombogenic performance of two bileaflet mechanical heart valves using a cfd/fsi model. *J. Biomech. Eng.*, 129(4):558–565.
- [40] Fogelson, A. L. (1992). Continuum models of platelet aggregation: Formulation and mechanical properties. *SIAM J. Appl. Math.*, 52(4):1089–1110.
- [41] Fogelson, A. L. and Guy, R. D. (2004). Platelet-wall interactions in continuum models of platelet thrombosis: formulation and numerical solution. *Math. Med. Biol.*, 21:293–334.

- [42] Fogelson, A. L. and Guy, R. D. (2008). Immersed-boundary-type models of intravascular platelet aggregation. *Comput. Meth. Appl. Mech. Eng.*, 197:2087–2104.
- [43] Fogelson, A. L. and Neeves, K. B. (2015). Fluid mechanics of blood clot formation. *Ann. Rev. Fluid Mech.*, 47(1):377–403.
- [44] Furie, B. and Furie, B. C. (2008). Mechanisms of thrombus formation. *New Eng. J. Med.*, 359:938–949.
- [45] Galley, H. F. and Webster, N. R. (2004). Physiology of the endothelium. , 93(1):105–113.
- [46] Goodman, P. D., Barlow, E. T., Crapo, P. M., Mohammad, S. F., and Solen, K. A. (2005). Computational model of device-induced thrombosis and thromboembolism. *Ann. of Biomed. Eng.*, 33:780–797.
- [47] Gorbet, M. B. and Sefton, M. V. (2004). Biomaterial-associated thrombosis: roles of coagulation factors, complement, platelets and leukocytes. *Biomaterials*, 25:5681–5703.
- [48] Grabowski, E. F., Friedman, L. I., and Leonard, E. F. (1972). Effects of shear rate on the diffusion and adhesion of blood platelets to a foreign surface. *Ind. Eng. Chem. Fundam.*, 11:224–232.
- [49] Gregory, K. and Basmadjian, D. (1994). An analysis of the contact phase of blood coagulation: Effects of shear rate and surface are intertwined. *Ann. of Biomed. Eng.*, 22:184–193.
- [50] Guo, Z., Bussard, K. M., Chatterjee, K., Miller, R., Vogler, E. A., and Siedlecki, C. A. (2006). Mathematical modeling of material-induced blood plasma coagulation. *Biomed. Mater.*, 27(5):796–806.
- [51] Hansen, K. B., Arzani, A., and Shadden, S. C. (2015). Mechanical platelet activation potential in abdominal aortic aneurysms. *J. Biomech. Eng.*, 137:041005 –1–8.
- [52] Hansen, K. B. and Shadden, S. C. (2015). A reduced-dimensional model for near-wall transport in cardiovascular flows. *Biomech. Model. Mechanobiol.*
- [53] Hastings, S. M., Ku, D. N., Wagoner, S., Maher, O. K., and Deshpande, S. (2017). Sources of circuit thrombosis in pediatric extracorporeal membrane oxygenation. *Am. Soc. Artif. Intern. Org.* , 63(1):86–92.
- [54] Hellums, J. D. (1994). 1993 whitaker lecture: Biorheology in thrombosis research. *Ann. of Biomed. Eng.*, 22:445–455.
- [55] Hemker, H., Giesen, P., Al Dieri, R., Regnault, V., De Smedt, E., Wagenvoort, R., Lecompte, T., and Béguin, S. (2003). alibrated automated thrombin generation measurement in clotting plasma. *Pathophysiol. Haemost. Thromb.*, 33:4—15.
- [56] Hemker, H. C., Kerdelo, S., and Kremers, R. M. W. (2012). Is there value in kinetic modeling of thrombin generation? no (unless...). *J. Thromb. Haemost.*, 10:1470–1477.
- [57] Hockin, M. F., Jones, K. C., Everse, S. J., and Mann, K. G. (2002). A model for the stoichiometric regulation of blood coagulation. *J. Biol. Chem.*, 277(21):18322–18333.

- [58] Hoffbrand, A. V. and Moss, P. A. H. (2011). *Essential Haematology*, volume 1. Wiley-Blackwell, 6 edition.
- [59] Iooss, B. and Lemaître, P. (2015). *Uncertainty Management in Simulation-Optimization of Complex Systems: Algorithms and Applications*, chapter A Review on Global Sensitivity Analysis Methods, pages 101–122. Springer US.
- [60] Jaffer, I. H., Fredenburgh, J. C., Hirsh, J., and Weitz, J. I. (2015). Medical device-induced thrombosis: what causes it and how can we prevent it? *J. Thromb. Haemost.*, 13(Suppl. 1):72–81.
- [61] Jetsy, J., Yin, W., Perrotta, P., and Bluestein, D. (2003). Platelet activation in a circulating flow loop: combined effects of shear stress and exposure time. *Platelets*, 14(3):143–149.
- [62] Jones, K. C. and Mann, K. G. (1994). A model for the tissue factor pathway to thrombin. ii. a mathematical simulation. *J. Biol. Chem.*, 269:23367–23373.
- [63] Kim, J. and Moin, P. (1985). Application of a fractional-step method to incompressible Navier-Stokes equations. *J. Comput. Phys.*, 59:308–323.
- [64] Kirklin, J. K., Pagani, F. D., Kormos, R. L., Stevenson, L. W., Blume, E. D., Myers, S. L., Miller, M. A., Baldwin, J. T., Young, J. B., and Naftel, D. C. (2017). Eighth annual intermacs report: Special focus on framing the impact of adverse events. *J. Heart Long Transplant.*, 36(10):1080–1086.
- [65] Kroll, M. H., Hellums, J. D., McIntire, L. V., Schafer, A. I., and Moake, J. L. (1996). Platelets and shear stress. *Blood*, 88(5):1525–1541.
- [66] Krüger, T. (2016). Effect of tube diameter and capillary number on platelet margination and near-wall dynamics. *Rheol. Acta*, 55(6):511–526.
- [67] Kuharsky, A. L. and Fogelson, A. L. (2001). Surface-mediated control of blood coagulation: the role of binding site densities and platelet deposition. *Biophys. J.*, 80:1050–1074.
- [68] Lanotte, L., Mauer, J., Mendez, S., Fedosov, D. A., Fromental, J.-M., Clavería, V., Nicoud, F., Gompper, G., and Abkarian, M. (2016). Red cells’ dynamic morphologies govern blood shear thinning under microcirculatory flow conditions. *Proc. Natl Acad. Sc. USA*, 113(47):13289–13294.
- [69] Larsson, M., Rayzman, V., Nolte, M. W., Nickel, K. F., Björkqvist, J., Jämsä, A., Hardy, M. P., Fries, M., Schmidbauer, S., Hedenqvist, P., Broomé, M., Pragst, I., Dickneite, G., Wilson, M. J., Nash, A. D., Panousis, C., and Renné, T. (2014). A factor xiiia inhibitory antibody provides thromboprotection in extracorporeal circulation without increasing bleeding risk. *Sci. Transl. Med.*, 6(222).
- [70] Leiderman, K. and Fogelson, A. L. (2011). Grow with the flow: A spatial-temporal model of platelet deposition and blood coagulation under flow. *Math. Med. Biol.*, 28:47–84.

- [71] Litvinov, R. I. and Weisel, J. W. (2017). Role of red blood cells in haemostasis and thrombosis. *ISBT Sci. Series*, 12(1):176–183.
- [72] Malandain, M., Maheu, N., and Moureau, V. (2013). Optimization of the deflated conjugate gradient algorithm for the solving of elliptic equations on massively parallel machines. *J. Comput. Phys.*, 238:32–47.
- [73] Mann, K. G. (2012). Is there value in kinetic modeling of thrombin generation? yes. *J. Thromb. Haemost.*, 10:1463–1469.
- [74] Martins Afonso, M., Mendez, S., and Nicoud, F. (2014). On the damped oscillations of an elastic quasi-circular membrane in a two-dimensional incompressible fluid. *J. Fluid Mech.*, 746:300–331.
- [75] Mehra, M. R., Stewart, G. C., and Uber, P. A. (2014). The vexing problem of thrombosis in long-term mechanical circulatory support. *J. Heart Long Transplant.*, 33:1–11.
- [76] Mendez, S., Gibaud, E., and Nicoud, F. (2014). An unstructured solver for simulations of deformable particles in flows at arbitrary Reynolds numbers. *J. Comput. Phys.*, 256(1):465–483.
- [77] Méndez Rojano, R., Mendez, S., and Nicoud, F. (2018). Introducing the pro-coagulant contact system in the numerical assessment of device-related thrombosis. *Biomech. Model. Mechanobiol.*, 17(3):815–826.
- [78] Menichini, C., Cheng, Z., Gibbs, R. G. J., and Xu, X. Y. (2016). Predicting false lumen thrombosis in patient-specific models of aortic dissection. *J. R. Soc. Interf.*, 13(124).
- [79] Menichini, C., Cheng, Z., Gibbs, R. G. J., and Xu, X. Y. (2018). A computational model for false lumen thrombosis in type b aortic dissection following thoracic endovascular repair. *J. Biomech.*, 66:36 – 43.
- [80] Menichini, C. and Xu, X. Y. (2016). Mathematical modeling of thrombus formation in idealized models of aortic dissection: initial findings and potential applications. *J. Math. Biol.*, 73(5):1205–1226.
- [81] Michaelis, L., Menten, M., Johson, K., and Goodoy, R. (2011). The original michaelis constant: translation of the 1913 michaelis-menten paper. *Biochemistry-US*, 50(39):8264–8269.
- [82] Morris, M. (1991). Factorial sampling plans for preliminary computational experiments. *Technometrics*, 33:161–174.
- [83] Moureau, V. and Desjardins, O. (2008). A second-order ghost-fluid method for the primary atomization of liquid fuel in air-blast type injectors. In *Center for Turbulence Research. Proceedings of the Summer Program 2008*.
- [84] Moureau, V., Domingo, P., and Vervisch, L. (2011). Design of a massively parallel CFD code for complex geometries. *Comp. Rend. Méc.*, 339(2-3):141–148.
- [85] Naudin, C., Burillo, E., Blankenberg, S., Butler, L., and Renné, T. (2017). *Factor XII Contact Activation*. Thieme Medical Publishers, Inc.

- [86] Neeves, K. B., Illing, D. A. R., and Diamond, S. L. (2010). Thrombin flux and wall shear rate regulate fibrin fiber deposition state during polymerization under flow. *Biophys. J.*, 98:1344–1352.
- [87] Ngoepe, M. N., Frangi, A. F., Byrne, J. V., and Ventikos, Y. (2018). Thrombosis in cerebral aneurysms and the computational modeling thereof: A review. *Front. Physiol.*, 9:306.
- [88] Ngoepe, M. N. and Ventikos, Y. (2016). Computational modelling of clot development in patient-specific cerebral aneurysm cases. *J. Thromb. Haemost.*, 14(2):262–272.
- [89] Nobili, M., Sheriff, J., Morbiducci, U., Redaelli, A., and Bluestein, D. (2008). Platelet activation due to hemodynamic shear stresses: Damage accumulation model and comparison to in vitro measurement. *Am. Soc. Artif. Intern. Org.*, 54(1):64–72.
- [90] Panteleev, M. A., Balandina, A. N., Lipets, E. N., Ovanesov, M. V., and Ataulkhanov, F. I. (2010). Task-oriented modular decomposition of biological networks: Trigger mechanism in blood coagulation. *Biophys. J.*, 98(9):1751–1761.
- [91] Papadopoulos, K. P., Gavaises, M., and Atkin, C. (2014). A simplified mathematical model for thrombin generation. *Med. Eng. Phys.*, 36(2):196–204.
- [92] Piatti, F., Sturla, F., Marom, G., Sheriff, J., Claiborne, T. E., Slepian, M. J., Redaelli, A., and Bluestein, D. (2015). Hemodynamic and thrombogenic analysis of a trileaflet polymeric valve using a fluid-structure interaction approach. *J. Biomech.*, 48(13):3650–3658.
- [93] Pivkin, I. V., Richardson, P. D., and Karniadakis, G. (2006). Blood flow velocity effects and role of activation delay time on growth and form of platelet thrombi. *Proc. Natl Acad. Sc. USA*, 103:17164–17169.
- [94] Rana, K. and Neeves, K. B. (2016). Blood flow and mass transfer regulation of coagulation. *Bl. Rev.*, 0(0).
- [95] Renné, T., Pozgajová, M., Grüner, S., Schuh, K., Pauer, H.-U., Burfeind, P., Gailani, D., and Nieswandt, B. (2005). Defective thrombus formation in mice lacking coagulation factor xii. *J. Emerg. Med.*, 202(2).
- [96] Rice, N. T., Szlam, F., Varner, J. F., Bernstein, P. S., Szlam, A. D., and Tanaka, K. A. (2016). Differential contributions of intrinsic and extrinsic pathways to thrombin generation in adult, maternal and cord plasma samples. *PLoS One*, 11(5):e0154127.
- [97] Ruggeri, Z. M., Orje, J. N., Habermann, R., Federici, A. B., and Reininger, A. J. (2006). Activation-independent platelet adhesion and aggregation under elevated shear stress. *Blood*, 108((6)):1903–1910.
- [98] Saltelli, A., Ratto, M., Tarantola, S., and Campolongo, F. (2004). *Sensitivity analysis practice: A guide to scientific models*. Jhon Wiley & Sons, Ltd.
- [99] Schneider, S. W., Nuschele, S., Wixforth, A., Gorzelanny, C., Alexander-Katz, A., Netz, R. R., and Schneider, M. F. (2007). Shear-induced unfolding triggers adhesion of von willebrand factor fibers. *Proc. Natl Acad. Sc. USA*, 104((19)):7899–7903.

- [100] Seo, J. H., Abd, T., George, R. T., and Mittal, R. (2016). A coupled chemo-fluidic computational model for thrombogenesis in infarcted left ventricles. *Am. J. Phys.*, 310(11):H1567–H1582.
- [101] Seo, J.-H., Mittal, R., Abd, T., and George, R. (2015). Coupled chemo-fluidic computational modeling of thrombogenesis in infarcted hearts. In *4th International Conference on Computational and Mathematical Biomedical Engineering (CMBE2015), Paris, France, 29 June - 1 July 2015*.
- [102] Shadden, S. C. and Hendabadi, S. (2013). Potential fluid mechanic pathways of platelet activation. *Biomech. Model. Mechanobiol.*, 12:467–474.
- [103] Sigüenza, J. (2016). *Fluid-structure interaction problems involving deformable membranes: application to blood flows at macroscopic and microscopic scales*. PhD thesis, University of Montpellier.
- [104] Sigüenza, J., Mendez, S., Ambard, D., Dubois, F., Jourdan, F., Mozul, R., and Nicoud, F. (2016). Validation of an immersed thick boundary method for simulating fluid-structure interactions of deformable membranes. *J. Comput. Phys.*, 322:723–746.
- [105] Sigüenza, J., Mendez, S., and Nicoud, F. (2017). How should the optical tweezers experiment be used to characterize the red blood cell membrane mechanics? *Biomech. Model. Mechanobiol.*, 16:1645–1657.
- [106] Sigüenza, J., Pott, D., Mendez, S., Sonntag, S., Kaufmann, T. A. S., Steinseifer, U., and Nicoud, F. (2018). Fluid-structure interaction of a pulsatile flow with an aortic valve model: A combined experimental and numerical study. *Int. J. Numer. Meth. Biomed. Eng.*, 34(e2945):1–19.
- [107] Soares, J. S., Sheriff, J., and Bluestein, D. (2013). A novel mathematical model of activation and sensitization of platelets subjected to dynamic stress histories. *Biomech. Model. Mechanobiol.*, 12:1127–1141.
- [108] Sobol, I. M. (2001). Global sensitivity indices for rather complex mathematical models can be efficiently computed by monte carlo (or quasi-monte carlo) methods. these indices are used for estimating the influence of individual variables or groups of variables on the model output. */mcs*, 55:271–280.
- [109] Sorensen, E. N., Burgreen, G. W., Wagner, W. R., and Antaki, J. F. (1999). Computational simulation of platelet deposition and activation: I. model development and properties. *Ann. of Biomed. Eng.*, 27:436–448.
- [110] Sun, J. C. J., Davidson, M. J., Lamy, A., and Eikelboom, J. W. (2009). Antithrombotic management of patients with prosthetic heart valves: current evidence and future. *The Lancet*, 374(9689):565–576.
- [111] Taylor, J., Witmer, K., Neuberger, T., Craven, B., Meyer, R., Deutsch, S., and Manning, K. B. (2014). In vitro quantification of time dependant thrombus size using magnetic resonance image and computational simulations of thrombus surface shear stresses. *J. Biomech. Eng.*, 136(7).

- [112] Taylor, J. O., Meyer, R. S., Deutsch, S., and Manning, K. B. (2016). Development of a computational model for macroscopic predictions of device-induced thrombosis. *Biomech. Model. Mechanobiol.*, 15(6):1713–1731.
- [113] Thevenot, P., Hu, W., and Tang, L. (2008). Surface chemistry influences implant biocompatibility. *Current Topics Med. Chem.*, 8((4)):270–280.
- [114] Turitto, V. T. and Baumgartner, H. R. (1975). Platelet deposition on subendothelium exposed to flowing blood: mathematical analysis of physical parameters. *Am. Soc. Artif. Intern. Org.*, 21:593–601.
- [115] Vroman, L., Adams, A. L., Fischer, G. C., and Munoz, P. C. (1980). Interaction of high molecular weight kininogen, factor xii, and fibrinogen in plasma at interfaces. *Blood*, 55(1):156–159.
- [116] Wagenvoort, R., Hemker, P. W., and Hemker, H. C. (2006). The limits of simulation of the clotting system. *J. Thromb. Haemost.*, 4:1331–1338.
- [117] Wilhelm, C. R., Ristich, J., Kormos, R. L., and Wagner, W. R. (1998). Monocyte tissue factor expression and ongoing complement generation in ventricular assist device patients. *Ann. of Thora. Surg.*, 65(4):1071–1076.
- [118] Williamson, J. H. (1980). Low-storage Runge-Kutta schemes. *J. Comput. Phys.*, 35:48–56.
- [119] Wilson, W. M. and Cruden, N. L. (2013). Advances in coronary stent technology: current expectations and new developments. *Res. Rep. Clin. Cardio.*, 4:85–96.
- [120] Wu, W. T., Jamiolkowski, M. A., Wagner, W. R., Aubry, N., Massoudi, M., and Antaki, J. F. (2017). Multi-constituent simulation of thrombus deposition. *Sc. Rep.*, 7.
- [121] Wu, W. T., Yang, F., Wu, J., Aubry, N., Massoudi, M., and Antaki, J. F. (2016). High fidelity computational simulation of thrombus formation in thoratec heartmate ii continuous flow ventricular assist device. *Sc. Rep.*, 6:38025–1–11.
- [122] Xiu, D. (2010). *Numerical Methods for Stochastic Computations*. Princeton University Press.
- [123] Xu, Z., Chen, N., and Kamocka, M. M. Rosen, E. D. A. M. (2008). A multiscale model of thrombus development. *J. R. Soc. Interf.*, 5:705–722.
- [124] Yan, Y., Xu, L.-C., Vogler, E. A., and Siedlecki, C. A. (2018). *I - Contact activation by the intrinsic pathway of blood plasma coagulation*. Woodhead Publishing.
- [125] Yazdani, A., Li, H., Bersi, M. R., Di Achille, P., Insley, J., Humphrey, J. D., and Karniadakis, G. E. (2018). Data-driven modeling of hemodynamics and its role on thrombus size and shape in aortic dissections. *Sc. Rep.*, 8(1).
- [126] Yazdani, A., Li, H., Humphrey, J. D., and Karniadakis, G. E. (2017). A general shear-dependent model for thrombus formation. *PLoS Comp. Biol.*, 13(1):e1005291.
- [127] Yoganathan, A. P., He, Z., and Jones, S. C. (2004). Fluid mechanics of heart valves. *Ann. Rev. Biomed. Eng.*, 6:331–62.

-
- [128] Young, M. E., Carroad, P. A., and Bell, R. L. (1980). Estimation of diffusion coefficients of proteins. *Biotechnol. Bioeng.*, 22(5):947–955.
- [129] Zarnitsina, V. I., Pokhilko, A. V., and Ataulakhanov, F. I. (1996). A mathematical model for the spatio-temporal dynamics of intrinsic pathway of blood coagulation. i. the model description. *Thromb. Res.*, 84(4):225–236.
- [130] Zhu, D. (2007). Mathematical modeling of blood coagulation cascade: kinetics of intrinsic and extrinsic pathways in normal and deficient conditions. *Blood. Coagul. Fibrinolysis.*, 18:637–646.
- [131] Zmijanovic, V., Mendez, S., Moureau, V., and Nicoud, F. (2017). About the numerical robustness of biomedical benchmark cases: Interlaboratory FDA’s idealized medical device. *Int. J. Numer. Meth. Biomed. Eng.*, 33(1):e02789:1–17.

Modélisation de la thrombose dans des dispositifs biomédicaux

Résumé. La thrombose est la formation d'un caillot sanguin (thrombus) dans le système cardiovasculaire. Il s'agit d'un des principaux problèmes des dispositifs biomédicaux en contact avec du sang. Toutefois, les biomatériaux utilisés jusqu'à présent dans ces dispositifs déclenchent la coagulation à travers le système de contact. Ce système n'a pas été pris en compte dans les modèles de thrombose dédiés aux dispositifs, alors que son importance pour la thrombose a été récemment remarquée. L'objectif de cette thèse est d'introduire les réactions de coagulation initiées par le système de contact dans la modélisation de la thrombose liées aux dispositifs. Un nouveau modèle réduit pour la génération de thrombine est proposé en incluant l'activation par contact. Le modèle arrive à calculer la formation de thrombine dans du plasma physiologique et du plasma déficient en prothrombine. Une fois réalisée, l'approche réduite est incluse dans un modèle de croissance du thrombus basé sur l'activité des plaquettes. Cette nouvelle stratégie est utilisée pour calculer la formation du thrombus dans une configuration académique.

Mots clés : Thrombose, dispositifs biomédicaux, système de contact.

Thrombosis modeling in blood coated medical devices

Abstract. Thrombosis, which is the formation of a blood clot (thrombus) in the vascular system, is one of the major issues of blood-coated medical devices. To reduce thrombosis risk in this type of devices, computational fluid dynamics has been used. Up to date, bio-material surfaces used in blood coated devices initiate blood coagulation through the contact activation system. This system has not been considered in models dedicated to devices, even though its importance in thrombosis has been recently highlighted. The objective of this thesis is to introduce device-triggered coagulation reactions in the modeling of device-related thrombosis. A novel reduced kinetic model including the contact activation system is proposed. The model correctly captures thrombin formation in physiological and prothrombin deficient platelet-poor-plasma. The reduced set of reactions is then included in a platelet-based model for thrombus formation considering platelet activation by thrombin. This approach is used to study thrombus formation in an academic configuration.

Keywords: Thrombosis, medical devices, contact system.